NOVEL DIELECTRIC FILM PROCESSING AND CHARACTERIZATION

By

WEN-BEN LUO

A DISSERTATION PRESENTED TO THE GRADUATE SCHOOL
OF THE UNIVERSITY OF FLORIDA IN PARTIAL FULFILLMENT
OF THE REQUIREMENTS FOR THE DEGREE OF
DOCTOR OF PHILOSOPHY

UNIVERSITY OF FLORIDA

2003

ACKNOWLEDGMENTS

I would like to thank my advisor Dr. Fan Ren, for providing the framework for my dissertation; for his guidance on my research; and for introducing me to semiconductor device physics, device design, processing, and characterization. His patience and encouragement helped me through the lengthy process of obtaining my degree. I can not express my appreciation adequately to thank him for the time he spent discussing and editing my dissertation.

I also thank my other dissertation committee members, Dr. Tim Anderson, Dr. Oscar Crisalle and Dr. Stephen Pearton as well as group advisor, Dr. Cammy Abernathy, for their valuable comments and time; and for making the semiconductor group such a good work environment.

I would like to express my gratitude to my colleagues: Wayne Johnson, Brent Gila, Jeff LaRoche, Gerard Dang, Anping Chang, Kyu-pil Lee, Jihyun Kim, Rishabh Menandru, and Kwang Baik. Special thanks go to Wayne, Brent, and Jeff for tolerating my English and helping to improve it with all of the conversations we had and with many bright discussions.

I thank Haoyin for all her endless love, understanding and supports. I appreciate the friendship with my ex-roommate, Yu-Hsiu Liu, who always shows me his generous concern.

Finally, to my family, I thank them for their endless dedication to the family and their ceaseless love and support as I pursue my dream. I hope there is a way that I can express my deepest appreciation.

TABLE OF CONTENTS

page

ACKNOWLEDGMENTS ii

ABSTRACT vi

CHAPTER

1 INTRODUCTION 1

1.1 Motivation 1
1.2 Disseration Outline 3

2 BACKGROUND AND LITERATURE REVIEW 4

2.1 Hydrogen Effects 4
2.2 Irradiation Hardness on Compound Semicondcutor 6
2.3 Surface Stability of Nitride HEMT 10

3 III-V COMPOUND SEMICONDUCTOR DEVICES FABRICATION 31

3.1 p-Ohmic Contact Study for Intra-Cavity Contacts in AlGaAs/GaAs Vertical-Cavity Surface-Emitting Lasers 31
3.2 High Breakdown M-I-M Structures on Bulk AlN 41
3.3 HVPE-Grwon AlGaN/GaN HEMTs 47

4 PLASMA DAMAGE EFFECTS ON III-V COMPOUND SEMICONDUCTOR DEVICES 55

4.1 Comparison of the Effects of H_2 and D_2 Plasma Exposure on AlGaAs/GaAs HEMTs 55
4.2 Hydorgenation Effects on AlGaAs/GaAs Heterojunction Bipolar Transistors 73

5 IRRADIATION HARDNESS OF III-V COMPOUND SEMICONDUCTOR DEVICES 90

5.1 Radiation-Induced Damages in Standard MESFET 90
5.2 Proton and Gamma-Ray Irradiation Effects on InGaP/GaAs Heterojunction Bipolar Transistors 97
5.3 Proton-Irradiated on dc and rf Performance of AlGaN/GaN High Electron Mobility Transistors 107

6 PASSIVATION EFFECTS OF PECVD DIELECTRIC FILMS ON III-V COMPOUND SEMCONDUCTOR DEVICES 118

6.1 Effect of Plasma Enhanced Chemical Vapor Deposition of SiN_X on n-GaN Schottky Rectifiers 118
6.2 Influence of PECVD Deuterated SiN_X on GaAs MESFETs and GaAs/AlGaAs HBTs 131

7 PASSIVATION EFFECTS OF MBE-GROWTH OXIDES ON NITRIDE HEMT DEVICES 140

7.1 Gas Source Molecular Beam Epitaxy Grown Oxide 140
7.2 Essentials of Surface Cleaning before Oxide Growth 142
7.3 Comparison of Surface Passivation Films for Reduction of Current Collapse in AlGaN/GaN HEMTs 156
7.4 Role of Cleaning Conditions and Epitaxial Layer Structure on Reliability of Sc_2O_3 and MgO Passivation on AlGaN/GaN HEMTs 170
7.5 Shielding Effects of Dielectric Films on Radiated Nitride HEMTs 180

LIST OF REFERENCES 189

BIOGRAPHICAL SKETCH 209

Abstract of Dissertation Presented to the Graduate School
of the University of Florida in Partial Fulfillment of the
Requirements for the Degree of Doctor of Philosophy

NOVEL DIELECTRIC FILM PROCESSING AND CHARACTERIZATION

By

Wen-Ben Luo

May, 2003

Chair: Fan Ren
Department: Chemical Engineering

We studied passivation effects of various dielectric films for GaAs MESFETs, AlGaAs/GaAs pseudo-morphic HEMTs, AlGaN/GaN HEMTs and AlGaAs/GaAs HBTs in terms of dc current-voltage characteristics, small signal responses, pulse and power measurement.

To prolong device lifetimes, depositions of passivation films play an important role in stabilizing device performance under biasing conditions. We used a plasma enhanced chemical vapor deposition (PECVD) system to investigate plasma-induced damage effects and passivation effects with different discharges such as N_2, H_2 or D_2. Three damage mechanisms are found after plasma exposures; creation of deep traps, preferential loss of As from the surface and passivation of acceptors or donors.

Radiation hard investigations were conducted with exposure of Cobalt^{60} and gamma sources to a variety of compound semiconductors devices. The irradiation doses corresponding to 10-100 years in low earth orbit could cause 30-50 % degradation in device performance.

Hydrogen-free, MBE-grown oxides use to passivate surface traps and suppress the current collapse phenomena of AlGaN/GaN HEMTs. We examined three different passivation films (SiN_X, MgO and Sc_2O_3) for their effectiveness in mitigating surface-state-induced current collapse in AlGaN/GaN HEMTs. Conventional PECVD SiN_X could recover 70-80% current level. Both the Sc_2O_3 and MgO passivated device produced essentially complete recovery of the current in GaN-cap HEMT structures and ~80 to 90% recovery in AlGaN-cap structures. In addition, the Sc_2O_3 had superior long-term stability, with no change in HEMT behavior over 5 months of aging.

CHAPTER 1
INTRODUCTION

1.1 Motivation

SiO_2 is well known in varied applications such as passivation material or insulator in the interlevel between metal and semiconductor in the last decades(1-5). Recently evaporated SiO_2 coupled with TiO_2 has been used as reflective mirror in optoelectronic devices(6-8). With the help of SiO_2 as a passivation layer, device lifetime actually successfully extend compared to those without SiO_2 deposited(9-12). In addition, SiO_2 does improve device leakage current several order of magnitude as a result of increasing barrier height in metal-oxide-semiconductor devices. Although SiO_2 is the essential dielectric material in Si based devices, it is not widely used in III-V dielectric device fabrication due to the native oxide formed during deposition at the SiO_2/III-V material interface. The III-V semiconductor native oxides consist of gallium oxide and arsenic oxide and their sub-oxides and it is known as the GaAs/native oxides interface is prone to high non-radiative recombination rates. The formation of interface states may either provide device leakage passes and causes degradation in device performance eventually during operation or trap carrier due to the creation of dangling bonds at the surface. PECVD silicon nitride (SiN_x) is currently used in the fabrication of III-V semiconductor devices. The SiN_x films are typically deposited form silane (SiH_4) and ammonium (NH_3) or from SiH_4 + N_2(13, 14). For the plasma enhanced chemical vapor deposition(PECVD) system, NH_3 is often used as a nitrogen source, since the high bond energy of N_2 usually results in silicon-rich films.

Silicon nitride is commonly used in the microelectronics industry as a diffusion barrier, an interlevel dielectric, a storage material for memory devices, and as a gate dielectric in thin film transistors. This is because SiN_x gives better device performance than other dielectrics, such as silicon oxide and tantalum oxide(15, 16).

Ether silicon dioxide or silicon nitride can not avoid a vital degradation problem in reliability test causing by hydrogen effects, due to the hydrogen element in PECVD precursors. A hydrogen-free passivation film or insulator will be a promising alternative for compound semiconductor materials. In the past ten years, different techniques such as Gas Source Molecular Beam Epitaxy (GSMBE) or E-beam implemented Molecular Beam Epitaxy (MBE) were applied to grow gate oxide such as GGG, Sc_2O_3 or MgO for III-V compound materials. Recently with steadily increasing emphasis on high power output amplifier, wide-bandgap such as SiC or GaN Field Effect Transistors provide solutions for wireless telecommunication and power plant. The major obstacle of AlGaN/GaN High Electron Mobility Transistors applications is the instability of surface traps resulting in the formation of virtual gate between high electric field between gate and drain terminals. An effective passivation film which passivate dangling bond and provide low interface state density will be essential to the problem. In last five years, silicon nitride has been used widely to cure this current collapse problem but long term reliability issue as a result of hydrogen passivation effects still is a concern. To develop a solution for this power swing problem without a worry about the hydrogen passivation will be interesting topic in future.

Another important reason why device passivation is critical is related to irradiation hardness of semiconductor devices. Because compound semiconductor devices are mainly applied in wireless telecommunication business, a high resistance to irradiation property can lower down the failure number and the cost of maintenance. Since it has been known that irradiation hardness is directly related to bandgap energy of semiconductor, compared to silicon based devices, gallium arsenide, silicon carbide or gallium nitride based transistors are capable to operate at higher irradiation dosage. An understanding of transistor performance changes corresponding to the exposed doses is important for circuit designer. In addition, the protection effects of passivation layers on device performance are worthy to investigate.

1.2 Dissertation Outline

Chapter 2 reviews the hydrogen passivation effect and surface instability problem of Nitride materials. Chapter 3 presents device fabrication and characterization of contact study on VCSEL structure, the AlN Schottky rectifier and AlGaN/GaN HEMTs on sapphire by HVPE. Chapter 4 includes the hydrogen passivation effects on AlGaAs/GaAs HEMTs and HBTs. The dc current-voltage technique is widely used to identify plasma damage effects on device performance by inductively coupled plasma etcher in order to simplify the plasma chemical factor. Chapter 5 discusses the proton and cobalt^{60} irradiation hardness of different compound semiconductor devices on varied materials. Chapter 6 deals with the deposition of dielectric films, SiN_X and SiO_2, by PECVD. The passivation effects on current-voltage characteristics of MESFET, HBT and Schottky rectifiers are also included. Chapter 7 presents the growth of novel oxide by GSMBE and the passivation effect on GaN HEMTs. We showed short- and long-term reliability of oxide for nitride HEMTs were performed by bias stressing. In addition, the shielding effect of oxide for proton irradiation hardness is also concluded.

CHAPTER 2
BACKGROUND AND LITERATURE REVIEW

2.1 Hydrogen Effects

Due to the limited thermal stability of III-V based materials, the deposition temperature is kept ≤ 300 °C and the Si-H and N-H bonds from the precursors, SiH_4 and NH_3, respectively, can not be completely broken(17, 18). Therefore, typical PECVD SiN_x does not have a fixed stoichiometry but rather contains varying amount of Si, N and H. The SiN_x films deposited in system without a load-lock chamber often contain around 5% oxygen when low deposition temperature is used (< 250 °C). The hydrogen content can be as high as 39 % (atomic) and is strongly dependent on the deposition conditions. The ratio of Si-H to N-H also depends on the deposition conditions(19). The rearrangement of hydrogen bonds and the out-diffusion of free hydrogen in the film can create traps and cause instability in devices(20-23). Trap formation can occur at subsequent high temperature process steps or during device operation. Under high electric field conditions, hot electrons can inject into the dielectric film and will release bonded H therefore create electron traps.

Hydrogen is critical to SiN_x's electrical characteristics because it passivates dangling bonds in the bulk and the interface of the film. To date, the industry still adopts hydrogen to repair dangling bonds inside the dielectric film. Due to the high electric field and heat dissipation problem under operation environment, hydrogen atoms passivating the dangling bonds of dielectric film acquire enough energy to debond from their nearestneighboring atoms. Those dangling bonds then form free carrier trap centers and deteriorate the device's performance.

In addition, the content of hydrogen in the dielectric film also affects the morphology of the surface. The surface roughness can be measured by atomic force microscope. The rough surface may cause high surface recombination velocity and have a high defect density which deteriorates the properties of SiN_x film. The surface roughness may be affected by inadequate deposition condition, such as a high plasma power or high hydrogenation condition. It has been proven that thin-film transistor (TFT) mobility decreases with the increase of roughness of SiN_x surface in an inverted, staggered TFT(24). Also due to the high hydrogen composition, the etch rate of SiN_x is affected. The high hydrogen-content film has a higher etch rate than the low hydrogen-content film. The refractive index is related to the etch rate of the SiN_x. Figure 2-1 shows PECVD SiN_x etch rate vs. film refractive index and hydrogen content. The wet etch rate decreases with the increase of the film's refractive index(25).

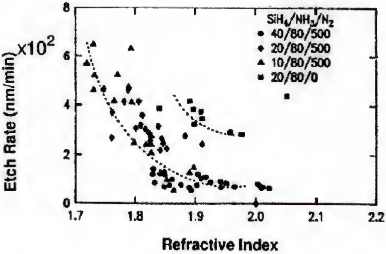

Figure 2-1. PECVD SiN_x etch rate vs. film refractive index and hydrogen content(25).

Due to the disadvantage of the hydrogen effect on SiN_x, lots of effort has been devoted to investigating how to minimize the hydrogen effect. Increasing in bombardment, obtained using diluted inert gas, can help to reduce hydrogen incorporation and to control film stress(26-28). In this study, we will try to reduce hydrogen content by modifying the precursor.

2.2 Dielectric Deposition With Different Techniques

2.2.1 Plasma-Enhanced Chemical Vapor Deposition (PECVD)

The motivation for using plasma enhanced deposition processes is that the substrate can be kept at low temperature, typically 300 °C or lower. This is achieved by reacting gases in a low discharge (plasma) which supplies much of the energy needed for the reaction. The plasma is created by applying a high electric field at a frequency of typically 13.56 MHz across the gas mixture. Due to their light mass, electrons acquire much higher kinetic energy during each cycle than do the ions. High-energy electrons then transfer energy to the gas molecules by impact and initiate a reaction which would have otherwise not been possible at low temperature. The properties of plasma deposited films depend on several variables such as electrode configuration and separation, power level and frequency, gas composition, pressure and flow rate and substrate temperature.

PECVD nitride films can be produced from silane and ammonia or nitrogen at 250-400 °C(29, 30). Unlike Si_3N_4 deposited at 750-900 °C, PECVD nitride films are not stoichiometric and depend strongly upon the method and deposition conditions. They typically contain excess silicon and large amounts (15-35 atomic %) of bonded hydrogen in form of Si-H, $Si\text{-}H_2$, $Si\text{-}H_3$, N-H and $N\text{-}H_2$(31, 32).

It is known that reducing temperature or eliminating NH_3 as a reactant tends to form films with many traps(33). Recently, however, there has been interest in depositing silicon nitride and other materials at low temperature (< 140 °C). As the temperature is reduced in plasma deposition, the energy required for desorbing hydrogen becomes less available, leading to more hydrogen incorporation and reduction of film density. One way to increase density and reduce the amount of hydrogen in PECVD silicon nitride is to use N_2 as a reactant instead of NH_3(34). The hydrogen content of nitride films deposited with N_2 at 250-300 °C is three times lower than that deposited with ammonia under similar conditions.

One important property of nitride films is stress. Nitride films can exhibit tensile or compress stress, depending on the deposition conditions and subsequent processing. For example, the stress of silicon nitride films depends on the rf chuck power, as shown in Figure 2-2(35). The temperature may also affect film stress, which is also important for device applications(36).

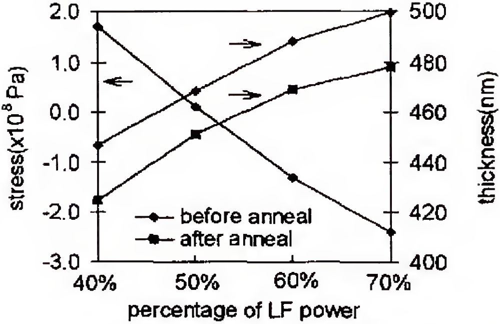

Figure 2-2. The stress and film thickness vs. percent of LF power for Novellus PECVD SiN_x. The deposition time is fixed(36).

2.2.2 Electron Cyclotron Resonant Chemical Vapor Deposition (ECRCVD)

The typical electron cyclotron resonant chemical vapor deposition (ECRCVD) is a remote plasma system and has two chambers, one is the ECR plasma generation and another is the sample position chamber where deposition occurs(37). Reactive radicals and ions are generated in the ECR source and diffuse into the deposition region. The electron resonance frequency created by the magnet around the ECR chamber is matched to the frequency (2.45 GHz) of the microwave plasma source thus, the microwave energy can efficiently incorporate into electrons. The energized electrons are confined inside the ECR zone colliding with gas molecules, therefore, the ion generation rates are much more efficient as compared to that of PECVD system. The ion densities for PECVD system are typical ~ 10^9 cm^{-3} and can be as high as 10^{12} cm^{-3} for the ECRCVD system.

This unique high ion density property of the ECR system results in many advantages over PECVD. First, nitrogen can be used as the N-precursor for SiN_x deposition, therefore, hydrogen content in the SiN_x film should be significantly reduced. Second, the high density ion bombardment can reduce the H concentration in the SiN_x film. Third, ion bombardment enhances the surface species migration, which will improve the step coverage and reduce the surface roughness. ECRCVD SiN_x has been shown far superior conformity of coverage around PHEMT T-gate contacts compared to that obtained with conventional rf-PECVD.

It is critically important to encapsulate the device with dielectric to protect it from scratches and improve the device stability. However, the additional dielectric layer will increase the gate parasitic capacitance and degrade the device RF performance. This is due to the higher dielectric constant of passivation layer compared to that of air.

2.2.3 Inductively Coupled Plasma Chemical Vapor Deposition (ICPCVD)

Inductively coupled plasma chemical vapor deposition(ICPCVD) can produce high ion density plasma conditions similar to that of ECRCVD, and can operate at higher pressure ($\geq$ 20 mTorr, instead of $\leq$ 5 mTorr in the ECR system). ICPCVD utilizes inductors to create a high density plasma in the processing reactor. This high pressure operation capability provides the deposition rates of 300-600 Å/min. This high deposition rate will reduce the exposure time of the intrinsic semiconductor surface to the ion bombardment during the deposition and may curtail the device damage. The ICPCVD has several advantages over the silicon nitride using the LPCVD and PECVD methods. The ICPCVD silicon nitride film can be deposited at much lower temperatures ($\leq$400 °C) than LPCVD silicon nitride, and has substantially less hydrogen (5.5 atomic %) than the PECVD film. In addition, PECVD film contains some oxygen in the film.

The wet-etch rate of ICPCVD silicon nitride is comparable to that of low-pressure chemical vapor deposition(LPCVD) film and is significantly less than that of PECVD film in both hot phosphoric acid and buffered HF solutions. The stress of the ICPCVD film is similarly compressive to the PECVD silicon nitride, and not as highly tensile as that of LPCVD silicon nitride(38). Some compared results are shown as Table 2-1 and Table 2-2.

Table 2-1 Elemental concentration of 1500 Å of silicon nitride films deposited using PECVD, LPCVD, and ICPCVD methods obtained using RBS and HFS(38).

		Atomic % concentration			
	Depth (Å)	Si	N	H	O
PECVD	0-600	35.2	41.3	19.5	4.0
	600-1500	34.9	45.6	19.5	-
LPCVD	0-1500	41.4	56.3	2.3	-
ICPCVD	0-1500	37.8	56.7	5.5	-

Table 2-2 Selected process and film properties of PECVD, LPCVD, and ICPCVD silicon nitride(38).

	PECVD	LPCVD	ICPCVD
Deposition rate (Å/min)	1800	300	960
Refractive Index	1.985	2.003	1.990
Stress (dyn/cm2)	-1.5×10^9	1×10^{10}	-3.8×10^9
Wet-etch rate in 85% H_3PO_4 (Å/min)	373	57	69
Wet-etch rate in 15:1 BHF (Å/min)	46.0	3.4	2.3

2.3 III-Nitride HEMT Properties

III-nitrides HFET structures mainly comprise of an interesting group of wide badngap materials such as AlGaN and GaN, which gets researchers' attentions in many semiconductor devices such as power amplifiers and microwave telecommunications. For example, III-nitride based devices conduct superior performance to those on other III-V compound semiconductor materials in terms of higher frequency operation, high output power handling, and high temperature operation. To date, high temperature transistors and high power, high frequency transistors have been demonstrated and the heterostructures are most commonly seen in these transistors and it gives devices more capabilities to reach outstanding performance.

The non-equilibrium energy bandgap structure of typical AlGaN/GaN HEMT is represented in Figure 2-3 and Table 2-3 presents band offset values at different III-nitride interfaces. Unlike other III-V compound semiconductors' structure, III-Nitride materials are normal wurtzite structure, and the growth direction is typically along the c-axis, so the relevant quantity is the one for the [0001] orientation on sapphire or SiC substrate by MOCVD or MBE. An initialization layer such as AlN or AlGaN is applied to nuclearize the epi-layer growth. Usually a thick buffer (~2μm) is grown in order to terminate the threshold dislocations propagate from nuclearlation layer into AlGaN/GaN interface. Because of the mismatch of lattice constant of AlGaN and GaN and polar properties of wurtzite structure, this makes a strain field and also polarization field at the AlGaN/GaN interface.

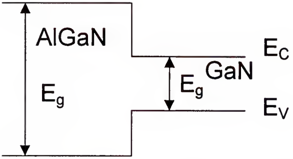

Figure 2-3. Energy band diagram for an abrupt heterojunction of AlGaN/GaN semiconductor materials.

Table 2-3. Valence(ΔV) and conduction band(ΔC) offset for III-nitride interfaces.

Interface	ΔV (eV)	ΔC (eV)	
AlN/GaN [0001]	0.8	2.05	(39)
AlN/GaN [0001]	0.5	2.4	(40)
AlN/GaN [0001]	1.36	1.5	(40)
AlN/GaN [110] cubic T	0.7	2.2	(42)
AlN/GaN [0001]T	0.57	2.3	(43)
AlN/GaN [0001]T	0.68	2.2	(44)
AlN/GaN [0001]	0.6	2.3	(45)
InN/GaN [0001]	0.93	0.6	(39)
GaN/InN [0001]	0.59	0.9	(39)
GaN/InN [0001]T	0.7	0.7	(44)
GaN/InN [110] cubic T	0.3	1.2	(42)
AlN/InN [0001]	1.32	3.0	(39)
InN/AlN [0001]	1.71	2.6	(39)
AlN/SiC [001] cubic T	2		(46)
AlN/SiC [110] cubic T	1.6		(46)
GaN/SiC [001] cubic T	1.3		(46)
GaN/SiC [110] cubic T	0.4		(46)

2.3.1 Polarization Fields

There are two kinds of polarization effects, one is spontaneous polarization and the other is piezoelectric polarization, which make of the total polarization field on the AlGaN or GaN layers. The spontaneous polarization is very sensitive to the symmetrical structure in semiconductors therefore, a wurtzite or lower symmetry crystal structure usually possess higher spontaneous polarization field than cubic or zinc blende structure does(47). In wurtzite lattice structure, this spontaneous polarization field is along a fixed direction along [0 0 0 1] c-axis and can be written as

$$\vec{P_{SP}} = P_{SP} \bullet \vec{c} \tag{2-1}$$

where P_{SP} is the scalar value of the polarization. The available data for the spontaneous polarization in the III-nitrides are collected in Table 2-4.

Table 2-4. Lattice constants (a_0, c_0), microscopic dimensionless parameter (μ), spontaneous polarization (P_{SP}), piezoelectric (e_{ij}) and dielectric (ε_{ij}) constants of AlN, GaN and InN.

Wurtzite	AlN	GaN	InN
a_0 (Å)	3.112	3.189	3.54
c_0 (Å)	4.982	5.185	5.705
c_0/a_0	1.601	1.627	1.612
	1.619 (48)	1.634 (48)	1.627 (48)
μ	0.380 (48)	0.376 (48)	0.377 (48)
P_{SP} (C/m^2)	-0.081 (48)	-0.029 (48)	-0.032 (48)
e_{33} (C/m^2)	1.46 (48)	0.73 (48)	0.97 (48)
	1.55 (49)	1 (50)	
		0.65 (51)	
	1.29 (52)	0.63 (52)	
e_{31} (C/m^2)	-0.60 (48)	-0.49 (48)	-0.57 (48)
	-0.58 (49)	-0.36 (50)	
		-0.33 (51)	
	-0.38 (52)	-0.32 (52)	
e_{13} (C/m^2)	-0.48 (49)	-0.3 (50)	
		-0.33 (51)	
ε_{11}	9.0 (49)	9.5 (53)	
ε_{13}	10.7 (49)	10.4 (53)	14.6 (54)

For the alloys P_{SP} may be estimated by a simple interpolation procedure according to a Vegard-like rule. So for the general case of $Al_XIn_YGa_{1-X-Y}N$, P_{SP} can be computed approximately for the polarization from the following expression:

$$P_{SP}(X,Y) = X \cdot P_{SP}^{AlN} + Y \cdot P_{SP}^{InN} + (1 - X - Y)P_{SP}^{GaN} \tag{2-2}$$

Figure 2-4 shows how P_{SP} varies across the entire AlGaInN materials system, according to theoretical calculations by Fiorentini et al(55). From the figure, spontaneous polarization effects play an important role for Al-containing structures, while in Ga-In-N structures the influence of spontaneous polarization fields is less obvious.

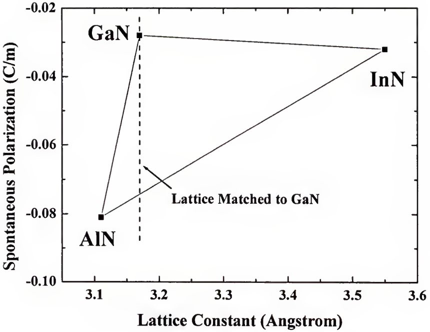

Figure 2-4. Theoretically calculated spontaneous polarization in the $Al_XIn_YGa_{1-X-Y}N$ alloy system, according to a Vegard-like rule(55).

Another important component of the polarization fields in III-N HEMT structures is the piezoelectric polarization. Because of differences in the lattice parameters of III-nitride materials, AlGaN/GaN multilayer structures based on this system are found to be strained. Most of the strain occurs due to the difference in thermal expansion coefficients, which causes elastic strain to develop in the layers during cool down after growth(56). The difference between two materials in the interface usually contributes a net charge caused by macroscopic polarization field, especially in III-nitride group since these polarization fields are very significant.

2.3.2 two DEG in AlGaN/GaN Heterojunction

$Al_XGa_{1-X}N$ grown on a GaN buffer layer with different composition X are very interesting for Heterojuncion Field Effect Transistor(HFET) applications(57). As point out in section 2.3.1, this material system has very strong coefficients for both spontaneous and piezoelectric polarization, and these effects will drastically influence the potential across the structure. Depending on the polarity of AlGaN/GaN interface, two different cases are expected to occur, one is Ga terminated face and the other is N terminated face as shown in Figure 2-5. When a GaN buffer layer is grown on sapphire by MOCVD, the surface is typically found to be Ga face as shown in Figure 2-5(left). However, in MBE growth, the growth of the same layer with polarity is typically N-face (Figure 2-5, right). Therefore, the spontaneous polarization induced charge at the interface will be opposite.

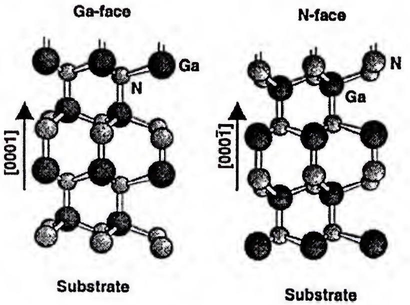

Figure 2-5. Schematic drawing of the crystal structure with surface termination of wurtzite Ga-face and N-face GaN(58).

The polarization fields are explained in more detail in either Ga face or N face in Figure 2-6. For Ga terminated case, it was found that a positive fixed interface charge σ is created by the difference of total polarization between GaN and AlGaN:

$$\sigma = \Delta P = (P^{AlGaN} - P^{GaN}) = (P_{SP}^{AlGaN} + P_{PZ}^{AlGaN}) - (P_{SP}^{GaN} + P_{PZ}^{GaN}) \qquad (2\text{-}3)$$

By putting in numbers into this equation, high sheet charge density of the order $10^{13}cm^{-2}$ is obtained. The interface charge may easily attract electrons from AlGaN cap layer, GaN buffer layer or from a top metal contact at elevated growth or processing temperatures, so that a two-dimensional electron gas (2DEG) is formed betweem AlGaN/GaN interface. This is a very important property of an AlGaN/GaN heterojuncion, since it allows the formation of a dense 2DEG in an undoped region without modulation doping of the AlGaN barrier.

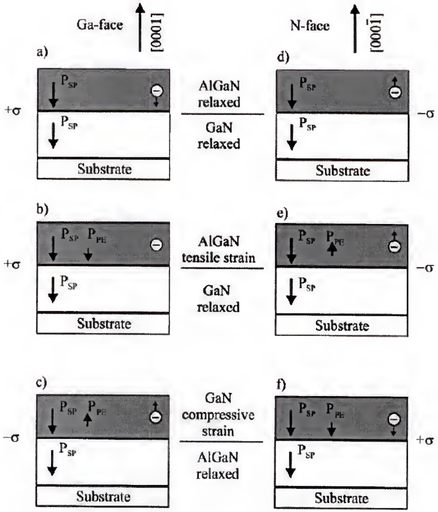

Figure 2-6. Polarization induced sheet charge density and directions of spontaneous (P_{SP}) and piezoelectric (P_{PE}) polarization in Ga- and N-face strained and relaxed AlGaN/GaN heterostructures(58).

On the other hand, the N terminated face will reverse the polarity and this operation not only reverses the spontaneous field, but also the piezoelectric field which provided the strain field remains the same. In order to maintain a 2DEG in an N-face structure, a second thin GaN layer has to grown on top of the AlGaN. The upper AlGaN/GaN interface will then have 2DEG in the GaN layer close to the interface. In Figure 2-7, the fixed polarization induced interface charges and compensating free carrier populations are shown in the case of Ga face HFET structure.

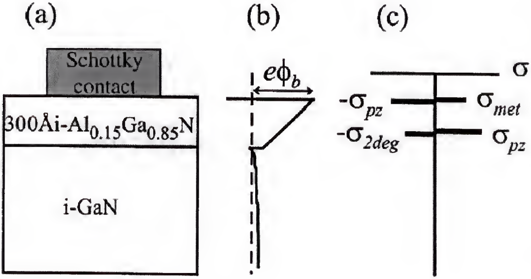

Figure 2-7. (a) Schematic diagram of a nominally undoped Al0.15Ga0.85N/GaN heterostructure field-effect transistor structure. (b) Conduction-band energy diagram; the dash line represents the Fermi level and $e\Phi_b$ is the Schottky barrier height. (c) Schematic diagram of polarization induced σ_{PZ} and free-carrier charge distribution σ_{2DEG}(59).

In order to solve potential profile across AlGaN/GaN interface, the Schrodinger equation and the Poisson equation are solved simultaneously with appropriate boundary assumption. Polarization induced electron charge density can be calculated by the following equation(60):

$$n(x) = \frac{\sigma(x)}{e} - (\frac{\varepsilon^{'} \hat{o} \varepsilon(x)}{de^{2}})[e\Phi_{b}(x) + E_{F}(x) - \Delta E_{C}(x)] \tag{2-4}$$

where the variable x is the Al concentration of $Al_XGa_{1-X}N$. ε represents the dielectric constant, σ the fixed polarization-induced charge, Φ_b the Schottky barrier height, d the thickness of the AlGaN layer, E_F the Fermi energy at the AlGaN/GaN interface with reference to the GaN conduction band edge, and ΔE_C the conduction band offset at the AlGaN/GaN heterojunction. Fermi energy $E_F(x)$ is a function of n(x)(58):

$$E_{F}(x) = [\frac{9\pi\hbar e^{2}}{8\varepsilon_{0}\sqrt{8m_{e}(x)}}\frac{n(x)}{\varepsilon(x)}]^{2/3} + \frac{\pi\hbar^{2}}{m_{e}(x)}n(x) \tag{2-5}$$

where $m_e(x)$, the effective electron mass, is 0.22 in GaN. Combining these equations it is possible to compute the induced electron concentration in the notch potential close to the AlGaN/GaN interface. From the equations, calculated sheet carrier concentrations of 2DEG in AlGaN/GaN structure is shown in Figure 2-8. Sheet electron concentration of $10^{13}cm^{-2}$ can readily obtained in these structures. One thing to be noticed is that there is no doping layer in the structure, the carrier accumulation in the 2DEG is mainly as a result of macroscopic polarization field. Capacitance-Voltage carrier concentration profile measurements may be used to measure the carrier profiles and to verify the presence of a 2DEG as shown in Figure 2-9.

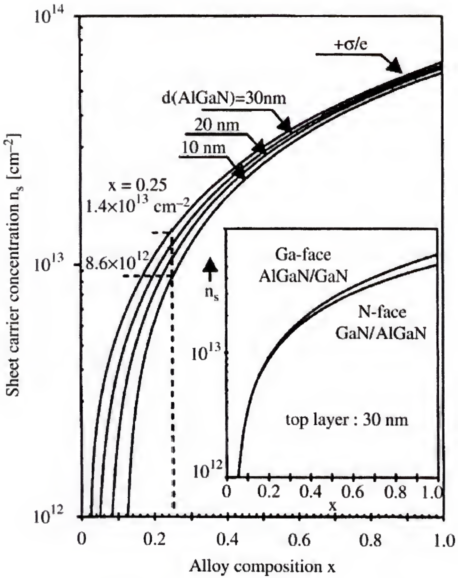

Figure 2-8. Calculated sheet carrier concentrations of the 2DEG confined at a Ga-face or N-face interface for different thickness of the AlGaN barrier and different composition X. The inset shows the maximum sheet carrier concentration of the same pseudomorphically grown Ga-face AlGaN/GaN and N-face GaN/AlGaN heterostructures(58).

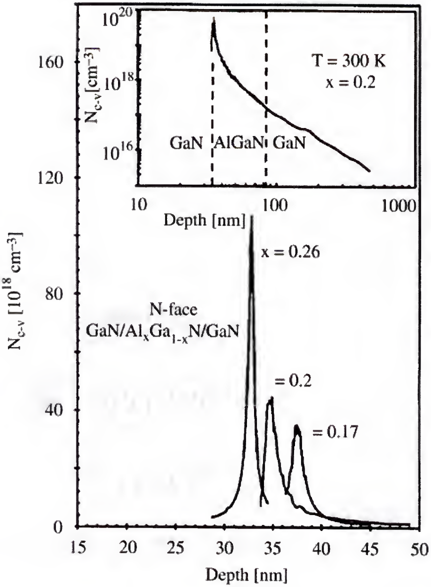

Figure 2-9. *CV*-concentration profile N_{C-V} vs. depth from the surface of GaN/Al$_x$Ga$_{1-x}$N/GaN heterostructures grown by plasma induced MBE with Al-contents of the barrier between x= 0.17 and 0.26 measured by the *C-V* profiling technique. The insert shows N_{C-V} vs. depth on a logarithmic scale for a heterostructure with an alloy composition of x"0.2. The 2DEG is located at the upper GaN/AlGaN interface(58).

2.3.3 Electron Mobilities in AlGaN/GaN heterojunction 2DEG

Two key factors for achieving a good channel conductance of HFET devices are a high sheet electron concentration and a high electron mobility. Several different scattering mechanisms are related to electron mobility in AlGaN/GaN material system. Ideally, the electron mobility is only a function of optical phonon scattering at room temperature. However, in practical case, with the presence of varied defects inside the material, it limits the mobility even at room temperature.

The various mechanisms which limit the electron mobility in an AlGaN/GaN Heterojunction structure can be summarised as follows in terms of the different scattering times τ_i for electron scattering⁽²⁸⁾:

$$1/\tau_{tot} = 1/\tau_{ph} + 1/\tau_{imp} + 1/\tau_{alloy} + 1/\tau_{\text{int}} + 1/\tau_{disl} \qquad (2\text{-}6)$$

where τ_{ph} denotes scattering with phonons, which includes several mechanisms: deformation potential and piezoelectric scattering with acoustic phonons, and polar optical phonon scattering. τ_{imp} is the Coulomb scattering with impurities, i.e. dopants and other charged defects, τ_{alloy}: denotes the scattering with alloy potential fluctuations at the interface, τ_{int} represents the influence of the roughness of the interface, and finally a separate process τ_{disl} is the dislocation scattering, which may need to be considered, since in most structures produced so far dislocation densities are high. The electron mobility in an $Al_XGa_{1\text{-}X}N$/GaN HFET was shown in Figure 2-8$^{(61)}$. At the room temperature, mobility is dominant by optical phonon scattering$^{(65,\ 63)}$, while at lower temperatures several scattering mechanisms will contribute. To date the best electron mobility at room temperature is just above 2000 $cm^2/V\text{-}s^{(64)}$. A limiting low temperature mobility as high as 10^6 cm^2/V s is predicted for low impurity and defect concentrations as shown in Figure 2-10$^{(61)}$. The highest low temperature mobility reported is 50000 $cm^2/V\text{-}s^{(65)}$, implying the immaturity of the quality of materials from the modern growth technology.

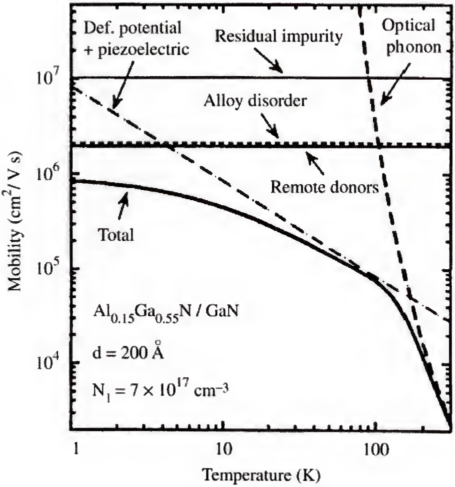

Figure 2-10. Temperature dependence of the mobility in an $Al_{0.15}Ga_{0.85}N$/GaN modulation doped heterostructure. All curves are calculated mobilities. The 2DEG density for this case is $6.2\times10^{11}cm^{-2}$ and the concentration of residual ionized impurities in the GaN is $1\times10^{14}cm^{-3}$ (61).

It is also know that threading dislocations in III-nitride structures are generally electrically active(66), and will behave as a charge in the active region of an AlGaN/GaN heterostructure. It has been demonstrated for GaN films that the dislocation density correlates with a low mobility in samples which are not too highly doped(67). In Fig. 2-11 the experimental data for MBE grown GaN layers, demonstrating this dependence is shown(68, 69). A charged dislocation line will be an efficient electron scatterer, and will reduce the mobility of a 2DEG if the dislocation density is sufficiently high. It has recently been estimated that a dislocation density below 10^8 cm^{-3} is needed in order to minimize the influence of dislocations on the room temperature electron mobility in these structures(67, 69). In addition these dislocations will trap carriers from the 2DEG into deep states in the bandgap, lowering the 2DEG density in a device structure, which is another undesired consequence of these defects.

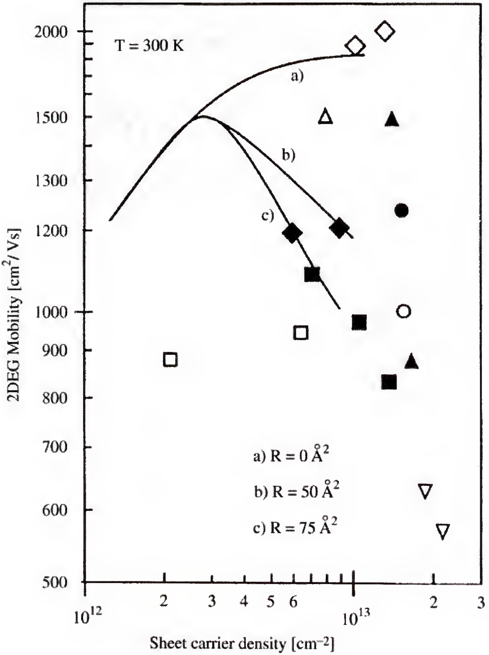

Fig. 2-11. Calculated and measured 2DEG mobility vs sheet carrier concentration for a collection of samples with different AlGaN/GaN interface roughness(58).

2.3.3 Current Collapse

Based on the unique properties of AlGaN/GaN HFET structures such as high 2DEG carrier density, high electron mobility, AlGaN/GaN based structure can operate under high current driving condition. In addition, due to higher bandgap energy, the forward operation region is at least an order of magnitude higher than compared to that of than Si and other compound semiconductor like GaAs or InP. Summarization of these two advantages gives AlGaN/GaN based HFET the capability to deliver high power throughout and it was widely employed for power amplifier application in wireless telecommunication and high power plant business, especially focusing on X band (8-12GHz) and Ku band (12-18GHz) high frequency band application(70).

Under these high power operation conditions, thermal dissipation becomes an issue to be aware of, otherwise, the increase of substrate temperature causing an unexpected decrease in electron mobility in 2DEG. In consequence, a severe degradation in drain-source current at forward gate voltage near knee voltage and a positive slop of I_{DS} as a function of V_{DS} is observed. This degradation in I_{DS} is recoverable as substrate temperature cools down. Several different solutions are proposed to solve this thermal degradation problem. By choosing high heat conductivity substrate such as SiC instead of sapphire, so generated heat can be effectively conducted away from active region of the devices. Besides, lapping the backside of substrate and flip-chip mounted to a large volume carrier can also mitigate the thermal problem effectively.

However, one of the vital disadvantage hampers the use of GaN HEMT is the unstable surface traps on the top of HEMT structures. Since the 2DEG is mainly resulted from spontaneous polarization and piezoelectric field, any negative charged surface states such as dangling bonds or point defects will compensate any polarization charges on the surface and result in a decrease in 2DEG electron density(71). This surface states play a role in GaN HEMT dc/rf output performance by acting as a virtual gate(56) as shown in Figure 2-12.

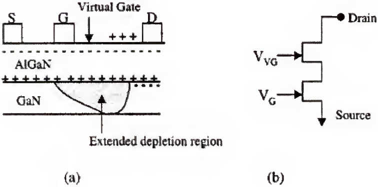

Figure 2-12. Model of the device showing the location of the virtual gate and schematic representation of the device including the virtual gate(72).

The presence of virtual gate deteriorates the drain-source current under the same bias condition as well as output power due to the large time constant of surface traps. Therefore, the drain-source current can not follow ac signal applied to gate terminal. These surface states are revealed themselves under pulsed bias condition such as gate-lag or drain-lag(73-76). The setup of gate lag and drain lag measurement are shown in Figure 2-13. In the gate lag setup as shown in Figure 2-13 (left), the pulse bias source is connected to the gate electrode and keeps the drain electrode biased with dc bias source. In the drain lag setup, the dc and pulse bias source are switched as shown in right of Figure 2-13.

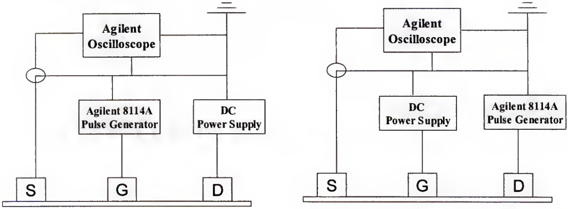

Figure 2-13. The equipment setup of gate lag (left) and drain (right) measurement.

It has been found that the gate lag measurement is more related to the surface states on the surface in the high electric field between gate and drain. The pulse frequency is higher than the time constant of surface traps, therefore, at the slow pulse frequency region, the pulsed drain-source current can follow ac gate signal and conduct better match with dc IV characteristics. In Figure 2-14, the pulsed I_{DS} is obvious found out as a function of pulse frequency. The higher the pulse frequency, the lower the pulsed I_{DS}. Besides, the pulsed I_{DS} also changes corresponding to different substrates. A less bulk defect density is expected for epilayer grown on SiC substrate than sapphire substrate. In Figure 2-15, pulsed I_{DS} on a SiC substrate is superior to that on a sapphire substrate. In addition, shorter the gate will experience higher electric field and cause a higher negatively charges density accumulated.

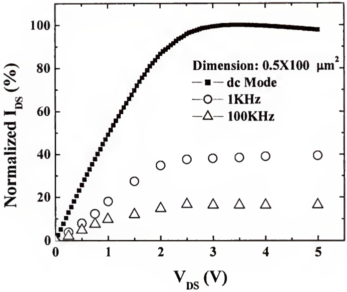

Figure 2-14. Comparison of pulsed I_{DS} and dc I_{DS}. Pulsed I_{DS} as a function of pulse frequency due to slow surface states.

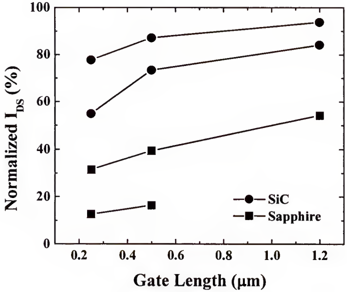

Figure 2-15. Gate lag measurement as functions of gate length as well as substrates.

In order to solve this current collapse problem, PECVD deposited SiN_X is widely used(77). After successfully passivating surface traps, the output power performance is increase dramatically as shown in Figure 2-16(76).

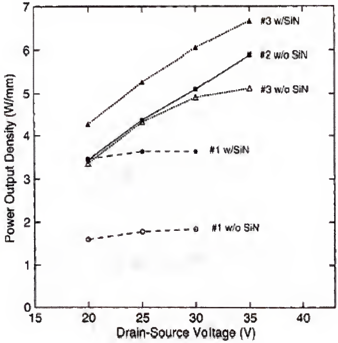

Figure 2-16. Pulsed power output dependence on drain-source voltage. The results are obtained on devices from three different wafers(76).

Although the I_{DS} is independent of ac frequency of gate signal after silicon nitride passivation, there are still several issues need to be concerned. One of the issues is the reduction in three terminal breakdown voltage. Three terminal breakdown voltage is defined as the forward operation region in which power amplifier can operate without severe gate leakage current occur. A gate leakage current is usually observed after silicon nitride deposition. Several hypotheses are proposed to explain this phenomenon such as creating leakage passes in the SiN_X film. Another possible reason is because the breakdown voltage is smaller if only a thin layer of SiN_X put down on the surface(77).

Karmalkar, S. et. al.(78) effectively increase the forward breakdown voltage by adding a field plate between gate and drain as shown in Figure 2-17, which can moderate the electric field at the edge of gate contact(Figure 2-18).

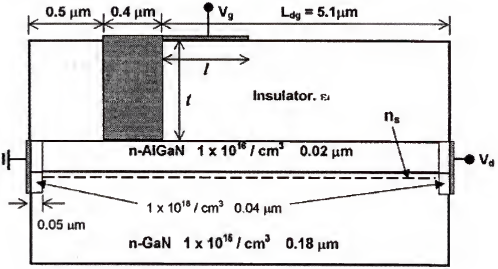
0.5 μm
0.4 μm
V_g
L_{dg} = 5.1μm
l
t
Insulator, ε_i
n_s
n-AlGaN 1 x 10^{18} / cm^3 0.02 μm
V_d
1 x 10^{18} / cm^3 0.04 μm
0.05 um
n-GaN 1 x 10^{15} / cm^3 0.18 μm

Figure 2-17. FP-HEMT structure; the particular dimensions and doping values employed for simulation in this paper are also shown. Although not shown here, a 0.3μm-thick dielectric medium above the field plate is used in all our simulations(78).

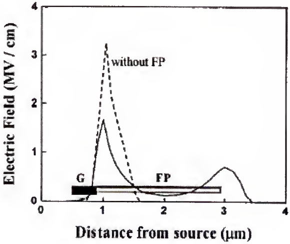

Figure 2-18. Simulated distribution of the electric field along the 2-DEG, directed from drain to source, without and with a FP (t = 0.3 μm silicon nitride, l = 2 μm); n = 1×10^{13} /cm^2 and V_d, V_g = 123, -2.8 V. The device without FP is on the verge of breakdown(78).

CHAPTER 3
III-V COMPOUND SEMICONDUCTOR DEVICES FABRICATION

3.1 p-Ohmic Contact Study for Intra-Cavity Contacts in AlGaAs/GaAs Vertical-Cavity Surface-Emitting Lasers

The effects of metallization and annealing temperatures on p-ohmic contacts for 850nm AlGaAs/GaAs vertical-cavity surface-emitting laser were investigated. Different metallization containing AuBe, Pt, Pd, Ti, Ag, and Au were used. The AuBe/Au and Pd/AuBe/Pt/Au based metallizations showed the lowest specific contact resistances. For an annealing temperature of 400°C, specific contact resistances of these metal schemes reached 4×10^{-6} Ω-cm^2. The thermal stability of the contacts was also investigated. The contacts did not display degradation for temperatures up to 450°C

3.1.1 Intordution

Low device resistance is essential for high-speed performance in vertical-cavity surface-emitting lasers (VCSELs)(79-83). Intra-cavity contacts are contacts formed to semiconductor layers inside the optical cavity of the VCSEL. In order to use the dielectric distributed Bragg reflectors, intra-cavity contacts are needed inside the optical cavity of VCSEL. Intra-cavity contacts have been demonstrated for very low contact resistance in high-speed shallow-implanted 980 nm VCSELs(84). For these devices, contacts were made to highly-doped GaAs layers. For the case of 850 nm VCSEL, the contact has to be formed on AlGaAs layers and it became more challenging. The $Al_xGa_{1-x}As$ materials system oxidizes faster than GaAs and this makes the preservation of an oxide-free AlGaAs surface for the ohmic contact formation much more difficult(85).This task becomes even more complicated for ion-implanted, index-guided or I^2 VCSELs, when ion-implantation is used to define the current aperture(86). Typically, ion-implantation is performed prior to contact formation. Implantation is through the p-ohmic contact layer and places the peak of the damage within the cladding layer to confine the current injection. Although the peak of the implant profile lies about 1500 Å into the device structure, the implant profile does extend to the surface layers for the p-ohmic metallization formation region. Therefore an increase of p-contact resistance can be expected due to carrier reduction from ion implantation.

In this work, we examined effects of metallization, annealing temperature, and different semiconductor contact layers for forming intra-cavity p-ohmic contacts in to AlGaAs 850 nm VCSELs. The metallization schemes of AuBe/Ag/Au, AuBe/Pt/Au, Pd/Ti/Pt/Au, AuBe/Au and Pd/AuBe/Pt/Au were examined.

3.1.2 Experimental

The VCSEL epitaxial layers were grown by metal organic chemical vapor deposition (MOCVD) on semi-insulating GaAs substrates. The bottom semiconductor DBR mirror consisted of 30 pairs of AlAs/AlGaAs quarter wavelength layers. A p-i-n structure was employed inside the device cavity, with carbon as the p-type dopant and silicon as the n-type dopant. The top part of VCSEL including index guide, p^+-ohmic contact layers, and current spreading layer is shown in Figure 3-1.

Both as-grown and implanted samples were used in the study. The implant condition employed in this study is the exact implant condition used in our standard 850 nm VCSEL process(87). Oxygen was used as implanted ions. The typical dose and energy are $1.5\times10^{12}cm^{-2}$ and 180keV, respectively. Prior to loading the samples into the metal deposition chamber, the undoped $In_xGa_{1-x}P$ and $Al_yGa_{1-y}As$ layer were etched in

$HCl:H_2O$ and $H_3PO_4:H_2O_2:H_2O$ wet etch solution, respectively. This was followed by a short etch in $NH_4OH:H_2O$ (1:20) for 1 minute to remove native oxides on the carbon-doped AlGaAs contact surface. This helps to ensure uniform contact properties upon subsequent deposition and alloying of the contacts. InGaP is more resistant to the oxidation than AlGaAs. For some of the samples, the undoped InGaP was not etched and the ohmic metallizations were directly deposited on the InGaP.

Various contact metallization schemes were studied which included AuBe/Ag/Au, AuBe/Pt/Au, Pd/Ti/Pt/Au, AuBe/Au and Pd/AuBe/Pt/Au. The metals were deposited using e-beam evaporation and standard lift-off process. A thin layer of titanium was deposited on the top of Au, when AuBe was used in the metallization scheme. This Ti layer was etched off in BOE prior to the metal lift-off. This step was used to remove any Be that has segregated on the surface of the metal stack during metal deposition. Any Be left on the surface can form BeO_x that will create higher resistance contacts(88). After the metal lift-off, the metallized samples were then annealed in a N_2 ambient at temperatures of 300~450°C for 30 sec in a rapid thermal annealing (RTA) system.

The transmission line method (TLM) was employed to estimate the contact resistance(R_C), sheet resistance(ρ_S), and specific contact resistance(ρ_C). The TLM patterns were formed and patterned along with the contacts. The pad spacings were 2, 4, 8, 16 and 32 μm, with the pads dimension of 100×100 μm^2. The TLM measurementswere conducted with an HP 4145B parameter analyzer.

3.1.3 Results and Discussion

As illustrated in Figure 3-1, the p^{++}-highly doped ($\sim10^{20}$ cm^{-3}) $Al_yGa_{1-y}As$ ohmic contact layer is below an undoped $Al_yGa_{1-y}As$ index guide, an undoped InGaP etch stop and a p^+-$Al_yGa_{1-y}As$ optical spacer layer. The index guide layer is to improve the optical gain and the etch stop layer is used for the selective removal of the index guide outside the aperture region. This optical spacing layer is to place the p^{++}-$Al_yGa_{1-y}As$ ohmic contact layer at the nodes of the optical cavity standing wave to minimize free carrier absorption in the p^{++}-$Al_yGa_{1-y}As$ layer. In order to obtain the low contact resistance, all these three top layers should be etched off prior to the ohmic metal deposition. The first two layer can be easily etched off with selectively wet chemical solution(89). However, the p^+ spacer and p^{++} ohmic contact layer have the same composition. Therefore, it is impossible to etch off the p^+-$Al_yGa_{1-y}As$ spacing layer and stop right on the p^{++}-$Al_yGa_{1-y}As$ ohmic contact layer reproducibly. Thus an alloyed ohmic metallization is required to diffuse through the p^+-$Al_yGa_{1-y}As$ spacing layer and form an ohmic contact on p^{++}-$Al_yGa_{1-y}As$. Be is a p-dopant for GaAs and AuBe based metallizations can achieve this goal.

~300 Å	**undoped**	**$\sim Al_{0.2}Ga_{0.8}As$**
~300 Å	**undoped**	**$In_XGa_{1-X}P$**
~300 Å	**P^+**	**$\sim Al_{0.2}Ga_{0.8}As$**
~300 Å	**P^{++}**	**$\sim Al_{0.2}Ga_{0.8}As$**
≈		≈
~1000 Å	**P**	**$\sim Al_{0.2}Ga_{0.8}As$**
~300 Å	**P^{++}**	**$\sim Al_{0.2}Ga_{0.8}As$**

Figure 3-1. The first six layers on the top of VCSEL.

To form good p-ohmic contact, not only do we have to consider the effect of index guide, etch stop, and optical spacer layer on p^{++}-$Al_yGa_{1-y}As$ but also the layer beneath it. A key feature in the lateral current injection VCSEL design is the use of low doped p-$Al_yGa_{1-y}As$ layers to sandwich another thin highly doped p^{++}-$Al_yGa_{1-y}As$ layer for current spreading. This current spreading layer is directly under the p^{++}-$Al_yGa_{1-y}As$ ohmic contact layer. The purpose here is to allow the current to spread uniformly across the current aperture since the central low-doped layer provides some resistance in the vertical direction. Without this type of structure the current would flow along the periphery of the aperture, resulting in poor efficiency and preferential pumping of higher order modes. This current spreading layer is right under the p^{++}-$Al_yGa_{1-y}As$ ohmic contact layer. Therefore it is very important to control the diffusion depth of AuBe to stop right at the p^{++}-$Al_yGa_{1-y}As$ ohmic contact layer and avoid penetration into the p-$Al_yGa_{1-y}As$ current spreading layer. This can be achieved by optimizing the ohmic metallization, ohmic contact annealing temperature and time.

Different combinations of AuBe(90), Au, Pt(91), Ag, Ti, and Pd(92, 93) were used in our studies. AuBe was used for the ohmic formation. Be served as p-dopant and diffused into AlGaAs through annealing. Au was utilized as the top contact layer to reduce the metal resistance. Pt and Ag were employed as the diffusion barrier. Without this Pt or Ag layer, the top Au contact layer can form deep Au spikes (around 300 to 400 nm) in the semiconductor and these spikes behave as mini-Schottky contacts(88, 94). Auger depth profiles of as deposited and annealed Ti/Pt/Au and AuBe/Ag/Au samples (annealed at 400°C for 30 sec) are illustrated in Figure 3-2 and 3-3, respectively. There was no metal inter-mixing at all when Pt was used as diffusion barrier, however, there was slight interaction among Au/Ag/AuBe. However, there was no obvious Au penetration into the semiconductor. Figure 3-4 shows the TEM of annealed AuBe/Au metal contact. In this case, there was no diffusion barrier employed and deep Au spikes were clearly observed.

Pd is typically used as a wetting agent to dissolve native oxides on the semiconductor surface. Ti was used for adhesion in Ti/Pt/Au metallization and top Be removal layer for the other metallizations.

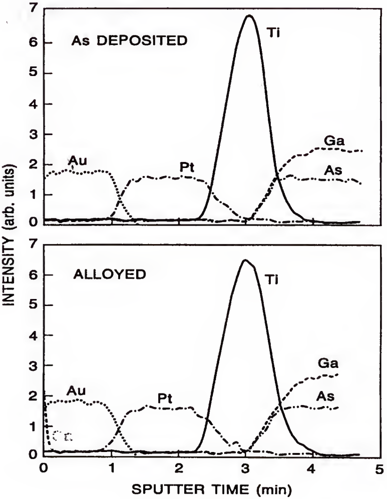

Figure 3-2. Auger depth profiles of as-deposited and annealed Ti/Pt/Au samples (annealed at 400°C for 30 sec).

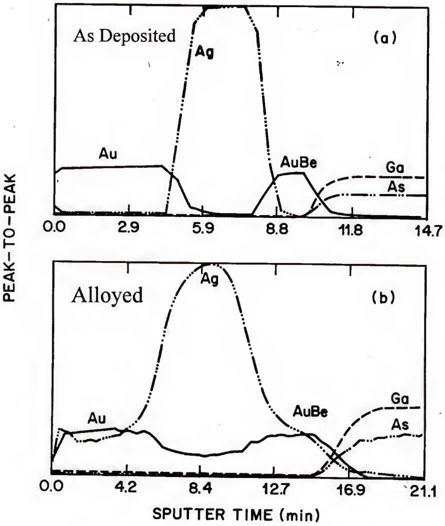

Figure 3-3. Auger depth profiles of as-deposited and annealed AuBe/Ag/Au samples (annealed at 400°C for 30 sec).

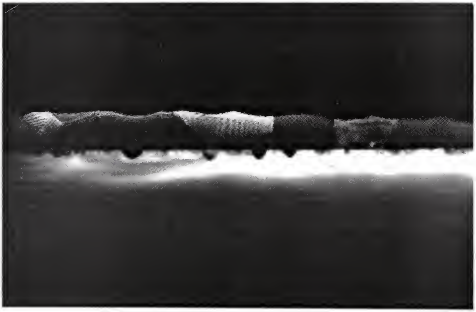

Figure 3-4. TEM of annealed AuBe/Au metal contact.

The as-deposited contacts of all the metallizations have Schottky characteristics and some of them showed ohmic behavior after annealing to 300~350°C. Once the annealing temperature was increased to 400°C, the specific contact resistances greatly improved to 10^{-5}~10^{-6} Ω-cm^2, as shown in Figure 3-5. For anneal temperature reaching 450 °C, the specific contact resistivity slightly reduced further, as shown in Table 3-1.

In general, the contact resistances are higher for the implanted samples due to the ion bombardment damage introduced to the p^{++} contact layer during the aperture definition implantation. Table 3-1 also contains the information on the effects of Pd and contacts directly deposited on InGaP instead of AlGaAs on the specific contact resistivity. As mentioned previously, Pd is used as a wetting agent to dissolve native oxides on the semiconductor surface and allow AuBe to diffuse into the p^{++}-$Al_yGa_{1-y}As$ forming low resistant contacts. The as-deposited and annealed samples at 350 °C showed ohmic characteristics. The metallization consisting of Pd and AuBe as the first two layers showed the lowest specific contact resistivity. The samples with contact metal deposited

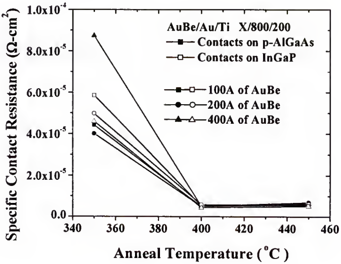

Figure 3-5. Specific contact resistance of contact with varied AuBe thickness as a function of anneal temperature

Composition		350°C	400°C	450°C
AuBe/Ag/Au/Ti *	No implant	Schottky	10.8	8.0
400/300/800/200	Implant	Schottky	7.4	14.7
AuBe/Pt/Au/Ti *	No implant	Schottky	50.3	13.4
400/300/800/200	Implant	Schottky	55.8	22.2
Pd/Ti/Pt/Au *	No implant	Schottky	33.2	9.9
50/200/300/800	Implant	Schottky	112	10.7
AuBe/Au/Ti *	No implant	87.4	5.2	6.5
400/800/200	Implant	Schottky	7.5	13.5
Pd/AuBe/Pt/Au/Ti *	No implant	10.2	4.2	5.6
50/400/300/800/200	Implant	580	6.1	4.1
AuBe/Au/Ti #	No implant	46	4.4	5.0
400/800/200	Implant	Schottky	9.7	4.4

The specific contact resistance is in the scale of 10^{-6} Ω-cm^2.

*: Contacts were on top of p-AlGaAs.

#: Contacts were on top of InGaP.

Table 3-1. Specific contact resistance of different metallic compositions at varied annealing temperature.

directly on the InGaP also showed lower resistance as compared to that on p-AlGaAs. Semiconductor surface native oxides hinder the ohmic formation between the contact metal and semiconductor. Since, InGaP is more resistant to oxidation than AlGaAs, the lower contact resistance should be expected with the samples having metal directly on the InGaP layer.

The effect of AuBe thickness on specific contact resistivity was also studied and is shown in Figure 3-6. The optimal thickness of AuBe is around 200 – 400 Å. 100 Å AuBe was not enough to penetrate through the p^+-$Al_yGa_{1-y}As$ optical space layer to the p^{++}-$Al_yGa_{1-y}As$ layer. 800 Å AuBe was too much and AuBe reached the low doped p-$Al_yGa_{1-y}As$ current spreading layer and destroyed the current spreading.

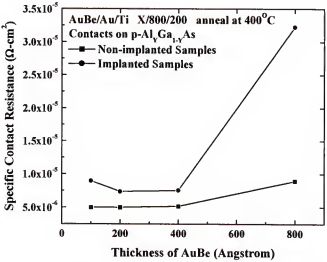

Figure 3-6. Specific contact resistance of contact with and without oxygen implantation as a function of AuBe Thickness.

Various p-ohmic contact metallizations were investigated in our study. By evaluating specific contact resistance and contact resistance, Pd/AuBe/Pt/Au/Ti based metallization had better results than other combinations. The effect of AuBe thickness and annealling temperature were also investigated and the optimal metal thickness and annealing temperature are 200-300 Å AuBe and 400 °C, respectively.

3.2 High Breakdown M-I-M Structures on Bulk AlN

The breakdown characteristics of metal-AlN-metal structures are reported as a function of contact diameter. The bulk AlN was grown by a HVPE method, resulting in a resistivity of $10^8 \Omega$cm. Front-side contact diameters of 175-600μm were fabricated, displaying breakdown voltages up to ~6300V at 25°C. Breakdown appeared to initiate at internal surfaces related to grain boundaries or cracks in the material. The results indicate the great promise of the Al(Ga)N system for high power rectifiers.

3.2.1 Introduction

There is a strong interest in developing wide bandgap power devices for use in the electric power industry(95-98). As this industry continues to be de-regulated, there are increasing numbers of transactions on the power grid in the US. A major problem in the current grid is momentary voltage sags, which affect motor drives, computers and digital controls. A system for eliminating power sags and switching transients would dramatically improve power quality. Some desirable attributes of next generation, widegap power electronics include the ability to withstand current in excess of 5kA and voltages in excess of 25kV, provide rapid switching, maintain good thermal stability while operating at temperature above 250°C without bulky heat-dissipating systems. In particular, the absence of Si devices capable of application to 13.8kV distribution lines (a common primary distribution mode) opens a major opportunity for widegap electronics. The AlGaN materials system is attractive from the viewpoint of fabricating unipolar power devices such as rectifiers because of its large bandgap and relatively high electron mobility. A number of groups have reported excellent high breakdown performance from both lateral and vertical geometry GaN and AlGaN Schottky and p-i-n rectifiers, both for epilayers grown on sapphire substrates and for free-standing GaN quasi-substrates(98-107). While lateral rectifiers on epi AlGaN have shown reverse breakdown voltages up to 9.7kV(105), the maximum breakdown in free-standing GaN is ~700V(107).

In this letter, we report on the breakdown characteristics of free-standing AlN substrates. This data gives some idea of the voltage-handling capability of the nitride materials system at the extreme of bandgap (i.e. pure AlN). Since this material is expected to be insulating we fabricated metal-insulator-metal structures rather than true rectifiers.

3.2.2 Experiment

The bulk AlN was ~200μm thick and was grown by the sublimation method. E-beam deposited full-area back contacts of Ti/Al/Pt/Au were placed on the N-face, while front-side contacts were e-beam deposited Pt/Au with diameters 125-600μm. No edge termination methods were employed around the periphery of the front-side contacts. The current-voltage characteristics were recorded at 25°C using a high-voltage power supply and sensitive ammeter.

3.2.3 Result and Discussion

Figure 1 shows an optical micrograph (top) and plan view transmission electron micrograph (bottom) from the as-grown AlN. A network of crystalline defects and cracks were visible in the material. The defect density was ~10^7cm^{-2}, as measured by TEM.

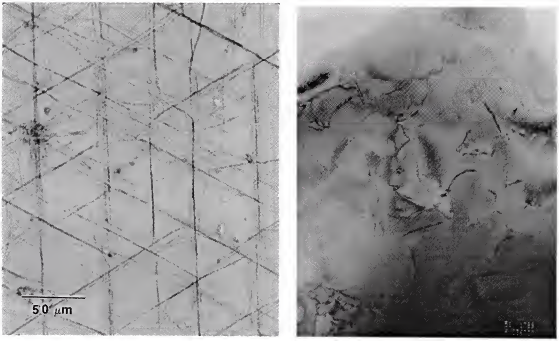

Figure 3-7. Optical micrograph of AlN surface (top) and plan view TEM (bottom).

The low bias current-voltage (I-V) characteristics measured on 225µm diameter contact samples are shown in Figure 3-8. In this region the resistance is ~$2\times10^{10}\Omega$, corresponding to a resistivity of ~$10^{14}\Omega$cm assuming the sample is fully depleted. This confirms the insulator nature of the AlN, negating the possibility of passing current through the material in the forward-bias direction.

Figure 3-9 shows reverse I-V characteristics from samples with two different contact diameters. Note the very high breakdown voltage. We can estimate the critical electric field for breakdown, E_C, from the relationship

$$V_{PT} = E_C W_P - \frac{qNW_P^2}{2\varepsilon_S}$$

where W_P is the stand-off region thickness (assumed to be 200µm), N the doping concentration (assumed to be $<10^6$cm^{-3} for an insulator) and ε_S is the AlN permittivity.

From this relation, we obtain $E_C \sim 3.3\times10^5$ V/cm. This is clearly dominated by breakdown at internal surfaces and therefore the effective stand-off region thickness is much less than the sample thickness and the intrinsic E_C of AlN is much larger than the value found in our samples.

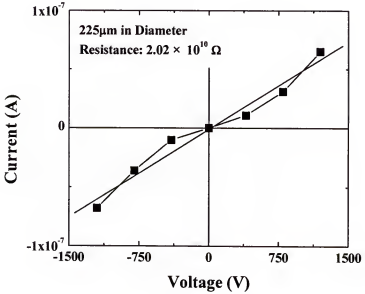

Figure 3-8. I-V characteristics at low bias.

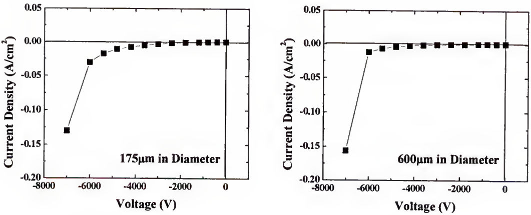

Figure 3-9. Reverse I-V characteristics from samples with different front-side contact diameters.

Figure 3-10 shows the I-V characteristics in both the forward and reverse directions. As expected there is no rectification and the sample behaves as back-to-back diodes. Figure 3-11 shows the reverse breakdown voltage (defined as the voltage for a current density of 0.01A/cm^2) as a function of contact area. The breakdown voltage actually increases with contact size before decreasing at the largest size investigated here. This is a promising sign for future AlGaN bulk rectifiers with low carrier density. The currently available GaN bulk rectifiers have relatively high background carrier concentrations and defect densities, leading to low breakdown voltages(108).

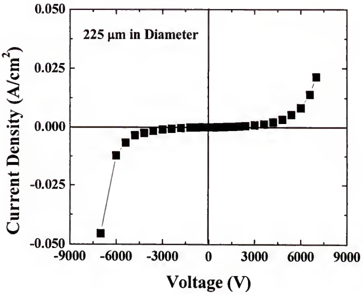

Figure 3-10. I-V characteristics from sample with 225µm diameter front contact.

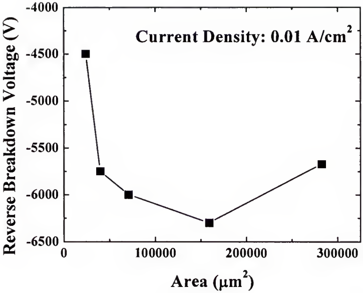

Figure 3-11. Reverse breakdown voltage as a function of front-side contact area.

Finally, Figure 3-12 shows the reverse current density at 4200V as a function of both contact diameter (top) and area (bottom). Since the current is not proportional to either the contact perimeter (surface currents) or the area (bulk current), we confirm the breakdown is dominated by the internal surfaces in the material.

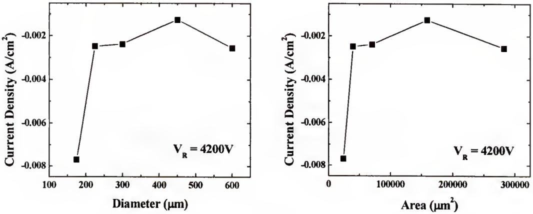

Figure 3-12. Reverse current density at 4200V as a function of either front-side contact diameter (top) or area (bottom).

In summary M-I-M structures fabricated on bulk AlN show the excellent potential of the Al(Ga)N system for power rectifiers.

3.3 HVPE-GROWN AlGaN/GaN HEMTs

High quality undoped AlGaN/GaN high electron mobility transistors(HEMTs) structures have been grown by Hydride Vapor Phase Epitaxy (HVPE). The morphology of the films grown on Al_2O_3 substrates is excellent with root-mean-square roughness of ~0.2nm over $10\times10\mu m^2$ measurement area. Capacitance-voltage measurements show formation of dense sheet of charge at the AlGaN/GaN interface. HEMTs with 1μm gate length fabricated on these structures show transconductances in excess of 110 mS/mm and drain-source current above 0.6A/mm. Gate lag measurements show similar current collapse characteristics to HEMTs fabricated in MBE- or MOCVD grown material.

3.3.1 Introduction

Hydride Vapor Phase Epitaxy (HVPE) was one of the first growth methods employed for GaN(109) and has been successfully used for growth of thick, high-purity quasi-bulk substrates(110-125). The Ga is usually transported to the growth surface as a volatile chlorine compound, while NH_3 is used as the N-precursor. The use of carbon-free precursors is a major advantage relative to other chemical vapor deposition techniques, although at the stage it has still proven challenging to grow insulating GaN by HVPE. It is generally considered that O and Si are not responsible for the after-observed n-type conductivity, but that nitrogen vacancies may play a dominant role(112). This suggests that careful control of the growth process should produce high purity device-quality GaN.

In this paper we report on the characteristics of AlGaN/GaN high electron mobility transistors(HEMTs) grown by HVPE on sapphire substrates.

3.3.2 Experiment

The HEMT structure consisted of a 2μm undoped GaN layer grown on sapphire, followed by 30nm of $Al_{0.22}Ga_{0.78}N$. All of the layers were grown by HVPE at 650°C, as described previously(121). The HEMTs were fabricated by a 4 step process consisting of dry etch mesa isolation, ohmic metallization, ohmic anneal and gate metallization as described in detail previously(131). In brief, the mesa that was performed by Cl_2/Ar Inductively Coupled Plasma etching at 1mTorr with 300W of 2MHz source power and 40W of rf(13.56MHz) chuck power. Ohmic metallization of Ti/Al/Pt/Au was deposited by e-beam evaporation and patterned by lift-off. A low specific contact resistance of 10^{-6} $\Omega\text{-cm}^2$ was achieved after 850°C, 30sec annealing. Gate contacts ($1\times100\mu m^2$) of Ni/Au were patterned by lift-off. A schematic of the completed device is shown in Figure 3-13. The dc characteristics were measured in common-source mode with an HP 4145B parameter analyzer.

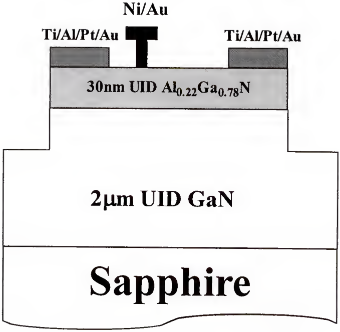

Figure 3-13. Schematic of Completed HEMT.

3.3.3 Results and Discussion

Figure 3-14 shows Atomic Force Microscope (AFM) scan from various areas of an as-grown HEMT structure. The typical best root-mean-square (RMS) roughness measured over a $10\times10\mu m^2$ area was ~0.22nm as shown in the scan at right whereas the roughest area was still < 1nm, as shown in the scan at left. There is a clear demonstration that HVPE is capable of growing high quality ALGaN/GaN heterostructures with excellent surface morphology, which is a necessary condition for achieving sharp heterointerfaces.

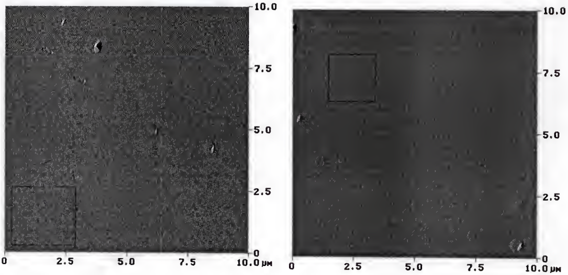

rms = 0.713nm, box rms = 0.647nm

rms = 0.251nm, box rms = 0.226nm

Figure 3-14. AFM scans from 30nm $Al_{0.22}Ga_{0.78}N$ / 2μm undoped GaN grown by HVPE in sapphire.

To give an example of the ability of HVPE to form a HEMT structure, Figure 3-15 shows a typical result of capacitance-voltage (C-V) measurements performed on-wafer on large-area contact pads. The data is shown in C^{-2} vs V form at top and the resulting carrier concentration as a function of voltage at bottom. There is a clear indication of the presence of a dense sheet of charge at the AlGaN/GaN heterointerface.

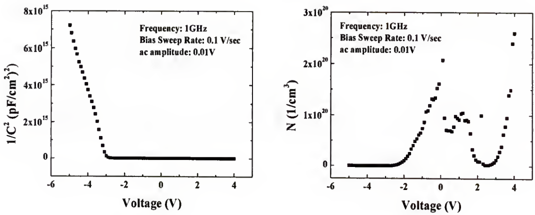

Figure 3-15. C^{-2} vs V and resultant N vs V for HVPE-grown $Al_{0.22}Ga_{0.78}N/GaN$ HEMT structure.

The carrier concentration measured by Hg-probe C-V measurements at 10KHz on an as-grown calibration sample is shown in Figure 3-16. Once again, this data shows a sheet of carriers at the AlGaN/GaN heterointerface which we ascribe to a polarization-induced two dimensional electron gas, just as is observed in NBE or MOCVD grown structures^(126).

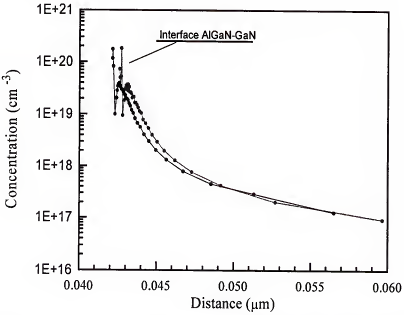

Figure 3-16. N_D-N_A concentration profile measured by Hg probe at 10KHz for $Al_{0.22}Ga_{0.78}N/GaN$ HEMT structure at different parts on the wafer.

The maximum drain current density was > 0.6A/mm before self-heating effects caused a decrease in the output current. Characteristics drain I-V characteristics are shown at the top of Figure 3-17. The devices showed excellent pinch-off behavior, with maximum transcondcutance > 100mS/mm as seen in the transfer characteristics at the bottom of the figure. From a limited set of data, we found that the peak of the extrinsic transconductance curve shifted forwards more positive gate voltage with increasing gate length and the magnitude of g_m scaled with increase gate length. The performance of the HVPE grown HEMTs in clearly very promising when compared with MBE or MOCVD HEMTs with similar gate lengths.

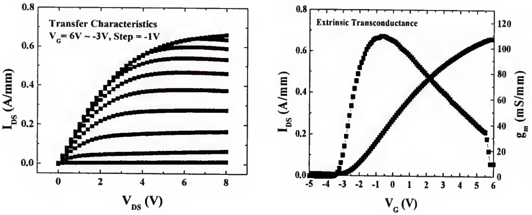

Figure 3-17. Drain I-V characteristics (top) and transfer characteristics (bottom) from HVPE-grown, 1×100μm^2 HEMT.

Gate I-V characteristics are shown in Figure 3-18. Further optimization of the layer structure and growth conditions is expected to produce larger reverse breakdown voltages and these initial layer designs were not focused in power applications. Our experience with the HVPE growth is that there is a relatively broad range of conditions that produce device-quality material.

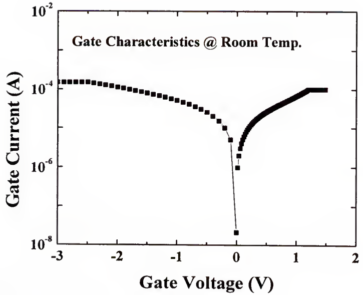

Figure 3-18. Gate I-V characteristics from 1×100μm^2 HVPE-grown HEMT.

One of the existing problems with AlGaN/GaN HEMT technology is the so-called "current-collapse" phenomenon that causes at high drive current. This is caused in most cases by intrinsic surface traps in the gate-drain region that can create an additional depletion region which pinches off the current flow(76). Figure 3-19 shows a 40-50% decrease in drain-source current during pulsing of the gate terminal with the drain biased at a fixed dc voltage. These results are consistent with results reported for MBE and MOCVD AlGaN/GaN HEMTs, indicating that the HVPE material has similar surface properties(132). The current collapse problem can be effectively mitigated by use of high quality passivating dielectrics and oxides(132-134).

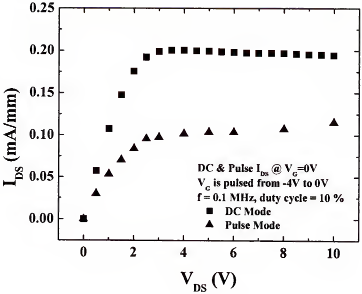

Figure 3-19. Gate lag measurements on unpassivated HVPE-grown HEMT.

The HVPE technique is shown to be a very promising approach for growth of AlGaN/GaN HEMT structures. The surface morphology is excellent after growth of layers with total thicknesses similar those employed in MBE and MOCVD growth. Electrical measurements show formation of an abrupt sheet of charge at the heterointerface. HEMTs fabricated with a standard processing sequence display excellent dc characteristics and indicate that HVPE is an attractive, high throughput, low cost approach to growth of nitride-based devices.

CHAPTER 4
PLASMA DAMAGE EFFECTS ON III-V COMPOUND SEMICONDUCTOR DEVICES

4.1 Comparison of the Effects of H_2 AND D_2 Plasma Exposure on AlGaAs/GaAs HEMTs

The dc and rf performance of AlGaAs/GaAs High Electron Mobility Transistors were measured after exposure to low pressure (5 mtorr) Inductively Coupled Plasmas of H_2 or D_2 for various source (100-400W) and chuck powers (10-100W) and durations (1-4 min). The plasma exposure decreases drain-source current, increases gate leakage and increases the gate ideality factor, even at very low plasma powers and for short process durations. A number of physical and chemical effects are found to be responsible for the observed behavior, including preferential loss of As from the surface, creation of deep trap states by energetic ion bombardment and passivation of Si donors by formation of Si-H or Si-D neutral complexes.

4.1.1 Introduction

AlGaAs/GaAs HEMTs are an integral part of many monolithic microwave integrated circuits used in wireless communication devices such as hand- held phones. Plasma processing is a key to the ability to manufacture HEMTs with high yield. A key etching step is selective removal of the GaAs cap layer to expose the AlGaAs donor layer for deposition of the gate metal(135). This can be achieved with very high selectivities using low power plasmas involving a mixture of Cl_2 and F_2 gases. End-point detection is possible using optical emission spectroscopy that monitors Ga-related emission lines. It is also necessary to provide final passivation of the HEMT surface, which is typically achieved by low power plasma-enhanced chemical vapor deposition (PECVD) of SiN_X. The gaseous precursors in this case are SiH_4/N_2 or SiH_4/NH_3. It is important to understand the effect of the hydrogen in these plasmas on the dc and rf performance of the completed HEMTs. For example, there are at least three possible effects that the hydrogen could have:

(i) creation of deep trap states by the impingement of energetic H_2^+ or H^+ ions on the semiconductor surface. The displacement energy of the atoms in compound semiconductors is roughly 25eV, while the average energy of the incident ions may be three or four times higher(136-171).

(ii) preferential loss of As from the surface by chemical reaction with atomic hydrogen, i.e.

$$GaAs + 3H \rightarrow AsH_3 + Ga \qquad (4\text{-}1)$$

(iii) passivation of Si donors in the AlGaAs through formation of neutral donor-hydrogen complexes, i.e.

$$Si^+ + H^- \rightarrow (Si\text{-}H)^o \qquad (4\text{-}2)$$

where the atomic hydrogen is in a negative charge state in n-type material(171).

In this paper, we compare the effects of low power Inductively Coupled Plasmas of H_2 and D_2 on the dc and rf performance of 0.25μm gate length unpassivated AlGaAs/GaAs HEMTs(144, 135, 172, 173). Even plasma exposures at low ion energies and fluxes can degrade the device performance. It should be noted we are in a worst-case scenario because there is no actual SiN_X deposition occurring that would cover up the semiconductor surface and prevent further hydrogen-induced degradation.

4.1.2 Experimental

The HEMTs were grown on semi-insulating GaAs substrate by solid-source Molecular Beam Epitaxy. After growth of a 1μm thick undoped superlattice buffer, the structure consisted of 0.5μm undoped GaAs, 300Å n^+-$Al_{0.25}Ga_{0.75}As$ and 410 Å of n^+-GaAs. Conventional optical lithography was used to pattern Ti/Pt/Au gate metal and Au/Ge/Ni/Au ohmic metal. The gate recess was formed by selective wet etching in order to avoid possible dry etch damage effects. The devices were exposed to H_2 or D_2 ICP discharges for 1-4 minutes at various rf chuck powers (10-100W at 13.56MHz) and source powers (100-400W at 2MHz). Testing was performed with an HP 4145A parameter analyzer for dc measurements and an HP 8722C high frequency network system.

4.1.3 Results and Discussion

(a)dc performance

Figure 4-1 shows typical drain-source current-voltage (I-V) characteristics before and after a 1 min exposure of the HEMTs to either a H_2 (left) or D_2 (right) plasma. Note that in both cases there is suppression of the drain-source current, with the reduction being greater in the case of D_2 plasmas. These results are consistent with a reduction in carrier concentration in the device channel, either through dopant passivation or creation of deep trap states by ion bombardment.

This reduction in carrier concentration is also reflected in a general increase in reverse breakdown voltage of the HEMTs, shown in Figure 4-2 for both H_2 (left) and D_2 (right) plasma exposure. In this data, we have held the rf chuck power constant at 10W while varying the source power, and also held the source power constant at 100W while varying the rf chuck power. Depending on the plasma, there may be a decrease in breakdown voltage at either the highest source or chuck power. This may result from surface-induced breakdown due to the creation of damaged or As-deficient near-surfaces.

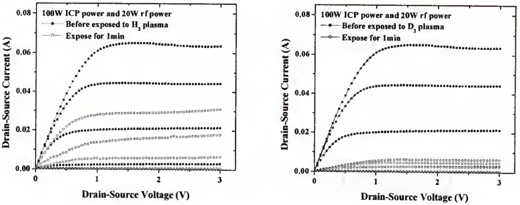

Figure 4-1. I_{DS}-V_{DS} characteristics before and after exposure to H_2 (left) or D_2 (right) plasmas for 1 min at 100W source power and 20W rf chuck power.

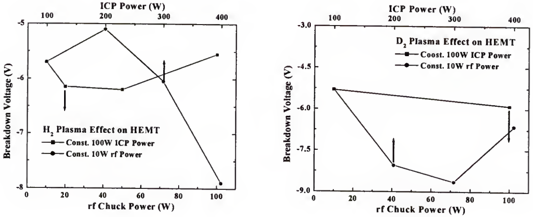

Figure 4-2. Variation of reverse breakdown voltage with both ICP source power and rf chuck power during H_2 (left) or D_2 (right) plasma exposures for 1min.

The plasma exposures also produce an increase in low bias gate current, as shown in the forward I-V characteristics of Figure 4-3 for H_2 plasmas at different rf chuck powers (left) and D_2 plasmas at different source powers (right). These results show that both ion energy and ion flux play a role in the change in I-V characteristics, since the power is mainly controlled by the rf chuck power and the latter is mainly a function of source power. The increased gate leakage could be a result of creation of defect states around the periphery of the gate contact. These defect states would need to be recombination centers, i.e. have a comparable capture cross-section for both electrons and holes. We rule out a change in barrier height for the gate contact as the reason for the increased gate leakage because the metal-semiconductor interface is protected by the thick metal stack.

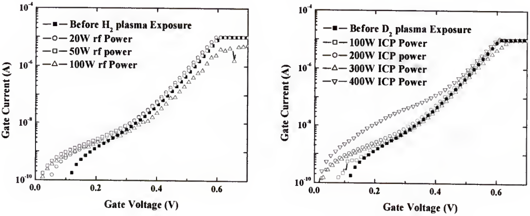

Figure 4-3. I_G-V_G characteristics before and after H_2 (left) or D_2 (right) plasma exposures for 1 min at different chuck or source powers.

There was a significant difference between H_2 and D_2 plasmas in terms of their effect on excess gate leakage induced as a function of plasma exposure time. As shown in Figure 4-4 (left), this leakage tended to saturate with H_2 plasma exposure time, whereas the low-bias current continued to increase with D_2 plasma exposure time (right). This may be a result of the heavier D_2^+ and D^+ ions inducing more recombination centers around the gate periphery. Note that there is no significant change in the I-V characteristics beyond a bias voltage of ~0.5V, indicating the recombination centers are saturated by the higher current flow at these biases.

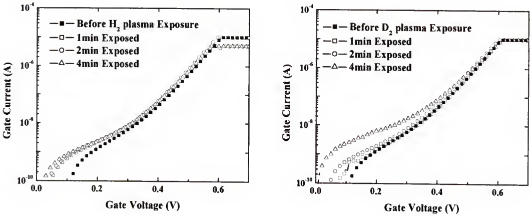

Figure 4-4. I_G-V_G characteristics before and after H_2 (left) or D_2 (right) plasma exposure for different times.

The I-V characteristics were fit to the relationship

$$I=A.A^{*}T^{2}\exp(-e\phi/kT)\exp(eV/nkT-1) \qquad (4\text{-}3)$$

where A is the contact area, A^* is Richardson's constant, e is the electronic charge, ϕ is the gate contact Schottky barrier height, n is the ideality factor, k is the Boltzmann's constant, V is the applied bias and T is the absolute device temperature. From this data, we could extract the ideality factors. Figure 4-5 (left) shows the effect of both rf chuck power and source power on n values from HEMTs exposed to H_2 plasmas. The ideality factor initially worsens as both the source or chuck power is increased, but is less decreased at either high source or chuck power. In the former case this may result from the reduced ion energy as the increased ion density suppresses the dc self-bias on the sample electrode. In the case of increasing rf chuck power at fixed source power, the damage around the gate periphery may become severe enough to induce a tunneling contribution in the I-V characteristics. In the case of D_2 plasmas (shown in Figure 4-5, right), once again the ideality factor worsens initially as source power is increased but decreases above 300W due to the reduction in the average incident ion energy. As the rf chuck power is increased, there is a monotonic increase in ideality factor. The turn-over observed with H_2 plasma exposure may occur at higher rf chuck powers for D_2 plasma exposure.

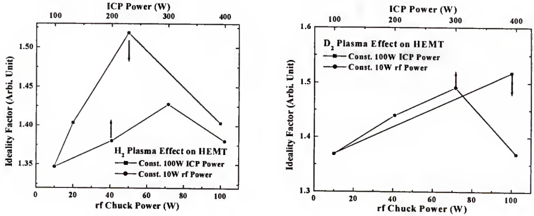

Figure 4-5. Ideality factor as a function of rf chuck or source power during H_2 (left) or D_2 (right) plasma exposures.

The sheet resistance of the conducting AlGaAs donor layer may be expressed as

$$\rho_S = e \times \mu \times n_S \tag{4-4}$$

where e is the electronic charge, μ the electron mobility and n_S the sheet electron density. Figure 4-6 (left and right) shows a similar behavior of H_2 and D_2 plasma exposed structures in terms of the response of sheet resistance to increasing source power at constant rf chuck power. The sheet resistance increases with increasing source power up to 300W and basically saturates thereafter. The increase in resistance can primarily be based to a reduction in sheet carrier density through the introduction of deep electron traps. However, as source power continues to be increased, the associated ion energy decreases and the damage saturates because the product of ion energy and ion flux remains roughly constant.

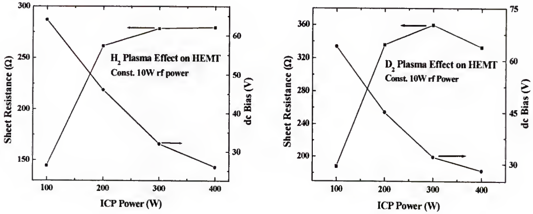

Figure 4-6. Channel sheet resistance as a function of ICP source power during H_2 (left) or D_2 (right) plasma exposures.

The strong influence of ion energy and constant ion flux is obvious from the data of Figure 4-7 (left and right). In the case of H_2 plasma exposure, there is only a slight indication of damage saturation as evidenced by the increase in sheet resistance, whereas the effect is more pronounced with the heavier D_2^+ and D^+ ions in the deuterium plasma. The number of point defects created by energetic ion bombardment, N_d, can be expressed approximately by the Kinchin-Pease formula

$$N_d = \frac{E_n}{2E_d} \qquad (4\text{-}5)$$

where E_n is the energy deposited into nuclear stopping and E_d is the atomic displacement energy (roughly 20-25eV in semiconductors). This formula usually overestimates the number of point defects because it does not take into account the dynamic annealing of damage through point defect recombination. This recombination effect would be more prevalent for D_2 plasma exposure and may explain the saturation of sheet resistance being obvious at lower rf chuck powers than for H_2 plasma exposure.

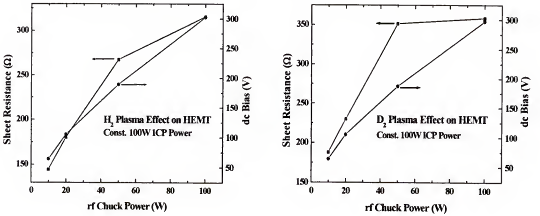

Figure 4-7. Channel sheet resistance as a function of rf chuck power during H_2 (left) or D_2 (right) exposures.

The damage induced in the HEMTs also tended to saturate with exposure time to both types of plasma, as shown in Figure 4-8 (left and right). The self-bias exhibited a slight upward drift with time for D_2 plasmas and the opposite trend for H_2 plasmas. The saturation effect of damage with exposure time may also be explained by recombination of point defects leading to an equilibrium situation.

The effects of both ICP source power and rf chuck power on HEMT threshold voltage (V_T) are shown in Figure 4-9 (left and right) for both H_2 and D_2 plasma exposure. The V_T values initially decrease as these powers are increased, corresponding to a lower effective carrier concentration in the channel as deep trap states are created. As the source power is increased above 200-300W, the corresponding decrease in ion energy leads to a reduced change in V_T. Once again, there is a noticeable difference in behavior between H_2 and D_2 plasma in terms of the effect in V_T at higher rf chuck powers, perhaps related to the role of ion mass in defect creation.

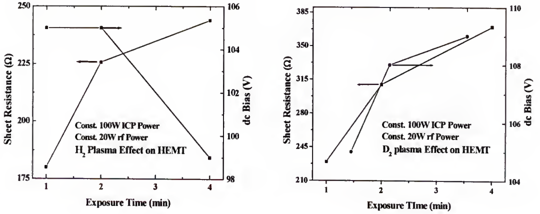

Figure 4-8. Channel sheet resistance as a function of exposure time to either H_2 (left) or D_2 (right) plasmas at fixed source (100W) and rf chuck power (20W).

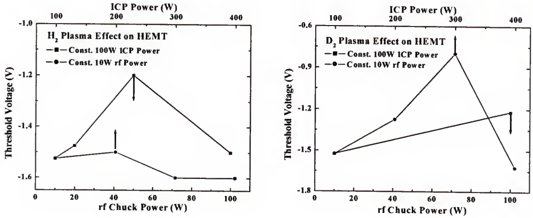

Figure 4-9. V_T a function of rf chuck or source power during either H_2 (left) or D_2 (right) plasma exposures.

The extrinsic transconductance (g_m) is a key device parameter for field effect transistors and was found to be strongly degraded by increasing rf chuck power or source power in both H_2 and D_2 plasmas, as shown in Figure 4-10 (left and right). In the case of

D_2 plasmas, the g_m essentially goes to zero at a moderate source power (300W) and is slightly less degraded at higher powers due to the lower ion energy. The degradation in g_m is slightly less pronounced for H_2 plasma exposure, which again is likely related to the smaller defect density created by the lighter ions. Note that both ion flux and ion energy have very strong influences on the HEMT g_m. To have minimal decrease in g_m, it is necessary to keep both of these parameters at their minimum values to sustain the plasma (i.e. roughly 100W source power and 10W rf chuck power). In a real deposition process, these requirements would not be quite as stringent due to the protective dielectric layer formed on the HEMT surface.

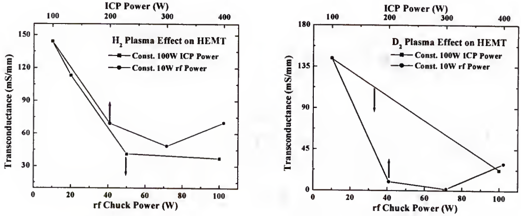

Figure 4-10. g_m as a function of rf chuck or source power during either H_2 (left) or D_2 (right) plasma exposures.

(b) rf performance

Figure 4-11 shows the effect of rf chuck power on the values of both f_T and f_{Max} at constant source power of 100W for both H_2 and D_2 plasmas. Both parameters fall-off rapidly with increasing ion energy during the plasma exposure. The average ion energy is given by the sum of dc self-bias and plasma potential with the latter being roughly -

25V in this system. There is slightly less degradation in f_T and f_{Max} for rf chuck powers of 100W in H_2 plasmas, but the values for both parameters remain well below their starting points of ~30GHz.

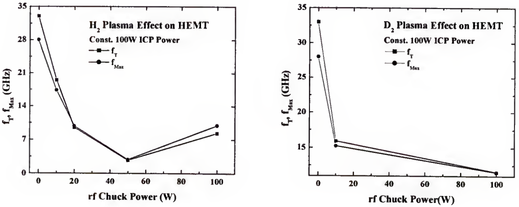

Figure 4-11. f_T and f_{MAX} as a function of rf chuck power during either H_2 (left) or D_2 (right) plasma exposure at fixed source power (100W).

Similar behavior was found for the effect of ICP source power on the microwave performance, as shown in Figure 4-12 (left and right) for increasing source power at a fixed rf chuck power of 10W. Note that for source powers in excess of ~100W, the f_T and f_{Max} values are severely degraded. As pointed out earlier, this fall-off would be somewhat less in a real deposition process. In the case of D_2 plasmas, the degradation in microwave parameters is less at higher source power due to the decrease in ion energy.

The HEMT can be viewed as a system of resistances and capacitances that will determine the final rf performance. Figure 4-13 (left) shows a cross-sectional view of the HEMT structure and the various source, drain and gate resistances and the capacitances between them. A simplified equivalent circuit for the HEMT is shown at the right of Figure 4-13. We were able to determine the numerical values for all these parameters by fitting the rf data and then to measure the variation of these values with the different plasma exposure conditions.

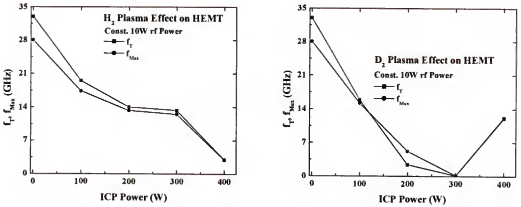

Figure 4-12. f_T and f_{MAX} as a function of source power during either H_2 (left) or D_2 (right) plasma exposure at fixed of chuck power (10W).

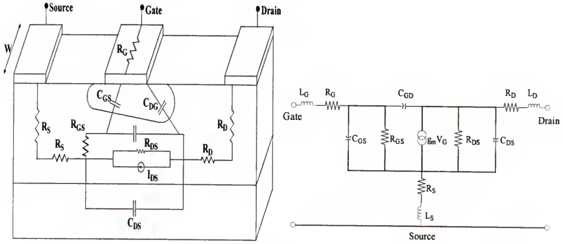

Figure 4-13. Schematic cross section of HEMT (left) showing origin of resistances and capacitances, and equivalent circuit diagram (right).

Figure 4-14 shows the effect of both rf chuck power and source power on the intrinsic transconductance. Both parameters lead to strong degradation of the transconductance as they are increased and even a low rf chuck power of 10W is sufficient to cause major suppressions of transconductance if source powers above 100W were employed. Since the transconductance is essentially related to gain, then clearly the utility of the device is lost if this parameter is degraded.

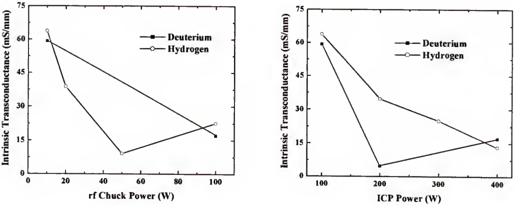

Figure 4-14. Intrinsic transconductance as a function of rf chuck (left) and source power (right) for H_2 and D_2 plasma exposures.

The effect of increasing rf chuck power in drain-source resistance (R_{DS}) and capacitance (C_{DS}) at fixed source power as shown in Figure 4-15 (left and right), respectively. The R_{DS} values increase in chuck power is increased due to the reduction in channel doping as trap states are introduced, while C_{DS} shows a more complex behavior but much smaller relative changes (of the order of 25% of the initial value, compared to 200-450% damages in R_{DS}).

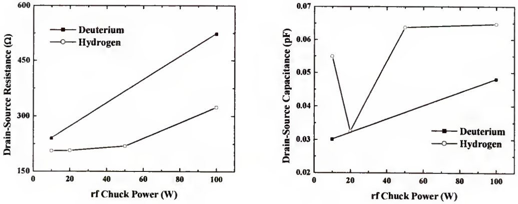

Figure 4-15. R_{DS} (left) and C_{DS} (right) as a function of rf chuck power for both H_2 and D_2 plasma exposure.

The drain resistance, R_D, comprises contribution from the heavily doped GaAs under the drain contact as well as the transition region to the channel. This parameter is clearly a function of the effective doping in these regions, which can be decreased through hydrogen passivation of the Si donors and creation of traps both in the epilayer and around the periphery of the drain contact area. Figure 4-16 (left and right) shows the effect of H_2 and D_2 plasma exposure on R_D as a function of increasing rf chuck power. The effect of H_2 is such greater, which may indicate hydrogen passivation of the drain dopants as a major contributor because the diffusivity of atomic hydrogen is $\sqrt{2}$ times larger than that of atomic deuterium because of the isotope effect.

Figure 4-17 shows the influence of rf chuck power (left) and source (right) on the gate-source resistance (R_{GS}) for both H_2 and D_2 plasma exposure. Once again, the H_2 plasmas are found to have a generally larger effect than D_2, which may be a result of the more efficient passivation. This is supported by the fact that H_2 plasmas lead to a very large change in R_{GS} at high source power (400W), where the ion energy is low (<30eV) and therefore point defect creation is quite inefficient.

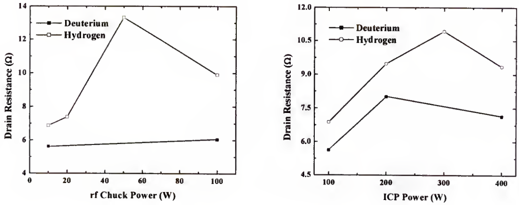

Figure 4-16. R_D as a function of rf chuck power (left) or source power (right) for both H_2 and D_2 plasma exposures.

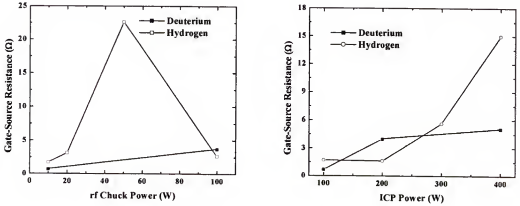

Figure 4-17. R_{GS} as a function of rf chuck power (left) or source power (right) for bother H_2 and D_2 plasma exposure.

Similar data is shown in Figure 4-18 (left and right) for gate-source capacitance (C_{GS}) as a function of both rf chuck power and source power. There is a general trend of decreasing C_{GS} as both of these parameters increase for both D_2 and H_2 plasma exposure, due to reduction in effective doping level between the gate and source regions. The only exception is for H_2 plasmas at the highest source powers where there may be situation in which low energy ion production is relatively efficient, reducing the density of atomic hydrogen neutrals available for passivation.

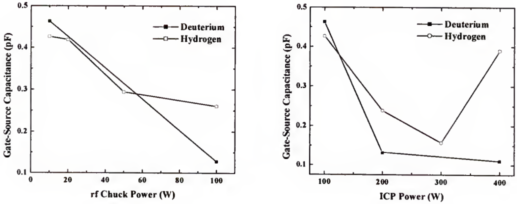

Figure 4-18. C_{GS} as a function of rf chuck power (left) as a source power (right) for both H_2 and D_2 plasma exposure.

The gate-to-drain capacitance (C_{GD}) was also extracted from the rf measurement data. This value is shown in Figure 4-19 (left and right) as a function of rf chuck power and ICP source power for both H_2 and D_2 plasma exposure. There is a general trend of increasing C_{GD} as source power increases for both H_2 and D_2, whereas the influence of rf chuck power is more complex and probably involves the net effect of creating donor-like surface states through preferential loss As and the loss of donors in the gate-to-drain region due to creation of deep traps and hydrogen passivation.

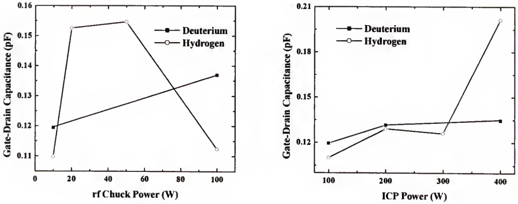

Figure 4-19. C_{GD} as a function of rf chuck power (left) or source power (right) for both H_2 and D_2 plasma exposures.

Finally, Figure 4-20 shows the change of source resistance, R_S, with ICP source power in both H_2 and D_2 plasmas. The R_S values lead to decrease in H_2 plasmas but go through a maximum with D_2 plasma exposure. This behavior is opposite to that of the drain resistance and needs more work in order to clarify the origin of the differences.

AlGaAs/GaAs HEMTs with 0.25µm gate length were exposed to low power H_2 or D_2 plasmas to simulate a worst-case scenario during deposition of dielectric passivation films. Both the dc and rf performance were strongly degraded by high ion energies or fluxes during the plasma exposure. Each of the critical device parameters was measured as a function of the source and rf chuck power during plasma exposure and all of them were sensitive to the plasma parameters. The strategy during deposition of dielectrics onto HEMTs using H_2-containing precursor gases is clearly to have a rapid initial deposition rate in order to cover the surface as quickly as possible to prevent changes through preferential loss of As, hydrogen passivation of dopants or creation of deep trap states by energetic ion bombardment.

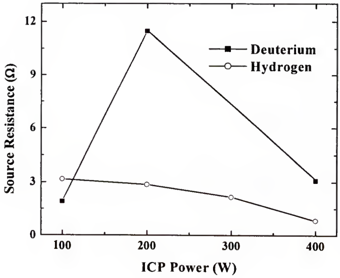

Figure 4-20. Source resistance as a function of ICP source power for both H_2 and D_2 plasma exposure.

4.2 Hydorgenation Effects on AlGaAs/GaAs Heterojunction Bipolar Transistors

A comparison of the effects of H_2 and D_2 plasmas on the dc characteristics of AlGaAs/GaAs heterojunction bipolar transistors showed a strong influence of exposure time, ion flux and ion energy on the forward and reverse junction current-voltage (I-V) characteristics, base resistance and E-B (E-B) breakdown voltage and ideality factor. The results are quite different than those observed with N_2 or Ar plasma exposure of similar devices and show that passivation of the carbon acceptors in the base layer is a major problem with processes such as PECVD of SiN_X or SiO_2 sidewall space layers during HBT fabrication.

4.2.1 Introduction

AlGaAs/GaAs heterojunction bipolar transistors (HBTs) are rapidly gaining marked share For use in wireless and lightwave communication systems because of their improved linearity relative to GaAs metal-semiconductor field effect transistor(174-182). As the device dimensions decrease, processing steps such as formation of sidewall spacers on the emitter/base mesa become increasingly necessary. These spacers are typically deposited by plasma enhanced chemical vapor deposition (PECVD) of SiN_X or SiO_2 from SiH_4/NH_3, SiH_4/N_2 or SiH_4/N_2O chemistries(142-162). The high concentration of atomic hydrogen present during this process might be expected to produce passivation of the Si and C dopants used in the emitter and base layers, respectively. Previous work has shown that ion bombardment occurring during N_2 or Ar plasma can have a significant effect on HBT dc performance through introduction of deep trapping states in both the both and on the surface of the component layers within the device(144, 158, 165-172). There is also inherent in the relative effects of hydrogen versus deuterium, because the heavier mass of the ^2H would decrease the damage depth for ion-bombardment effects. Typically-substituted precursors for PECVD are widely available and this could be are approach for reducing the effects of hydrogenation during plasma processing of HBTs. In addition the diffusion coefficient of ^2H is ~40% slower than that of ^1H, according to the relation

$$\frac{D_H}{D_D} \propto \frac{M_D}{M_H} \tag{4-6}$$

where D is the diffusivity and M is the atomic mass of the hydrogen (H) or deuterium (D), respectively.

In this paper, we report on the effect of ^1H and ^2H plasma exposure on the dc characteristics of large area AlGaAs/GaAs HBTs with aggressive doping and layer thickness design. These HBT layer structures are typical of those needed for high bit-rate lightwave communication systems.

4.2.2 Experiment

The layer structures were grown by Metal Organic Molecular Beam Epitaxy on undoped, semi-insulating GaAs(100) substrates$^{(183)}$. The n^+-GaAs ($n = 3\times10^{18}cm^{-3}$) sub-collector (0.6 μm thick) was followed by an n-GaAs ($n = 2\times10^{16}cm^{-3}$) collector (0.4 μm thick), p^+-GaAs ($p = 7\times10^{19}cm^{-3}$) base (0.07 μm thick), n^+-$Al_{0.3}Ga_{0.7}As$ ($n = 8\times10^{18}cm^{-3}$) emitter (0.08 μm thick) and a 0.02 μm grade to a n^+-GaAs ($n = 1.5\times10^{19}cm^{-3}$) emitter contact layer (0.2 μm thick). HBTs with emitter dimensioins ~90 μm were fabricated by wet chemical etching. Lift-off of e-beam deposited Au/Ge/Ni and Ti/Pt/Au was employed for ohmic contacts to the emitter/collector and base layers, respectively. A scanning electron micrograph of some of the completed devices is shown in Figure 4-21.

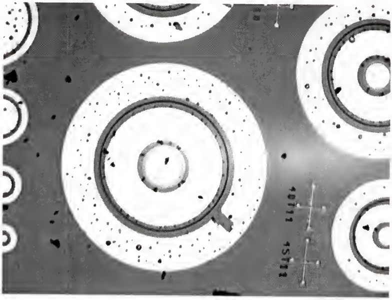

Figure 4-21. SEM micrograph of completed devices

The HBTs were exposed to H_2 or D_2 plasmas in a Plasma Therm 790 system. The inductively coupled plasma source operates at 2MHz, while the sample chuck was biased with 13.56MHz power. The source power basically contacts the ion flux and degree of plasma dissociation, while the rf chuck power controls the ion energy. This average ion energy is approximately the sum of the dc self-bias and the plasma potential. The latter is ~20eV in this particular tool under the experimental conditions we used. The device dc characteristics were measured on an HP 4145A parameter analyzer at room temperature.

4.2.3 Results and Discussion

Figure 4-22 shows the reverse I-V characteristics from the E-B functions of HBTs exposed to either H_2 (left) or D_2 (right) plasmas as a function ICP source power at fixed rf chuck power and process pressure (5 mTorr). The reverse breakdown voltage (V_B) of control devices was approximately –1.2V. Note that there is a major increase in V_B in all cases, but ^1H is significantly worse than ^2H under the same conditions. The degradation in V_B is also worse at high source powers for both types of discharge, where the ion energy is low and the ion flux is high. The results indicate that the doping on both sides of the junction is being decreased, probably through a combination of dopant passivation by the reactions

$$Si^+ + H^- \rightarrow (SiH)^0 \tag{4-7}$$

$$C^- + H^+ \rightarrow (CH)^0 \tag{4-8}$$

And by deep trap formation that removes electron from the emitter and holes form the base. Ion damage in GaAs and AlGaAs is known to move the Fermi level towards midgap in both n- and p-type material.

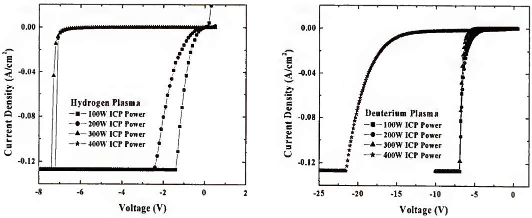

Figure 4-22. Reverse E-B junction characteristics as a function of source power during hydrogen (left) or deuterium (right) plasma exposure.

The forward I-V characteristics from these devices are shown in Figure 4-23. In the case of hydrogen plasma exposure (left), the E-B junction shows significant low-bias leakage for the lowest source power condition where ion energy is at its highest. This result would indicate that recombination centers are being created around the junction periphery by ion damage and preferential loss of As through the reaction

$$As + 3H \rightarrow AsH_{3(g)} \quad (4\text{-}9)$$

By sharp contrast, the results for ^{2}H plasma exposure show extreme degradation of the E-B junction forward I-V at the highest source power where the ion flux and atomic deuterium concentrations are at their highest values.

The E-B junction reverse I-V characteristics as a function of the rf chuck power for both ^{1}H and ^{2}H plasma exposure are shown in Figure 4-24. The V_B values for ^{1}H plasma treatments increase dramatically as the chuck power and hence ion energy is increased (left). By contrast, the ^{2}H plasma treatments produce an essentially constant amount of increase in V_B (right). These results implicate the ion mass is playing a major role and therefore that ion-induced trap states are one of the major mechanisms in the carrier loss that produces the increase in V_B.

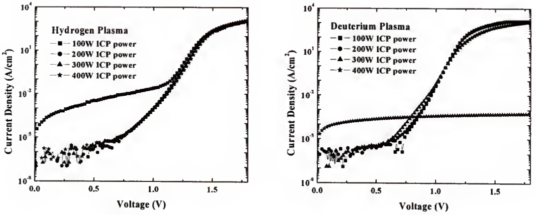

Figure 4-23. Forward E-B junction characteristics as a function of source power during hydrogen (left) or deuterium (right) plasma exposure.

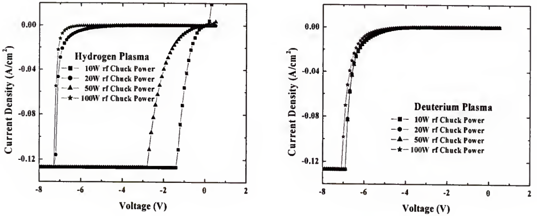

Figure 4-24. Reverse E-B junction characteristics as a function of rf chuck power during hydrogen (left) or deuterium (right) plasma exposure.

The forward I-V characteristics from the E-B junctions of the HBTs exposed to ^{1}H and ^{2}H plasmas as a function of rf chuck power are shown in Figure 4-25. In the case of hydrogen plasma treatments the forward leakage current is increased significantly at low chuck powers where the ion energy is small, suggesting that loss of As at the surface might be the cause of the increase current. In the case of deuterium plasma treatments the low bias leakage is largely ion affected by any of the rf chuck power, but the series resistance is worse at higher powers.

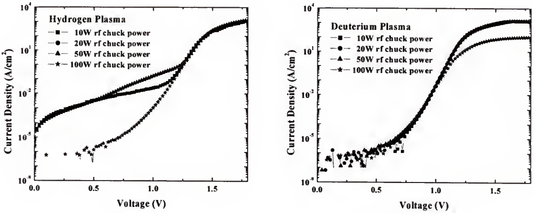

Figure 4-25. Forward E-B junction characteristics as a function of rf chuck power during hydrogen (left) or deuterium (right) plasma exposure.

The effect of exposure time at fixed source power and rf chuck power is shown in Figure 4-26. There is not a large effect of exposure time on the reverse E-B I-V characteristics provided the source power and chuck power are above the threshold for damage. Note that in all cases the V_B increases from –1.2V to approximately –7V, indicating very significant loss of doping.

The forward I-V characteristics of the E-B junctions are shown in Figure 4-27 as a function of plasma exposure time. In the case of hydrogen plasmas (left) there is a slight increase in low-bias leakage with increasing time, whereas for deuterium plasmas (right), the changes are more significant both for low-bias current and the series resistance effect above ~1.2 V. These results indicate that the mass of the incident ions plays a key role in influencing the function electrical characteristics.

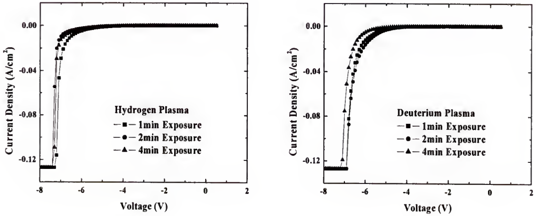

Figure 4-26. Reverse E-B junction characteristics as a function of exposure time to hydrogen (left) or deuterium (right) plasmas.

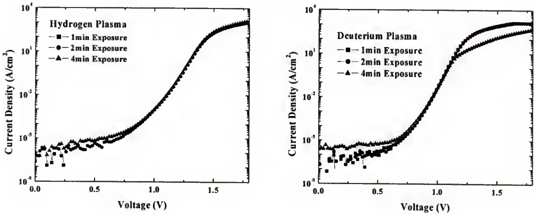

Figure 4-27. Forward E-B junction characteristics as a function of exposure time to hydrogen (left) or deuterium (right) plasmas.

Figure 4-28 shows the Gummel plots from deuterium plasma exposed samples as a function of rf chuck power (left), source power (center) or exposure time (right). There was little change in either collector or collector or base current as a function of chuck power, but both were decreased by increasing source power (or equivalently ion flux and atomic deuterium neutral flux). Similarly, longer exposure times at fixed power were found to decrease both I_C and I_B. This would be expected as damage builds up with longer exposure times.

These results translate into changes in the current gain of the devices, as shown in Figure 4-29. In the case of varying rf chuck power (top) the changes with both hydrogen and deuterium plasmas was negligible. In the case of varying source power (center), the changes in I_B and I_C essentially offset each other and again led to small changes in current gain. However for varying exposure time the changes could be quite large. One also has to remember that the current gain can be dependent on the device operating time when hydrogen is present, because passivated carbon acceptors in the base can be reactivated by carrier (electron) injection. The measured gain, G, then may vary as

$$G(t) = G_0 \times \exp(-{}^{t}\!/_{\tau}) \qquad (4\text{-}10)$$

where G_0 is the gain in unpassivated devices, t is the device operation time and τ is a temperature-dependent deactivation time constant.

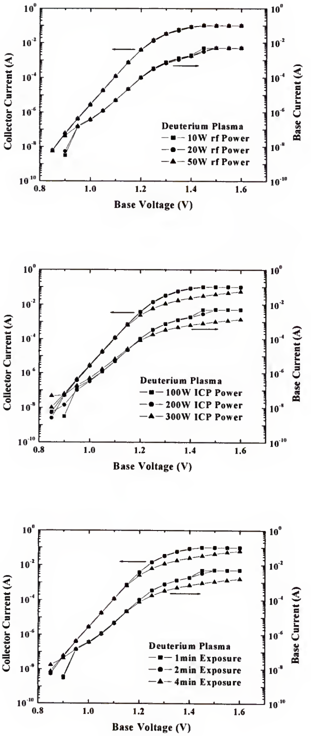

Figure 4-28. Gummel plots before and after deuterium plasma exposure at different rf chuck power (top), source power (center) or exposure times (bottom).

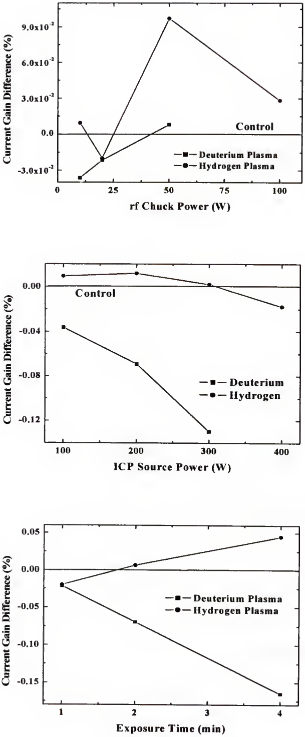

Figure 4-29. Current gain change as a function of rf chuck power (top), source power (center) or exposure time (bottom) for hydrogen and deuterium plasmas.

Figure 4-30 shows the E-B junction ideality factors as a function of source power (top), rf chuck power (center) or exposure time (bottom) for hydrogen plasma treatments, in addition to the E-B junction breakdown voltages. The ideality factors were extracted from the forward I-V characteristics according to the relationship

$$J_F = A^{**}T^2 \exp(\frac{eV}{nK_BT}) \exp\left[-\frac{(E_g - eV)}{K_BT}\right] \tag{4-11}$$

where A^{**} is Richardson's constant, T the absolute measurement temperature, e the electronic charge, K_B is Boltzmann's constant, E_g the material bandgap and J_F is the forward current density. The n values remain between ~1.25 and 1.48 and were more affected by rf chuck power.

Similar results are shows in Figure 4-31 for HBTs exposed to deuterium plasmas. The ideality factors are better for these devices than for the hydrogen-treated HBTs. Being in the range 1.04-1.16. The Figure also shows the E-B breakdown voltages extracted from the reverse I-V characteristics.

The changes in emitter resistance as a function of source power and rf chuck power are shown in Figure 4-32 for both hydrogen and deuterium plasma exposure. The charges in emitter resistance are lower than those in the base resistance, which is consistent with the fact that acceptors are more easily passivated than donors in GaAs and AlGaAs. Therefore, while there are changes in the doping on both sides of the E-B junction, the effect is more pronounced in the base.

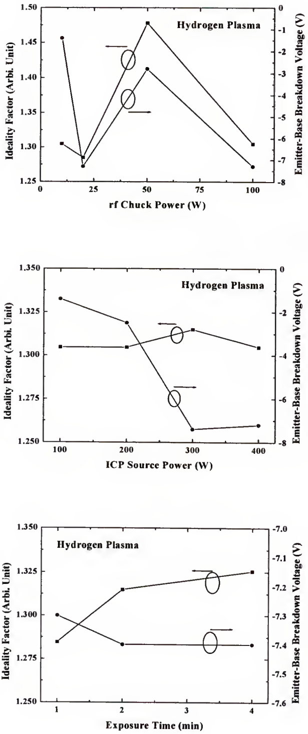

Figure 4-30. Ideality factor and E-B junction breakdown voltage as a function of rf chuck power (top), source power (center) or exposure time (bottom) for hydrogen plasmas.

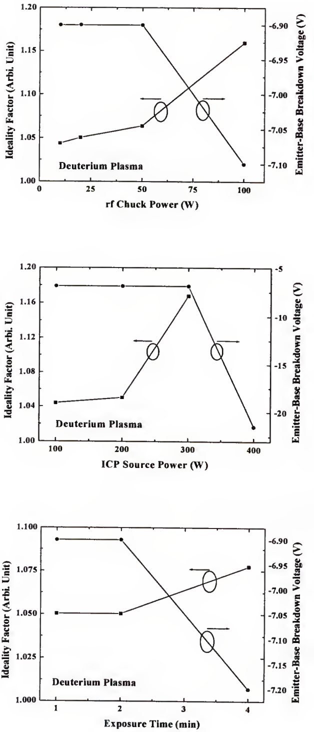

Figure 4-31. Ideality factor and E-B junction breakdown voltage as a function of rf chuck power (top), source power (center) or exposure time (bottom) for deuterium plasmas.

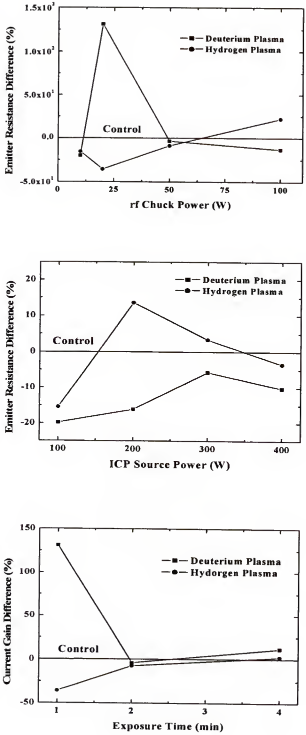

Figure 4-32. Emitter resistance change as a function of rf chuck power (top), source power (center) or exposure time (bottom) for both hydrogen and deuterium plasmas exposure.

The base resistance changes are shows for both hydrogen and deuterium plasma treatments as a function of source power, chuck power and exposure time in Figure 4-33. Note that very large increases in all cases, due to hydrogen or deuterium passivation of the carbon acceptors.

A systematic study of the effects of hydrogen or deuterium plasma processes (simulating deposition of dielectric sidewall spacers) on AlGaAs/GaAs HBTs has been performed. The base resistance shows a large increase under all conditions due to acceptor passivation, while current and E-B junction ideality factor do not show large changes. The E-B junction breakdown voltage is increased as a result of the decrease in effective doping in the base. Under same conditions it is advantageous to use deuterium rather than hydrogen to minimize changes to the HBT performance.

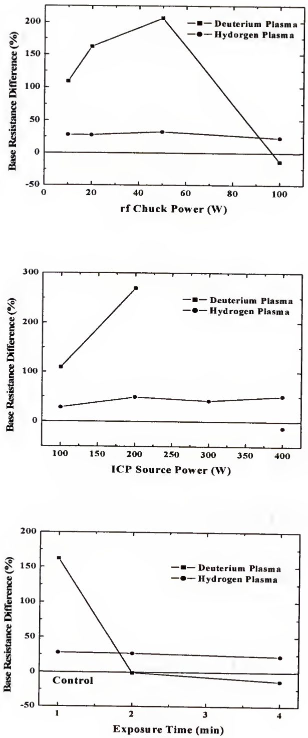

Figure 4-33. Base resistance change as a function of rf chuck power (top), source power (center) or exposure time (bottom) for both hydrogen and deuterium plasmas exposure.

CHAPTER 5
IRRADIATION HARDNESS OF III-V COMPOUND SEMICONDUCTOR DEVICES

5.1 Radiation Induced Damages in Standard MESFET

5.1.1 Introduction

Gallium Arsenide (GaAs) Metal Semiconductor Field-Effect-Transistor (MESFETs) based device and circuits are now commercially available and have been used in many civilian and military applications. The radiation hardness of GaAs MESFET is one of the critical factors for selection of the applications where radiation is encountered in certain military, nuclear industry and space applications. The device characteristics of MESFETs are affected by neutrons, electrons, gamma rays, and cosmic rays(184-190). The typical radiation damages are the displacement of atoms from their lattice sites, ionization of atoms, and interal energy changes(191). In this work, we investigate the ability of GaAs MESFETs to withstand long-term cumulative radiation of λ-ray irradiation from a 600Ci Cobalt^{60} source. MESFET characteristics of source-drain I-V characteristics, gate leakage current, saturation drain current, sub-threshold gate leakage current, and sheet resistance were monitored to study the effect of radiation.

5.1.2 Experimental

GaAs metal semiconductor field-effect-transistors (MESFETs) were fabricated using implantation technology. Silicon semi-insulating GaAs substrates were used as n-dopant and substrates. The doping concentration in the channel region is approximately 10^{17} cm^{-3}. AuGe/Ni based metallization was employed for the n-ohmic contacts. The contacts were formed with E-beam deposition and standard lift-off process. After deposition, the contacts were annealed at 420 °C for 30 sec in a rapid-thermal-annealing (RTA) system. The gate contact was Ti/Pt/Au. Transmission-Line-Method (TLM) test structure was formed along the device fabrication to determine the contact resistance (R_C), sheet resistance (ρ_S), and specific contact resistance (ρ_C).

An HP Model 4145B Semiconductor Parameter Analyzer was used to characterize the MESFET. All measurements were taken at different radiation dose levels, which depended on both time in the cobalt^{60} irradiator and distance from the 600 Ci source. The calibration of radiation dose was performed with radiachromic films and ion chamber radiation meters. ISP Technologies MD-55 films were used in the range from 0 to 50 Krads total dose and Far West Technologies HD810 films were used to the range up to 500Krads total dose. Two kinds of ion chambers were used in higher dose measurements.

5.1.3 Results and Discussion

The degradation mechanisms of in GaAs MESFETs from Cobalt^{60} irradiation typically are atom displacement and ionization. Several types of point defects are considered during radiation and the Frenkel defect is the most common one generated by the transfer of radiation energy to devices. The general radiation damage mechanisms are of two types: atomic displacements resulting in lattice defects, and changes at the molecular level. A combination of both mechanisms is important for electrical components such as semiconductors and insulators. Our study is only interested in the interaction of gamma rays with a compound semiconductor, gallium-arsenide (GaAs). The three processes that can play an important role are photoelectric absorption, Compton scattering and pair production. They result in sudden and abrupt changes in the γ-rays, and is in sharp contrast to the mechanisms for charged particles. GaAs Metal-Semiconductor Field-Effect-Transistor (MESFET) is a majority carrier device and will predominately be altered by the pair-production mechanisms with the creation of defect centers that trap electrons(192-194). These radiation-induced defects occupy a broad spectrum of energy levels inside the semiconductor energy gap and act as recombination centers or electron trap centers that cause a change in free carrier concentration, mobility and carrier lifetime(184).

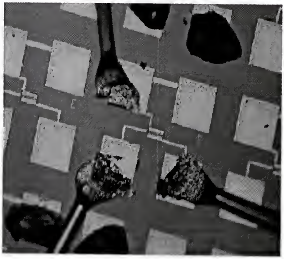

Figure 5-1: Photo of GaAs MESFET

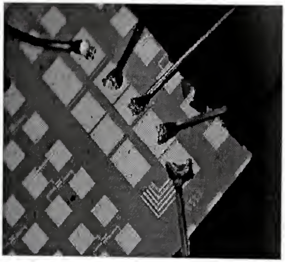

Figure 5-2: Photo of TLM Test Structure

The tested discrete MESFET and TLM pattern are shown in Figure 5-1 and 5-2. The dimension of discrete device is 1 × 35 μm^2 and the gaps of TLM pattern are 2, 4, 8, and 16 μm. Figure 5-3 shows the sheet resistance as a function of radiation dosage. Generally, the sheet resistance increased as the accumulative dose augmented, however, there were two regions observed. In the low radiation dose region (< 557MRADs), the sheet resistances increased slightly. In the high dose region (> 557Mrads), the sheet resistance was linearly proportional to the radiation dosage. The increase of sheet resistance is due to the formation of radiation-induced defects. MESFET is a majority carrier device. At low dosage level, the point defects induced within the substrate start to accumulate but the number of point defects are negligible compared to the free carrier concentration. With increasing radiation time and higher radiation dosage, more point defects accumulate inside the device. Once the defect concentration reached a certain level, distinct changes were observed in device characteristics. This explains why sheet resistance characteristic shows two different behaviors over the whole radiation dosage.

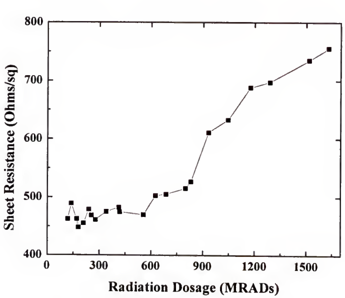

Figure 5-3. Sheet resistance as a function of radiation dosage.

Figure 5-4 and 5-5 show threshold voltage and sub-threshold voltage as a function of gate voltage at varied radiation dosage, respectively. There was a reduction in both of threshold voltages after λ-ray irradiation through the formation of electron trap centers. As shown in Figure 5-4, the threshold voltage didn't show obvious change until radiation dosage is higher than 750Mrads. In Figure 5-5, the range of change of sub-threshold voltage is within 1.5V. We didn't see any big difference in sub-threshold voltage in the dosage range from 800Mrads to 1630Mrads, although sub-threshold voltage showed a good trend versus radiation dosage from 120Mrads to 800Mrads. Therefore, sub-threshold voltage is not a suitable characteristic to use for tracking radiation induced changes.

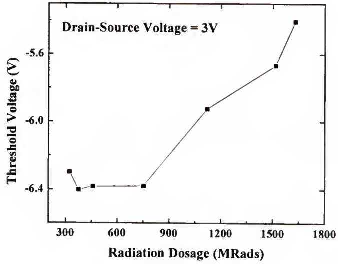

Figure 5-4. Sub-Threshold Voltage as a function of Gate Voltage at Varied Radiation Dosage.

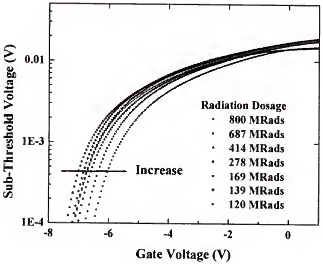

Figure 5-5. Sub-Threshold Voltage as a function of Gate Voltage at Varied Radiation Dosage.

Figure 5-6 shows the drain-source saturation current change before and after λ-ray irradiation and saturation current as a function of radiation dosage. Radiation-induced damage effects are observed in saturation current as illustrated in Figure 5-6. A drop in saturation current is caused mainly by the formation of electron trap centers within the active channel of the device. Both carrier concentration and mobility deteriorated due to radiation. The degradation of carrier mobility was result of increased scattering by radiation-induced defects. In Figure 5-7, measurements for radiation dosage higher than 169Mrads revealed a decrease in saturation current. The saturation current decreased monotonically with increasing radiation dosage and there was about 6mA drop in saturation current for a radiation dosage of 1630Mrads at gate voltage equal to -2V. Compared to sheet resistance, the saturation current is more sensitive to point defects and linear related to the radiation dosage than sheet resistance. Therefore, a radiation dosage detector can be made of a GaAs MESFET by monitor the sheet resistance or saturation current of the device.

The effects of λ-ray irradiation on GaAs MESFET dc characteristics were investigated. There was a trend shown in sub-threshold voltage, however, the change was not obvious enough to be used as a monitor of radiation. The changes of drain saturation current and sheet resistance showed a reversal proportion to the cumulative dosage of radiation. Therefore, drain saturation current and sheet resistance of GaAs MESFET can be employed as a indicator of radiation dosage from 120Mrads to 1630Mrads

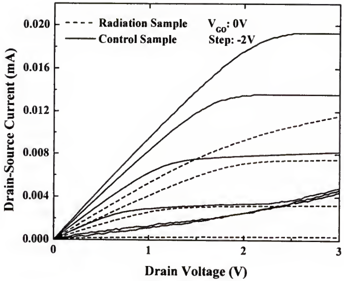

Figure 5-6. Drain-Source Saturation Current Change before and after λ-ray irradiation.

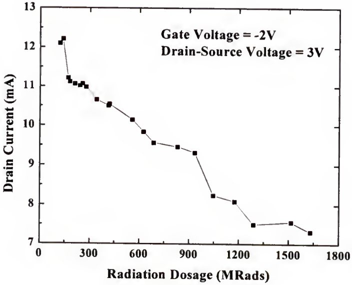

Figure 5-7. Drain saturation current as a function of the radiation dose.

5.2 Proton and Gamma-Ray Irradiation Effects on InGaP/GaAs Heterojunction Bipolar Transistors

5.2.1 Introduction

InGaP/GaAs Heterojunction Bipolar Transistors (HBTs) are widely used in wireless communication applications such as hand-held phones and satellite communication links(174-182, 195). The radiation hardness of HBTs is one of the critical factors that need to be established for military, space and nuclear industry applications. Previous results on AlGaAs/GaAs HBTs have indicated that these devices have superior γ-radiation resistance to GaAs metal-semiconductor field effect transistors (MESFETs) due to the higher doping levels in the active regions(196-202). There is little information available on the response of InGaP/GaAs HBTs to ionizing radiation. The replacement of AlGaAs as the emitter material by InGaP has been prompted by improving resistance to oxidation and better junction characteristics. Lower defect levels higher etch selectivity improved device performance and yield(175, 178, 195).

In this paper, we report a study of the effects of both γ-radiation and proton radiation on the dc performance of InGaP/GaAs HBTs. The devices were exposed to either a 600Ci Cobolt^{60} source for accumulated doses of 175 or 500 MRad or to a 40MeV proton beam for doses of 5×10^6 or 5×10^9 cm^{-2}. The proton irradiation conditions correspond to doses of 3.65 days to 10 years in low earth orbit.

5.2.2 Experimental

The layer structure were grown by Metal Organic Molecular Beam Exitaxy on undoped, semi-insulating GaAs(100) substrates(183). The n^+-GaAs Si-doped ($n=3\times10^{18}$ cm^{-3}) sub-collector (0.6μm thick) was followed by an n^--GaAs Si-doped ($n=2\times10^{16}$ cm^{-3})

collector (0.4μm thick), p^+-GaAs C-doped ($p=7\times10^{19}$ cm^{-3}) base (0.07μm thick), n^+-$In_{0.5}Ga_{0.5}P$ Si-doped ($n=8\times10^{18}$ cm^{-3}) emitter (0.08μm thick) and a 0.02 μm grade to a n^+-GaAs Si-doped ($n=1.5\times10^{19}$ cm^{-3}) emitter contact layer (0.2μm thick). HBTs with emitter dimension 75μm were fabricated by wet chemical etching. Lift-off of e-beam deposited Au/Ga/Ni and Ti/Pt/Au was employed for ohmic contacts to the emitter/collector and base layer, respectively(203).

The irradiations were performed in two separate facilities. For the Co^{60} source, the calibration of radiation dose was performed with radiochromic films and ion chamber radiation meters(204). The proton irradiations were performed at the Texas A&M cyclotron with 40MeV protons at fluences of 5×10^6 or 5×10^9 cm^{-2}, with the higher dose equivalent to at least 10 years exposure in low earth orbit(205). The projected range of the protons is > 50μm. Measurements were taken ~50 hours after irradiation. The device dc characteristics were measured at room temperature with an HP 4145B parameter analyzer.

5.2.3 RESULTS AND DISCUSSION

(a) γ-Irradiation

Where devices irradiated with the 175MRad dose shown no visible changes in appearance, the contact metal morphology was found to be degraded after the 500MRad exposure (Figure 5-8). This is not due to a temperature rise of the sample, but appears to be a main result of the γ-radiation on the metal or the oxide underneath the metal(202).

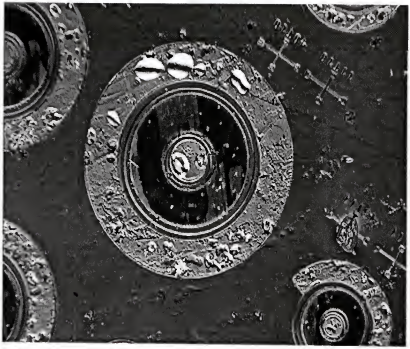

Figure 5-8. Optical micrograph of HBT after 500MRad γ-ray dose.

The forward current-voltage (I-V) characteristics from the emitter-base (e-b) junction are shown in Figure 5-9 (left) as a function of γ-dose. Let us examine the effect of the radiation exposure on the three different regions of the I-V curves, namely the generation-recombination region (V_F<0.7V), diffusion region (0.7<V_F<1.1V) and the series-resistance section (V_F>1.1V). At very low bias (<0.3V), there is an obvious increase in leakage current whose magnitude is proportional to dose. At slightly higher bias (0.3-0.5V), the higher dose HBT displays the effect of a reduction in free carrier density. In the diffusion current region of the I-V curves, the junction ideality factor (n) was calculated and is shown in Figure 5-9 (right). The n value increases only slightly with dose. In the region dominated by series resistance, there is most likely due to a decrease in free carriers because of deep traps created by the absorbed γ-rays.

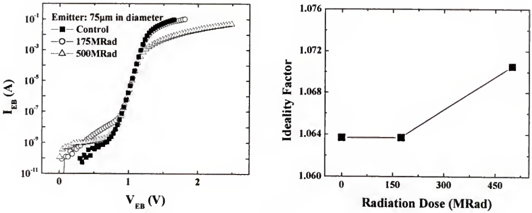

Figure 5-9. E-B junction forward I-V characteristics (left) and ideality factor (right) as a function of γ-ray dose.

The reverse I-V characteristics from the e-b junction are shown in Figure 5-10 (left) as a function of dose. The breakdown voltage (V_B) of this junction is determined by the competition between two mechanisms, namely creation of surface defects and bulk traps. For doses less than 175MRad, the reverse breakdown is dominated by surface recombination defects which increase the leakage current and produce a reduction in V_B (Figure 5-10, right). The higher doses the loss of free carriers by trapping into bulk defects dominates and leads to an increase of V_B towards the control value. These results are consistent with the forward I-V data.

A similar phenomenon was observed in the reverse breakdown characteristics from the base-collector (b-c) junction, as shown in Figure 5-11.

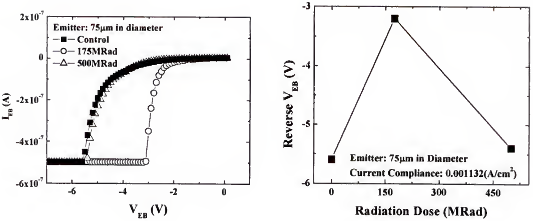

Figure 5-10. E-B junction reverse I-V characteristics (left) and reverse breakdown voltage (right) as a function of γ-ray dose.

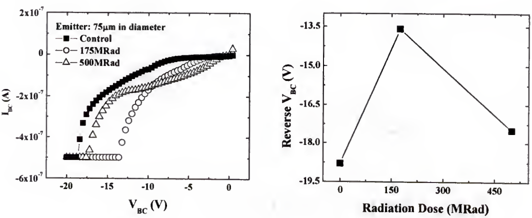

Figure 5-11. B-V junction reverse I-V characteristics (left) and reverse breakdown voltage (right) as a function of γ-ray dose.

The common-emitter characteristics from the HBTs before and after γ-irradiation are shown in Figure 5-12. The radiation damage causes two effects. The first effect is an increase in the turn-on voltage of the collector-emitter junction due to an increase in emitter resistance. The second effect is a change in slope of the initial part of the curves, due to an increase in collector resistance. These results are consistent with creation of deep electron trap states in both the emitter and collector layers.

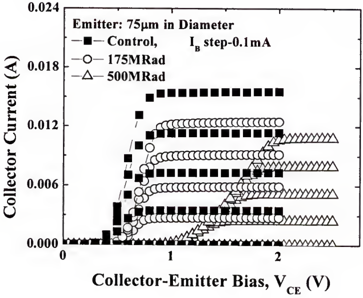

Figure 5-12. Common-Emitter characteristics before and after γ-irradiation at different doses.

The dc current gain in the HBTs was obtained from the Gummel plots for the different doses, as shown in Figure 5-13. The gain was found to decrease monotonically with dose from a control value of 48 down to 22 after the 500MRad dose. Both the base and collector currents were decreased by radiation exposure.

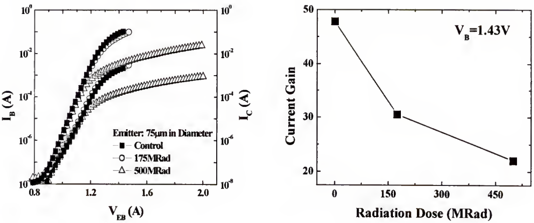

Figure 5-13. Gummel plots (left) and current gain (right) as a function of γ-ray dose.

(b)Proton Irradiation

The proton doses we employed did not degrade the contact metallization and did not have as large an effect on the forward e-b junction characteristics as the γ-radiation. Figure 5-14 (left) shows the I_B-V_{BE} characteristics as a function of proton dose, while the junction ideality factors are shown at the right of the figure. There is a relatively minor increase in the generation-recombination region of the characteristics, as shown in more detail in Figure 5-15 (left). In addition, the increase in series resistance of the junction is small (Figure 5-15, right). These results show the remarkable resistance of InGaP/GaAs HBTs to proton damage and the highly promising nature of these devices for space-borne Applications.

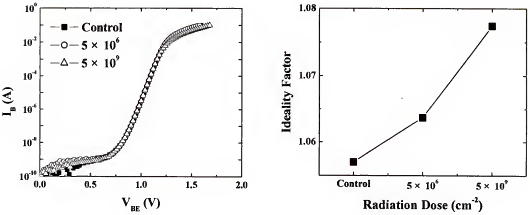

Figure 5-14. E-B junction forward I-V characteristics (left) and ideality factor (right) as a function of proton dose.

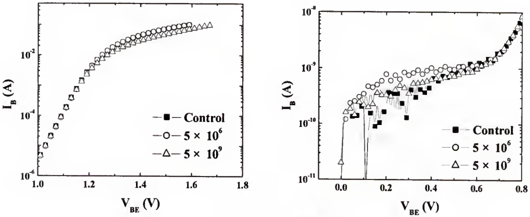

Figure 5-15. E-B junction forward I-V characteristics from series resistance dominated region (left) and generation-recombination region (right) as a function of proton dose.

Similar relatively small changes were observed in the reverse e-b junction I-V characteristics, as shown in Figure 5-16. The decrease in breakdown voltage is ~0.45V even after a dose of 5×10^9 proton/cm^2. Changes of a similar magnitude were observed in the base-collector junction breakdown voltage with an increase from –11.7V in the control devices to –12.3V in those exposed to 5×10^9 proton/cm^2.

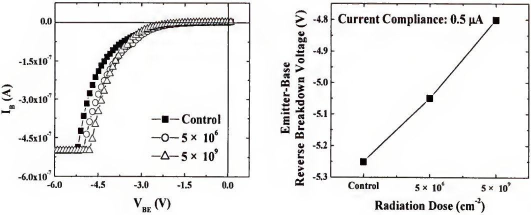

Figure 5-16. E-B junction reverse I-V characteristics (left) and reverse breakdown voltage (right) as a function of proton dose.

The common-emitter characteristics before and after the low dose exposure are shown in Figure 5-17 (left). For this condition, there is no shift in the turn-on voltage or change in slope of the characteristics. By sharp contact to the case of γ-irradiation, the collector current actually increases as a result of exposure to the proton beam. The right of Figure 5-17 shows the ratio of the collector current after proton irradiation to its value in control HBTs. These results suggest that at least some of the proton-induced damage has n-type nature and decrease the collector resistance.

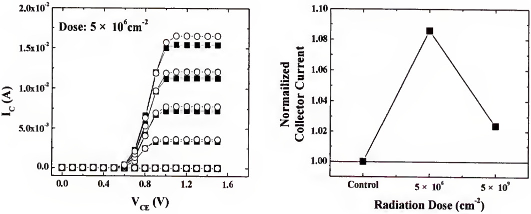

Figure 5-17. Common-emitter characteristics (left) and normalized change in collector current (right) as a function of proton dose.

Figure 5-18 (left) shows the Gummel plots before and after proton irradiation, while the right of the Figure shows the changes in dc current gain relative to the control value. Note that the gain remains above its initial value for both proton doses. The reason for the incresase in gain can be determined from the relative changes in base and collector sheet resistance (Figure 5-19), measured from transmission line data. The base resistance increases with proton dose (i.e. the carrier density decreases due to the introduction of hole traps), whereas the collector sheet resistance decreases under the same conditions. It is clear that the defects created by γ-radiation and proton damage differ in their electrical properties and hence on the effect on HBT performance.

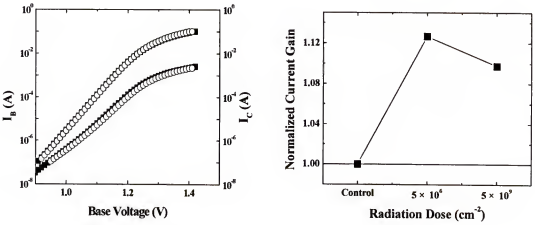

Figure 5-18. Gummel plots (left) and normalized current gain (right) as a function of proton dose.

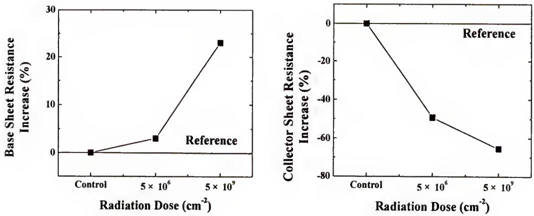

Figure 5-19. Percentage change in base (left) or collector (right) sheet resistance as a function of proton dose.

The InGaP/GaAs HBTs show a remarkable resistance to both proton and γ-ray induced degradation. The proton-irradiated devices show small changes in junction ideality factor, generation-recombination leakage current and dc current gain at doses equivalent to approximately 10 years in low earth orbit. The γ-irradiated HBTs show a decrease in current gain of roughly 50% after a dose of 500MRad. The InGaP/GaAs HBTs appear to be very promising for terrestrial or space-borne applications where radiation-resistance is desirable.

5.3 dc and rf Performance of Proton-Irradiated AlGaN/GaN High Electron Mobility Transistors

5.3.1 Introduciton

High electron mobility transistors(HEMTs) fabricated in the AlGaN/GaN material system show great potential for both space-borne and terrestrial applications where high power and elevated temperature operation are needed(76, 206-212). For satellite-based communication systems, weather forecasting, remote sensing or nuclear industry applications, the radiation resistance of electronics devices must be established. One would expect the AlGaN/GaN system to be even more radiation-hard than the more conventional AlGaAs/GaAs heterostructure due to the higher displacement energies in the nitrides(213). Previous reports have shown significant (>50%) decreases in transconductance of AlGaN/GaN HEMTs irradiated with 1.8MeV protons to doses of 10^{14}cm^{-2} (214). We have reported smaller changes (<30%) in transconductance in similar HEMTs exposed to higher energy (40MeV) protons at lower doses (5×10^{10}cm^{-2})(215).

In this paper we report on the irradiation dose effects on the dc performance of different AlGaN/GaN HEMTs. The exposed proton doses were equivalent to more than 100 years in low-earth orbit. In addition, post-irradiation annealing at 300°C was studied for various annealing times.

5.3.2 Experimental

The samples were grown by rf-plasma activated Molecular Beam Epitaxy on 2 inch diameter sapphire substrates(216). The layer structure and device schematic are shown at the right of Figure 1. The contacts were formed by lift-off of e-beam evaporated metal, with the ohmic metallization annealed at 850°C for 30secs. The Schottky gates were formed by optical lithography for 1.2 μm gate length and e-beam lithography for 0.8μm gates. The gate widths were varied from 100-200μm. An optical micrograph of a completed device is shown at the left of Figure 5-20. The devices were measured before after irradiation with 40MeV protons at fluences of 5×10^{9}-5×10^{10}cm^{-2}. Post-irradiation annealing was performed at 300°C under N_2 for periods of 1-8 minutes.

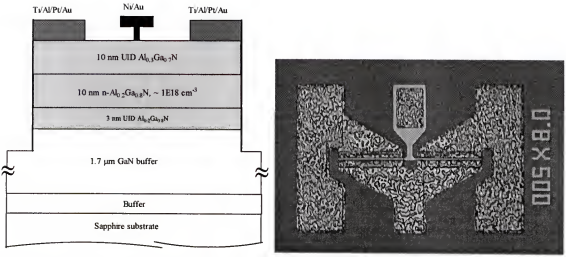
Ti/Al/Pt/Au
Ni/Au
Ti/Al/Pt/Au
10 nm UID $Al_{0.3}Ga_{0.7}N$
10 nm n-$Al_{0.2}Ga_{0.8}N$, ~ 1E18 cm^{-3}
3 nm UID $Al_{0.2}Ga_{0.8}N$
1.7 μm GaN buffer
Buffer
Sapphire substrate
0.8X500

Figure 5-20. HEMT schematic (left) and optical micrograph of completed device (right).

5.3.3 Results and Discussions

Figure 5-21 shows transfer characteristics of the smallest ($0.8\times100\mu m^2$) and largest ($1.2\times200\mu m^2$) HEMTs before and after proton irradiation. The extrinsic transconductance (g_m) decreases more with the higher fluence and the peak shifts to slightly more positive gate voltages along with the threshold voltage (V_{TH}). Since $g_m = \partial I_{DS}/\partial V_G$, the decrease with irradiation can be explained by a decrease in drain-source current due to an increase in channel resistance.

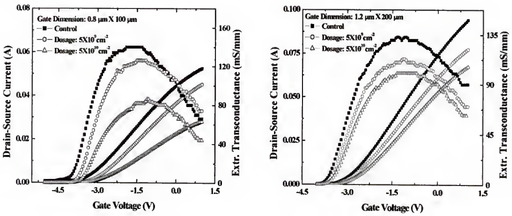

Figure 5-21. Transfer characteristics for 0.8×100μm^2 (left) and 1.2×200μm^2 (right) HEMTs before and after proton irradiation.

Figure 5-22 shows the variation of g_m with proton dose as a function of both HEMT gate length and width. There is no systematic effect of device size on the decrease in g_m for either of the proton fluences. Note the relatively small percentage decrease (9-15%) for a dose of 5×10^{9}cm^{-2}, corresponding to more than 10 years in low earth orbit.

Supporting evidence for the notion that the proton irradiation leads to an increase in channel resistance comes from the data in Figure 5-23, showing the reverse breakdown voltage (V_B) as a function of dose. Since V_B is inversely proportional to the doping in the channel, this data suggests that the protons traversing the devices (the projected range of 40MeV protons is >50μm) create deep trap states that remove electrons.

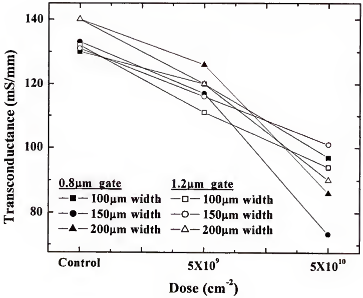

Figure 5-22. Transconductance as a function of proton fluence for HEMTs with different gate lengths and gate widths.

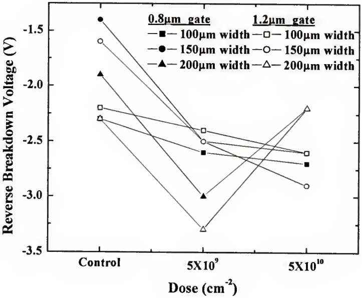

Figure 5-23. Reverse breakdown voltage from devices with different gate lengths and widths, as a function of proton fluences.

Figure 5-24 shows the drain-source current-voltage characteristics (I_{DS}-V_{DS}) from $0.8\times100\mu m^2$(left) and $0.8\times100\mu m^2$(right) devices before and after irradiation. The main effect of the proton-induced damage is a reduction in I_{DS}, which could be due either to a decrease in electron concentration in the channel or a decrease in saturated carrier velocity. The initial slope of the curves at low bias also shows a decrease. This has previously been ascribed to a decrease in both carrier density and mobility in proton-damaged AlGaN/GaN HEMTs(214). The decrease in I_{DS} is 30-50% at the highest dose employed here.

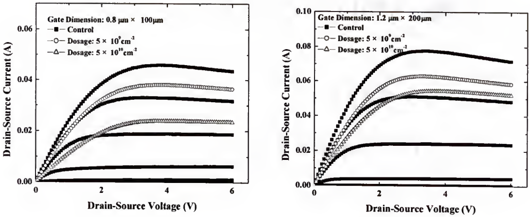

Figure 5-24. I_{DS}-V_{DS} characteristics from $0.8\times100\mu m^2$ (left) and $1.2\times200\mu m^2$ (right) HEMTs before and after proton irradiation at two different fluences. In the case of the irradiated devices, only the uppermost curves are shown for the sake of clarity.

The forward I-V characteristics from HEMTs with two different sets of gate widths and lengths are shown in Figure 5-25 for both the pre- and post-irradiation conditions. The current is decreased over the entire voltage range, which again is consistent with an increase in channel resistance as a result of the proton irradiation. There was no significant change in ideality factor in the HEMTs and little difference in forward current density for the two different proton fluences.

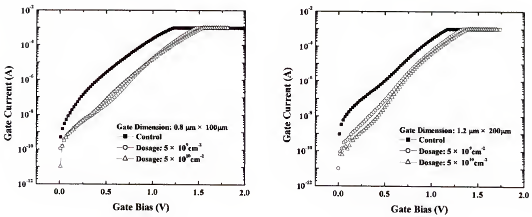

Figure 5-25. Forward gate characteristics from $0.8 \times 100 \mu m^2$ (left) and $1.2 \times 200 \mu m^2$ (right) HEMTs before and after proton irradiation at two different doses. The flat regions at high forward bias are due to compliance limits on the test setup.

The reverse recovery characteristics from control and proton-damaged HEMTs switched from 2V to -3V are shown in Figure 5-26 for $1.2 \times 200 \mu m^2$ devices. Apart from the reduced forward current levels in the irradiated HEMTs, there is no significant change in the switching time. We propose that this is due to the very small minority carrier lifetime in n-GaN, so that the introduction of additional defects into the material does not further degrade it to a measurable extent. A recent review of minority carrier properties in GaN shows that this lifetime is typically of order a few nanoseconds(217).

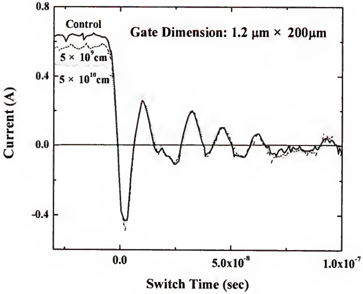

Figure 5-26. Reverse recovery characteristics for 1.2×200µm^2 HEMTs before and after proton irradiation.

The increase in channel resistance in the irradiated HEMTs led to a decrease in the maximum frequency of oscillation (f_{MAX}) of the devices. Figure 5-27 shows the variation of f_{MAX} with gate length and width for the two different proton doses. The decrease in f_{MAX} is more obvious for shorter gate lengths with changes up to 50% for 0.8µm HEMTs. This is likely a result of the lower capacitance of these devices relative to 1.2µm gate length HEMTs, so that an increase in channel resistance has a larger effect on f_{MAX}. The reverse recovery characteristics of all the HEMTs remained unchanged within experimental error, with a switching time of ~1.6×10^{-8} sec for switching from +2V to -3V. The minority carrier lifetime is already so small in GaN that additional defect creation does not appear to degrade it(218-220).

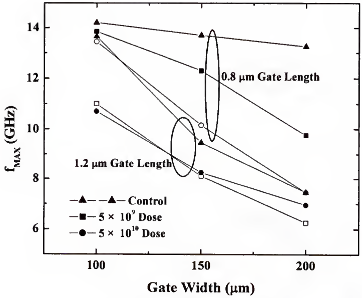

Figure 5-27. f_{MAX} as a function of gate width for 0.8 and 1.2μm gate length HEMTs before and after proton irradiation at two different doses.

Once a device has been irradiated, there is a limit to the temperature at which it can be annealed because of thermal degradation of the Schottky metallization. We chose to investigate the effects of post-irradiation annealing at 300°C for various times to see if this process could restore the dc performance parameters. Figure 5-28 shows V_{TH} and V_B as a function of annealing time at 300°C. Note that the annealing process changes both parameters in the unirradiated (control) sample and that is only partial recovery in the irradiated devices (i.e. they do not come back to the values in the control sample).

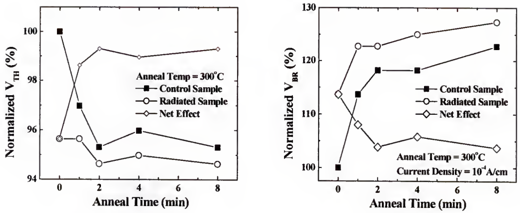

Figure 5-28. V_{TH} (left) and V_B (right) for 1.2×200μm^2 HEMTs irradiated with protons to a dose of 5×10^{10}cm^{-2} and then annealed at 300°C for various periods.

A more clear-cut demonstration of the role of annealing is shown in Figure 5-29. Both g_m and I_{DS} show an initial improvement after annealing the irradiated devices for 1 minute, but essentially no further change with annealing up to 8 minutes. Once again, there is only partial recovery in both parameters, with each reaching ~70% of the control values.

The transconductance, drain-source current, forward gate current and reverse breakdown voltage all show changes upon proton irradiation, consistent with a decrease in electron concentration in HEMT channel. The main degradation mechanism is removal of carriers from the device channel by damage-related traps. Reverse recovery switching times in the HEMTs were unaffected by the proton fluences we investigated. Annealing at 300°C restores g_m and I_{DS} to ~70% of their values in unirradiated HEMTs. The HEMTs appear to be promising for terrestrial or aerospace applications where radiation-resistance is desirable.

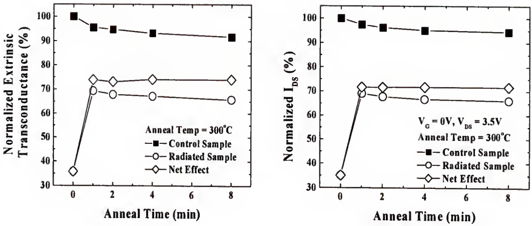

Figure 5-29. Normalized g_m (left) and I_{DS} (right) for 1.2×200μm^2 HEMTs irradiated with protons to a dose of 5×10^{10}cm^{-2} and then annealed at 300°C for various periods.

CHAPTER 6
PASSIVATION EFFECTS OF MBE-GROWTH OXIDES ON NITRIDE HEMT DEVICES

6.1 Effect of Plasma Enhanced Chemical Vapor Deposition of SiN_X on n-GaN Schottky Rectifiers

The electrical properties of lateral geometry GaN Schottky rectifiers were measured before and after deposition of SiN_X passivation layers by conventional capacitively-coupled plasma enhanced chemical vapor deposition. The rectifiers showed changes in reverse breakdown voltages and higher forward leakage currents for all plasma deposition conditions. The change in rectifier performance was found to depend on plasma exposure time, incident ion energy, atomic hydrogen neutral flux and film stress.

6.1.1 Introduction

There is increasing interred in the use of GaN-based electronic devices for high power, high temperature applications in more-electric automobiles, aircraft and ships and in utility switching for power flow control(96, 98, 99, 221-225). The simple GaN Schottky rectifier would be an integral part of an inverter module for power switching and there have been a number of recent reports of high breakdown voltages in both lateral and vertical geometry diode rectifiers(99-105, 226-231). It is obvious that these devices will require stable surface passivation/encapsulation layers in real-world applications. While SiO_2 is one choice, there have been reports of rapid oxygen diffusion into GaN during plasma enhanced chemical vapor deposition (PECVD) of this dielectric(232). The other obvious choice is SiN_X. In this paper we report on the electrical characteristics of n-GaN diode rectifiers after PECVD of thin (≤ 300Å) layers. These layers were thin enough that we could probe directly through them to the underlying contacts on the GaN, thus avoiding potential problems arising from plasma or wet-etch removal of the SiN_X. The forward and reverse current-voltage characteristics and the capacitance-voltage characteristics from the diodes were measured as a function of the plasma applied power, process pressure and SiH_4/NH_3 ratio during the SiN_X deposition. The variations in electrical characteristics of the rectifiers were a strong function of the plasma parameters during the dielectric deposition and could be explained by invoking mechanisms involving loss of nitrogen from the GaN surface.

6.1.2 Experiment

The GaN layers were grown by hydride vapor phase epitaxy to a thickness of ~ 60μm on c-plane Al_2O_3 substrates. The near surface carrier concentration was $\sim 2.5 \times 10^{16}$ cm^{-3}. Lateral rectifiers were fabricated by lift-off of e-beam deposited Pt/Au rectifying contacts (125μm diameter) and Ti/Al/Pt/Au ohmic contacts. The latter were deposited first and were annealed at 850°C for 30 sec to produce the lowest contact resistivity ($\sim 10^{-6}$ Ω-cm^2). The current-voltage (I-V) and capacitance-voltage characteristics were recorded on an HP4145A parameter analyzer at room temperature as a function of the plasma deposition parameters.

Thin (~200Å) layers of SiN_X were deposited at a substrate temperature of ~255°C using 2% SiH_4 in N_2, 5% NH_3 in N_2 and a separate N_2 flow as the precursors in a Plasma-Therm SLR 730 PECVD reactor. The silane flow rate was held constant at 100 standard cubic centimeters per minute (sccm), the N_2 flow rate at 400sccm, while the ammonia flow rate was varied from 23-160sccm. The process pressure was varied in the range 400-900mtorr, while the rf (13.56MHz) applied power was varied from 30-300W. The deposition rate, refractive index and wet etch rate of SiN_X in buffered HF at 25°C were all measured as a function of the plasma parameters.

6.1.3 Results and Discussion

Figures 6-1, 6-2 and 6-3 shows the variation of SiN_X deposition rate, refractive index and wet etching rate with process pressure(Figure 6-1), rf applied power(Figure 6-2) and SiH_4/NH_3 ratio by total flow rate(Figure 6-3). The deposition rate was almost proportional to process pressure over the range we investigated, saturated with increasing rf power and went through a maximum with SiH_4/NH_3 ratio. The refractive index saturated with process pressure, decreased with applied plasma power and increased with SiH_4/NH_3 ratio. The wet etching rate decreased with increasing process pressure and SiH_4/NH_3 ratio and increased with increasing plasma power. These trends are likely to originate in the amount of atomic hydrogen incorporated into the SiN_X under different deposition conditions and in the degree of densification by ion bombardment under ion energy values in which broken bonds are not being created in the growing film. The deposition rate is of particular interest in the present work because it determines how quickly the GaN surface is protected against further exposure to the plasma.

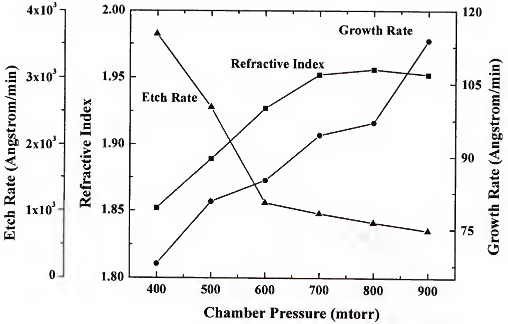

Figure 6-1. SiN_X deposition rate, refractive index and wet etching rate as a function of chamber pressure.

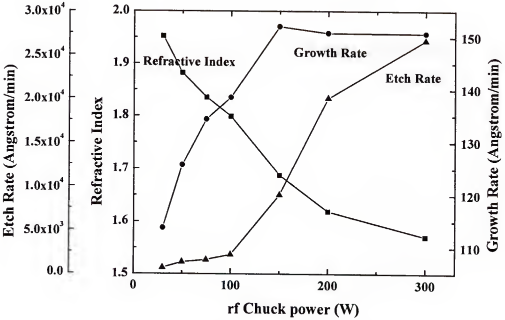

Figure 6-2. SiN_X deposition rate, refractive index and wet etching rate as a function of rf chuck power.

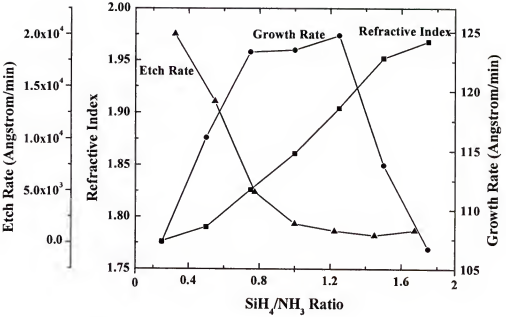

Figure 6-3. SiN_X deposition rate, refractive index and wet etching rate as a function of SiH_4/NH_3 flow ratio.

Figure 6-4 shows the reverse I-V characteristics from the rectifiers as a function of pressure(top), rf applied power(center) and SiH_4/NH_3 ratio(bottom). A decrease in reverse breakdown voltage (V_B), defined as the reverse bias at which the current density reached 1mA-cm^{-2}, is only observed at high process pressures, rf power and high SiH_4/NH_3 ratios. Let us examine the possible reasons in each case. In the case of variations in process pressure, the SiN_X deposition rate is highest at the highest pressures. In this situation, it appears that the exposure time of the GaN surface is less important than the concentration of active species in the plasma. It is plausible that the higher hydrogen content present at higher pressures leads to degradation of the GaN surface enough preferential loss of nitrogen according to the reaction $GaN + H^\circ \rightarrow NH_3 + GaN + N_V$, where N_V are nitrogen vacancies which have shallow donor states in the GaN bandgap. The increased n-type doping near the surface would produce surface-initiated breakdown at lower biases than in stoichiometric material(98). In the case of varying the rf power applied to the plasma, the degradation in V_B is highest at either very low or very high powers. In the situation of low applied powers, the SiN_X deposition rate is small and therefore the GaN surface is exposed to the ion flux and atomic hydrogen neutral flux for a relatively longer time. In the situation of high applied powers, both of these fluxes will be larger and hence result in more degradation of the GaN surface even though the exposure time to the plasma will be shorter. In the case of varying the SiH_4/NH_3 ratio, the decreases in V_B occurred for the highest values of this parameter, i.e. where the deposition rate has a minimum (see Figure 6-3). Once again, under these conditions the exposure time of the GaN surface to the energetic ion bombardment and chemically active flux from the plasma will be maximized.

Figure 6-5 shows the numerical values of V_B from the GaN rectifiers plotted as a function of process pressure(top), rf applied power(center) and SiH_4/NH_3 ratio(bottom). Note that the dc chuck self-bias was very low (-15V) during the depositions in which both pressure and gas ratio were varied. The average incident ion energy is roughly the sum of this bias voltage and the plasma potential, which is very low (≤-10V) at these high pressures. For low ion energy conditions, the increase in V_B occurs mainly through passivation of defect states on the GaN surface because the energy needed to displace on atom in a semiconductor by ion bombardment is typically in the range 25-50eV. For the case of varying the rf chuck power (Figure 6-5, center), we believe the fact that V_B exhibits a maximum results from a competition between SiN_X deposition rate and incident ion energy as to which is the dominant degradation mechanism for the GaN surface.

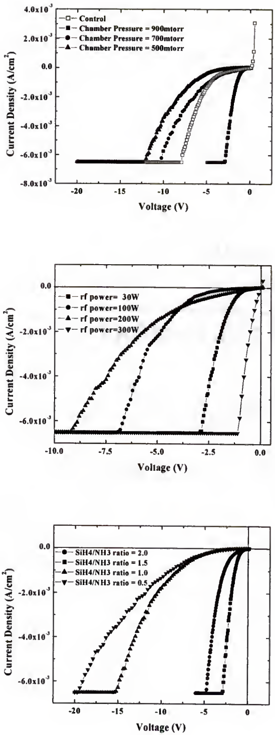

Figure 6-4. Reverse I-V characteristics for GaN rectifiers before and after deposition with SiN_X as a function of chamber pressure(top, where 30W of rf power was used), applied rf power(center, at a pressure of 900mtorr) or SiH_4/NH_3 flow ratio(bottom, at an rf power of 30W and a pressure of 900mtorr).

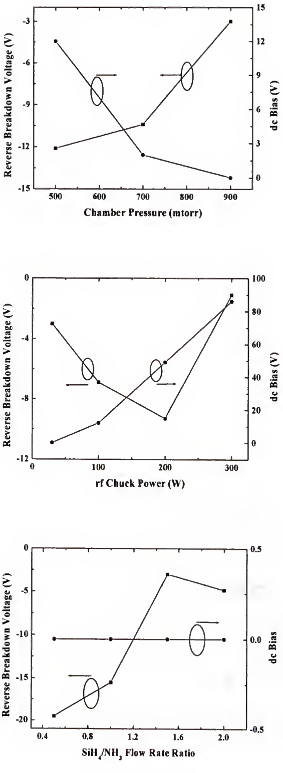

Figure 6-5. Reverse breakdown voltage for GaN rectifiers deposited with SiN_X as a function of chamber pressure (top), applied rf power(center) or SiH_4/NH_3 ratio(bottom).

The forward I-V characteristics from the rectifiers are shown in Figure 6-6 as a function of process pressure(top), rf applied power(center) and SiH_4/NH_3 ratio(bottom). Note in all cases that there is an increase in the low-bias (<1V) forward current in the rectifiers. Since the contacts were already in place prior to the SiN_X deposition, the increase in current is not due to a decrease in barrier height but rather originates in leakage current from surface states. The effective barrier heights were obtained from the relationship:

$$J = A^{**}T^2 \exp(-\frac{e\phi_B}{K_B T})\left[(\frac{eV}{nK_B T}) - 1\right] \tag{6-1}$$

where A^{**}, the Richardson constant, is 26.4 A/cm^2-K^2 for n-GaN, J the current density, T the measured temperature, Φ_B the barrier height, n the ideality factor and K_B is Boltzmann's constant. The control (undeposited) rectifiers had Φ_B values of ~0.99eV and n values of ~1.4. The changes in n as a function of process conditions are shown in Figure 6-7. In general, these ideality factors increase significantly upon SiN_X deposition if the rf applied power is high or chamber pressure is low. Under conditions of low rf power(<200W) or high pressure (≥650mtorr) there is even a slight improvement in n, which may be related to passivation of defect states around the periphery of the rectifying contact.

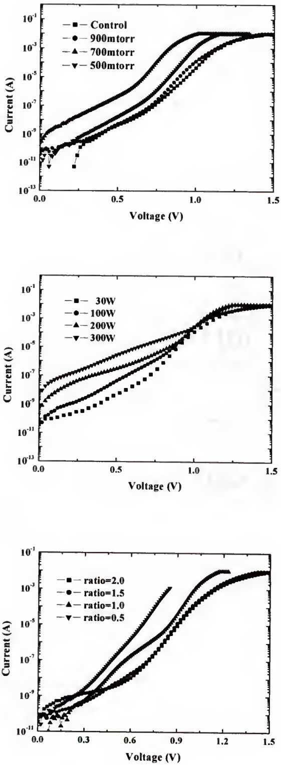

Figure 6-6. Forward I-V characteristics for GaN rectifiers before and after deposition with SiN_X as a function of chamber pressure(top), applied rf power(center) or SiH_4/NH_3 ratio(bottom).

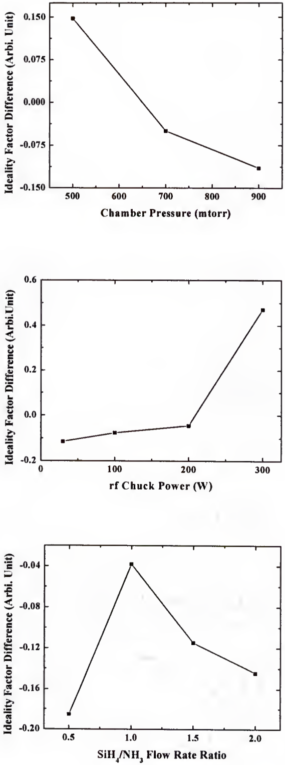

Figure 6-7. Change in diode ideality factor for GaN rectifiers after deposition of SiN_X as a function of chamber pressure(top), applied rf power(center) or SiH_4/NH_3 ratio(bottom).

Finally, C-V measurements performed before and after the SiN_X deposition showed significant changes in the effective carrier concentration under the gate contact, as shown in Figure 6-8. These trends correlated with the refractive indices in the deposited SiN_X films (compare data in Figures 6-1 and 6-8), which implicates the stress induced in the GaN by the deposition. These piezo-induced electrons also play a role in altering the breakdown characteristics of the rectifiers and point up need to optimize the stress properties of the dielectric for real-world applications(211, 233). Note however that there are the additional factors mentioned earlier such as preferential nitrogen loss from the surface and ion-induced damage which are dominant under most deposition conditions.

PECVD of SiN_X passivation layers can have a profound effect on the I-V characteristics of GaN Schottky rectifiers. The reverse breakdown voltages are found to decrease under some of the deposition conditions employed, while the forward leakage current is increased in all cases. These parameters are a strong function of the process pressure, applied plasma power and SiH_4/NH_3 ratio used for the SiN_X deposition, which in turn determine the amount of time the GaN surface is exposed to the plasma, the incident ion energy and neutral atomic hydrogen flux. There appear to be at least three mechanisms by which the rectifier performance may be degraded, including preferential loss of nitrogen from the GaN surface, piezo-induced carriers and ion damage. Plasma deposition conditions that minimize the plasma exposure time, average ion energy and stress in the SiN_X film lead to an improvement in reverse breakdown voltage of the rectifiers.

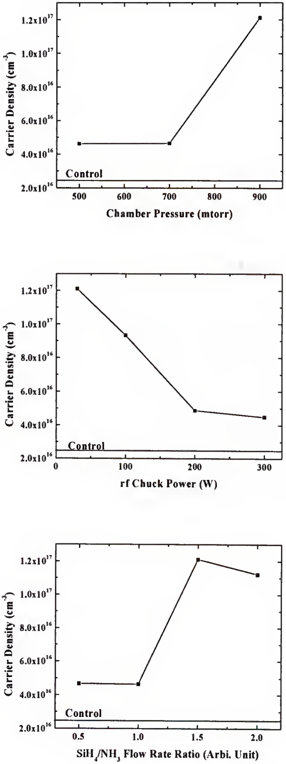

Figure 6-8. Carrier density obtained from C-V measurements on GaN rectifiers after deposition of SiN_X as a function of chamber pressure(top), applied rf power(center) or SiH_4/NH_3 ratio(bottom).

6.2 Influence of PECVD Deuterated SiNX on GaAs MESFETs and GaAs/AlGaAs HBTs

The degradation of electrical characteristics of GaAs MESFETs and HBTs can occur during PECVD of SIN_X passivation films through the hydrogen passivation of dopants or creation of deep traps by ion bombardment or preferential loss of As. In this paper we report in the dc characteristics of MESFETs and HBTs deposited with SiN_X using deuterated precursors (SiD_4/ND_3). For the MESFETs, changes in I_{DS}, g_m and channel sheet resistance were typically $\leq 25\%$, with process pressure being the most important parameter. For the HBTs, changes in β and sheet resistance of the base and emitter layers were again typically $\leq 15\%$ for the conditions we investigated.

6.2.1 Introduction

GaAs/AlGaAs heterojunction bipolar transistors (HBTs)(136-146, 234-244) and GaAs metal semiconductor field effect transistors (MESFETs) form the basis of high speed lightwave communication systems, microwave power amplifiers and digital wireless devices(144-158, 165-173, 245-252). In both types of device, a key processing step is the deposition of an encapsulation/passivation layer, which is usually a dielectric such as SiN_X(162). Since this step is typically carried out by plasma enhanced chemical vapor deposition (PECVD) using SiH_4 and NH_3 as the precursors, there are a number of possible problems that may arise due to changes in the electrical properties of the GaAs upon exposure to the plasma environment. One of these uses is the hydrogen passivation of donors in the MESFET channel or HBT emitter/collector layers through the reaction

$$Si^+ + H^- \rightarrow (SiH)^0 \qquad (6\text{-}2)$$

Or the hydrogen passivation of carbon acceptors in the HBT base through the reaction.

$$C^- + H^+ \rightarrow (CH)^0 \qquad (6\text{-}3)$$

A second potential problem is creation of surface states around the periphery of the device contacts through ion bombardment from the plasma. These defect states may include those due to preferential loss of the group V element through reaction with atomic hydrogen.

One method for minimizing these effects is to use deuterated precursors for the PECVD of SiN_X. The potential advantages are the lower diffusivity of ^2H relative to ^1H (by a factor of $\sqrt{2}$ at all temperatures) and the shallower range of $^2H^+$ ions. In this paper we report on the effects of PECVD of SiN_X using SiD_4 and ND_3 on the dc performance of GaAs MESFETs and GaAs/AlGaAs HBTs.

6.3.2 Experiment

(a) MESFETs

The semi-insulating GaAs surface were given a blanket implant of $^{29}Si^+$ ions at a dose of a $3\times10^{12}cm^{-2}$ at 50keV in selected areas to form the source/drain regions. Annealing at 900°C for 10s was performed capless in a Heatpulse 410 rapid annealer under a flowing N_2 ambient with the wafers contained in SiC-coated graphite susceptor. An overpressure of arsenic vapor was provided by filling reservoirs in graphite susceptor with powdered GaAs. Contacts were formed by lift-off of Au/Ge/Ni/Au (alloyed at 420°C, 30s) for source/drain and Ti/Pt/Au for the gate. The gate length was 1μm and width 30μm. The dc characteristics were measured on a parameter analyzer.

(b) HBTs

The HBTs were grown on semi-insulating, (100) GaAs substrates by metal organic molecular beam epitaxy, as described previously. The layer structure consisted of 6000Å Si-doped n^+-GaAs ($n=3\times10^{18}cm^{-3}$) subcollector, 4000Å Si-doped n-GaAs ($n=2\times10^{16}cm^{-3}$) collector, 700 Å C-doped p^+-GaAs ($p=7\times10^{19}cm^{-3}$) base, 800 Å Si-doped n^+-$Al_{0.3}Ga_{0.7}As$ ($n=8\times10^{18}cm^{-3}$) emitter, a 200Å grade to a 2000Å Si-doped n^+-GaAs ($n=1.5\times10^{19}cm^{-3}$) emitter contact layer. Large area (emitter diameter of 90μm) HBTs were fabricated with wet chemical etching and used AuGeNi based metallization for emitter contacts and Ti/Pt/Au for the base contacts.

Both the MESFETs and HBTs were deposited with ~125 Å of SiN_X using SiD_4 and ND_3 as the precursors at a temperature of 255°C. The rf input power was varied from 30-150W(13.56MHz) and process pressure from 600-900mTorr. The devices were test by probing through the dielectric to the underlying contacts.

6.3.3 Results and Discussion

(a) MESFETs

Figure 6-9 shows the I_{DS}-V_{DS} and gate current characteristics from MESFETs deposited with SiN_X at different pressures. From data of this type we were able to construct the plots of Figure 6-10, which shows the effect of process pressure on the drain-source current (I_{DS}), transconductance (g_m), reverse breakdown voltage (V_{BR}) and channel sheet resistance (R_S). Both I_{DS} and g_m show a linear variation with process pressure. This is consistent with the carrier loss being mainly due to creation of deep traps by ion bombardment since the ion flux will be higher at lower pressure. The sheet resistance change is also larger at lower process pressure. However, the reverse breakdown voltage shows its largest decreases at the highest pressure. This suggests that V_{BR} is dominated by surface leakage pass around the contact periphery and that these states may be related to preferential loss of As.

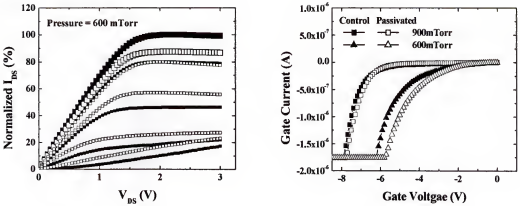

Figure 6-9. I_{DS}-V_{DS} (left) and gate current (right) characteristics from MESFETs deposited with SiN_X at different pressures.

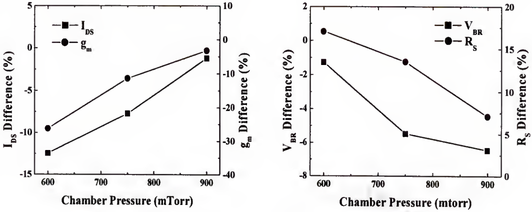

Figure 6-10. Changes in I_{DS} and g_m (left) and V_{BR} and R_S (right) from MESFETs deposited with SiN_X at different pressures.

Figure 6-11 shows the effect of SiD_4/ND_3 ratio on I_{DS}, gm V_{BR} and R_S. Once again I_{DS}, g_m and R_S show their largest change at the highest SiD_4/ND_3 ratio, which indicates that the atomic deuterium concentration is highest under these conditions. Similarly, V_{BR} shows the inverse trend, which indicates that loss of carriers is not the dominant mechanism for the changes in this parameter.

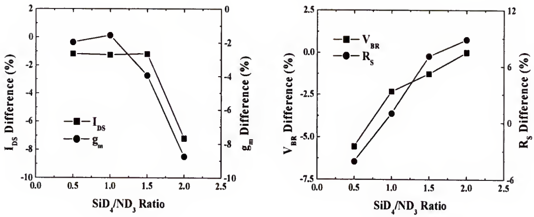

Figure 6-11. Changes in I_{DS} and g_m (left) and V_{BR} and R_S (right) from MESFETs deposited with SiN_X at different SiD_4/ND_3 gas flow ratios.

The effect of rf plasma input power during the SiN_X deposition is shown in Figure 6-12. Note that the relative magnitude of the changes in I_{DS} and g_m are small ($< \pm 5\%$), which V_{BR} and R_S go through maximum or minimum with rf power during the deposition.

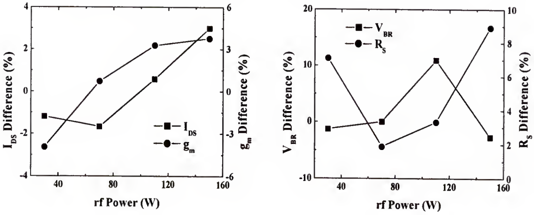

Figure 6-12. Changes in I_{DS} and g_m (left) and V_{BR} and R_S (right) from MESFETs deposited with SiN_X at different rf powers.

(b) HBTs

Figure 6-13 shows the B-C reverse I-V characteristics and gummel plots before and after SiN_X deposition at 110W rf power, SiD_4/ND_3 flow rate ratio of 1.5, chamber pressure of 900mTorr and deposition temperature of 255°C. There was actually a bigger increase in reverse BC junction breakdown voltage at 30W rf power, which indicates that the HBT behavior is more affected by hydrogen passivation of dopants rather than creation of deep traps by ion bombardment.

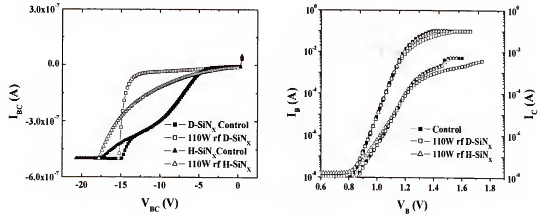

Figure 6-13. I_{BC}-V_{BC} (left) and Gummel plots (right) from HBTs before and after deposition with SiN_X using either hydrogenated or deuterated precursors at 110W rf power.

Figure 6-14 shows a comparison of the effects of deuterated verse hydrogenated precursors on the change of BC reverse breakdown voltage and current gain (β) in the HBTs, as a function of the rf power during SiN_X deposition, along with the changes in base and emitter sheet resistance ($R_{S\text{-}BASE}$ and $R_{S\text{-}EMITTER}$, respectively). Note that the current gain differences are small (≤2%), which the sheet resistance changes are larger (≤15%). The largest effect is seen on the V_{BR} of the BC junction. This breakdown voltage is inversely proportional to the carrier concentration in the base and collector layers. The change in current gain can be explained from the observed changes in emitter and base sheet resistance.

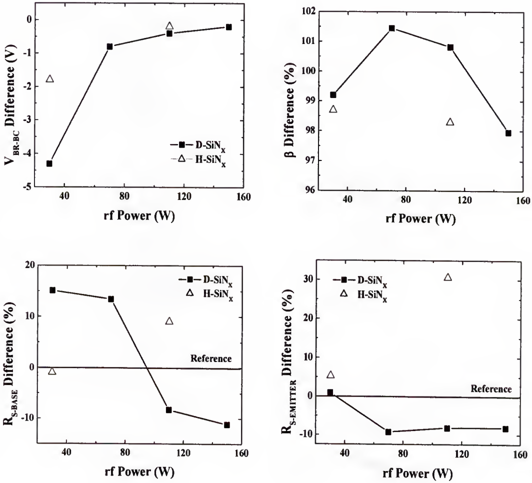

Figure 6-14. Changes in $V_{BR\text{-}BC}$, β, $R_{S\text{-}BASE}$ and $R_{S\text{-}EMITTER}$ from HBTs deposited with SiN_X at different rf powers.

The effects of SiD_4/ND_3 flow ratio on V_{BR} of the BC junction, β and the base and emitter sheet resistances are shown in Figure 6-15. Similar trends were observed as with the rf power in the sense that V_{BR} of the BC junction showed the largest changes and the other parameters showed variations of ≤10%.

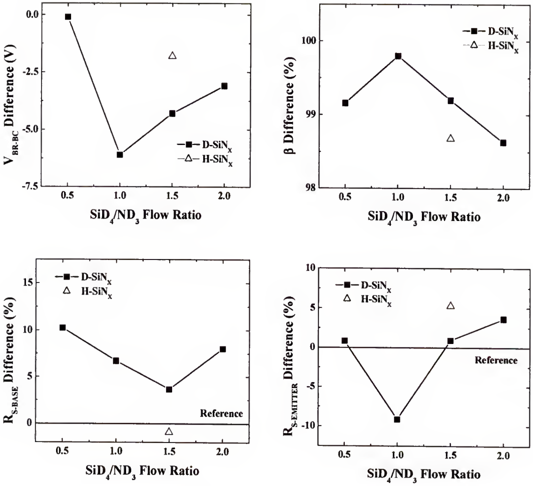

Figure 6-15. Changes in $V_{BR\text{-}BC}$, β, $R_{S\text{-}BASE}$ and $R_{S\text{-}EMITTER}$ from HBTs deposited with SiN_X at different SiD_4/ND_3 gas flow ratios.

Finally, Figure 6-16 shows the effect of deposition pressure on V_{BR} of the BC junction, β and sheet resistance of the base and emitter layers. The changes in gain and sheet resistance are again quite small (≤15%), with the biggest changes observed in breakdown voltage of the BC junction. The magnitude of the changes is typically slightly less with hydrogenated precursors relative to deuterated chemicals.

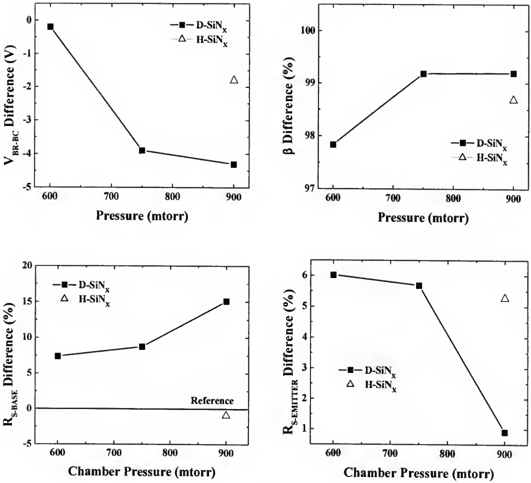

Figure 6-16. Changes in $V_{BR\text{-}BC}$, β, $R_{S\text{-}BASE}$ and $R_{S\text{-}EMITTER}$ from HBTs deposited with SiN_X at different process pressure.

There does not appear to be any significant advantage to use of deuterated precursors for the PECVD of SiN_X films on GaAs MESFETs or GaAs/AlGaAs HBTs. The changes in channel sheet resistance and drain-source current of MESFETs is typically ≤10%, while similar magnitude changes were observed in dc current gain and base and emitter sheet resistance of HBTs. The PECVD process produces minimal changes at higher pressure, lower powers and relatively low SiH_4/NH_3 flow ratios.

CHAPTER 7
PASSIVATION EFFECTS OF MBE-GROWTH OXIDES ON NITRIDE HEMT DEVICES

7.1 Gas Source Molecular Beam Epitaxy Grown Oxide

Sc_2O_3 growth was performed in a modified RIBER 2300 MBE equipped with a reflection high-energy electron diffraction (RHEED) system, as shown in Figure 7-1. Oxygen was supplied from a Wavemat MPDR 610 ECR plasma source (2.54 GHz) with 200 watts forward power at $1\text{x}10^{-4}$ Torr oxygen pressure. Sc element evaporated out from standard effusion cell operating at 1130°-1170°C and the substrate temperature was measured using a backside thermocouple that was calibrated using the melting points of InSb and GaSb. All temperatures reported are actual. Materials characterization was provided from RHEED, 5 crystal high resolution x-ray diffraction (HXRD), atomic force microscopy (AFM) and Auger electron spectroscopy (AES).

The Nitride HEMT sample preparation consisted of a UV-ozone exposure for 25 minutes then indium mounted to molybdenum blocks and loaded into the MBE. At room temperature the surface of the substrates was polycrystalline according to the RHEED patterns.

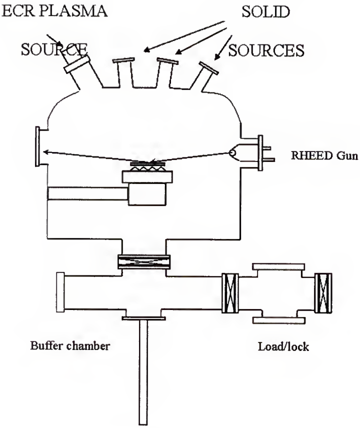

Figure 7-1. Illustration of Riber MBE used for oxide growth

From AFM and SEM results, MBE growth of Sc_2O_3 produced extremely smooth surface. RMS roughnesses of 0.5 to 0.8 nm were seen for substrate temperatures of 100°C to 600°C, respectively. The MOCVD GaN substrates have RMS roughnesses of 1.0 to 2.0 nm. Using AES depth profiling and surface scans, it was shown that the MBE derived Sc_2O_3 was of uniform concentration throughout the film, as shown in Figure 7-2. It was also found that the pretreatment of the GaN substrates removed the carbon contamination to levels below the Auger detection limits. The O:Sc ratio, as measured from comparing Auger peak to peak heights, was 0.85 to 0.90 for substrate temperatures of 600°C and 100°C respectively. This variation in O:Sc ratio is within the error of the AES detection limits. The O:Sc ratio did not change as a function of cell temperature. A

Sc_2O_3 standard was not available to compare against the thin film data. The growth rate of the scandium oxide was 0.67nm/min for T_{Sc}=1130°C and 1.25nm/min for T_{Sc}=1170°C. The growth rate did not appear to vary with changes in substrate temperature.

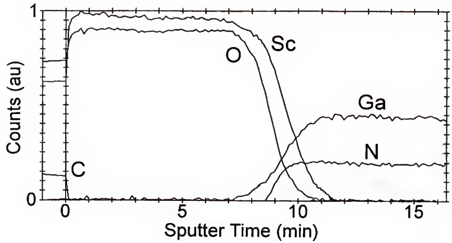

Figure 7-2. Auger Electron Spectroscopy(AES) depth profile of Sc_2O_3 on GaN. The conditions of the oxide growth were T_{Sc}=1130°C and T_{sub}= 100°C

7.2 Essentials of Surface Cleaning before Oxide Growth

7.2.1 Introduction

AlGaN/GaN high electron mobility transistors show excellent potential for high power, high efficiency microwave power amplifiers for military and wireless communication applications(253-257). One of the frequently reported problems is that the rf power obtained from GaN-based HEMTs is much lower than expected from the dc characteristics(209, 253-255). This is manifested by a significant frequency slump or collapse in drain current which severely reduces output power and power-added efficiency(76). The cause appears to be the presence of surface states between the gate and drain of the HEMT structure which deplete the channel in this region with time constants long enough to disrupt modulation the channel charge during large signal of operation(254).

The use of SiN_X passivation layers deposited by plasma-enhanced chemical vapor deposition has proven effective in reducing the effects of the surface states(209). However there have not been any long-term reliability studies demonstrating the stability of these layers. Typical PECVD SiN_X layers contain high concentrations of hydrogen which can migrate into GaN or into the gate metallization.

Two alternative passivation materials are MgO and Sc_2O_3, which are being investigated for use as gate dielectrics for GaN-based MOSFETs(259-261). These materials have the most attractive bandgaps and thermal and lattice properties for use on GaN. In this paper we report the effect of deposition of thin films of MgO and Sc_2O_3 on the dc and rf performance of AlGaN/GaN HEMTs. Both materials can reduce the reverse leakage current and increase f_T and f_{MAX} if the deposition conditions are optimized.

7.2.2 Experimental

The HEMT structures were grown by rf plasma-assisted Molecular Beam Exitaxy (MBE) on c-plane sapphire substrates. The layer structures and dc performance have been described in detail previously(209, 257). The oxide films were deposited at 100°C on the completed $1.2\times100\mu m^2$ HEMTs, using an rf plasma source (200W, 10^{-4} torr) for O_2 and e-beam evaporation of the Sc (at a source temperature of 1130°C) or Mg (at a source temperature of 380°C) within an MBE system. The deposition thickness was ~100Å in all cases and growth was initiated with both the O_2 plasma and metal evaporation. Several different variations of pretreatments (either heating to 300°C or UV-ozone treatment) were applied prior to the oxide deposition.

7.2.3 Results and Discussions

(a) MgO deposition

Figure 7-3 shows I_{DS}-V_{DS} (top left), transfer characteristics (top right), reverse I-V (bottom left) and gate I-V (bottom right) along with a table of equivalent circuit parameters derived from rf measurements of HEMTs deposited with 100Å of MgO. These include mutual transconductance, gate-source capacitance, drain-source resistance, drain-source capacitance, gate-drain capacitance, gate resistance, source resistance, drain resistance and transit time. The values for the control devices are shown in the top line of the table and the values after MgO deposition are shown in the bottom line. Note that the main change in the dc characteristics is a reduction in reverse leakage current. We expect this is due to an effective passivation of surface states that would otherwise contribute to leakage through generation-recombination processes.

Figure 7-4 shows similar results for a HEMT heated to 300°C for 5mins prior to cooling to 100°C for the MgO deposition. In this case the reverse leakage is slightly increased, without any significant change in other dc parameters. From the rf data, we observed increases in gate-source resistance, source resistance and drain resistance. We expect that at least part of these increases is due to thermal degradation of the gate contact.

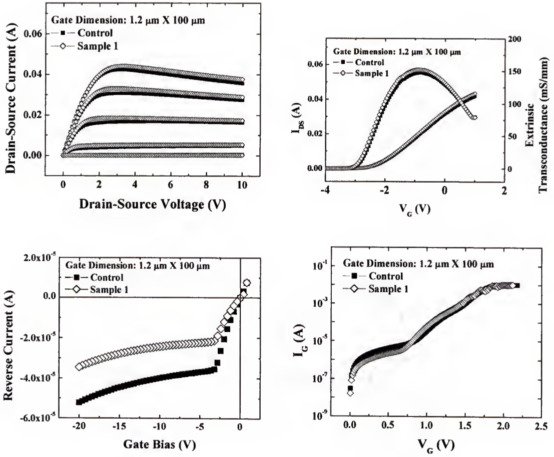

GM	CGS	RDS	CDS	CGD	RGS	RG	RS	RD	TAU
17.419	0.27328	869.58	0.00775	0.03884	1.5780	16.816	11.824	7.1143	0.5773
19.2137	0.28151	845.21	0.01548	0.03429	2.4069	13.926	13.986	12.492	0.5152

Figure 7-3. dc characteristics (I_{DS}-V_{DS}, I_{DS}, g_m-V_G, I_R-V_G, I_G-V_G) and tabulation of equivalent circuit parameters from rf measurements (bottom) before and after 100Å MgO deposition without any other ex-situ or in-situ treatments.

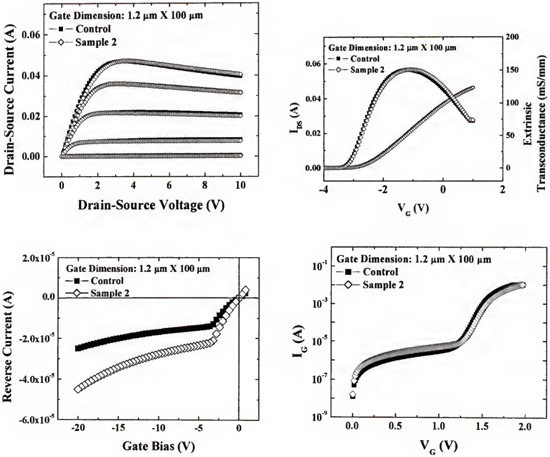

GM	CGS	RDS	CDS	CGD	RGS	RG	RS	RD	TAU
17.892	0.21182	783.63	0.01003	0.03311	1.6445	16.177	12.055	2.1557	0.3633
19.529	0.23339	614.07	0.01621	0.03148	2.6477	16.475	16.215	10.947	0.3411

Figure 7-4. dc characteristics and tabulation of equivalent circuit parameters from HEMTs heated to 300°C for 5mins and then deposited with 100Å of MgO at 100°C.

Similar results we observed for HEMTs treated in UV-ozone for 25mins, then heated to 300°C for 5mins prior to cooling to 100°C for the MgO deposition. The reverse leakage increased slightly, along with some of the equivalent resistances. The UV-ozone treatment by itself, with no MgO deposition also reduced the reverse leakage current, as shown in Figure 7-5. The expected result of this process is the removal of surface hydrocarbons and points to the critical need for effective surface cleaning of the GaN for optical device performance.

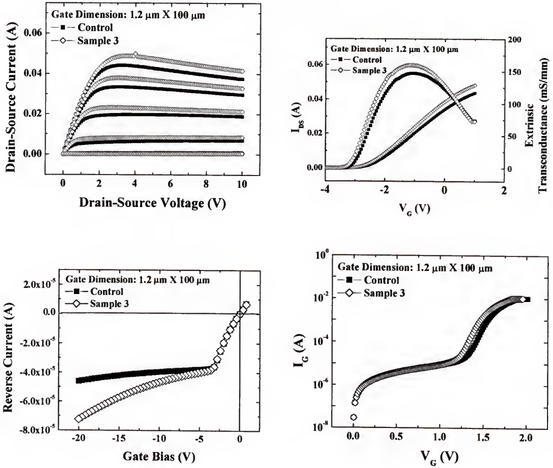

GM	CGS	RDS	CDS	CGD	RGS	RG	RS	RD	TAU
18.004	0.22420	865.08	0.01068	0.03379	1.2574	16.642	12.564	3.0270	0.4702
20.764	0.23622	930.33	0.01268	0.03200	1.9065	13.798	11.356	6.4969	0.3891

Figure 7-5. dc characteristics and tabulation of equivalent circuit parameters from HEMTs heated for 25mins with UV/O_3 at 25°C.

Figure 7-6 shows a compilation of rf and dc data from the MgO experiments. Condition 1 corresponds to MgO deposition with no ex-situ pretreatment or in-situ thermal treatment; Condition 2 corresponds to no ex-situ pretreatment, heating to 300°C for 5mins then cooling to 100°C for MgO deposition; Condition 3 corresponds to a 25min UV-ozone treatment, heating to 300°C for 5 mins then cooling to 100°C for MgO deposition; Condition 4 corresponds to a 25 min UV-ozone treatment only with no MgO deposition. Note that the MgO deposition without any other treatment consistently improves I_{DS}, g_m, f_T, and f_{MAX}.

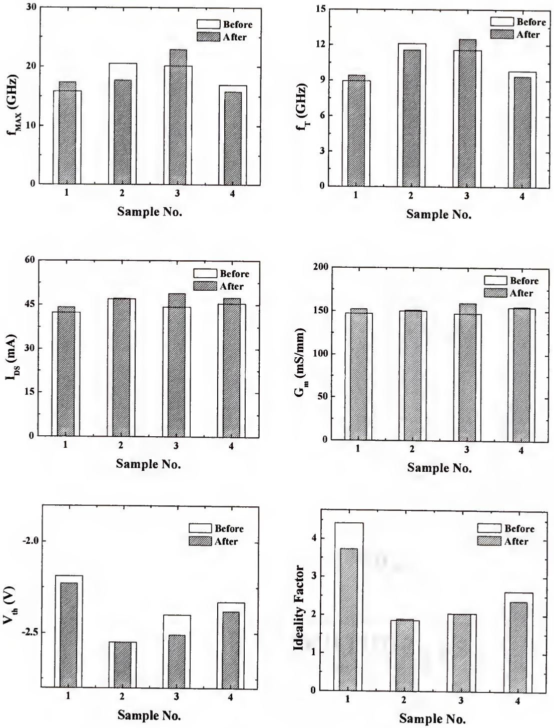

Figure 7-6. Tabulation of rf and dc results from HEMTs heated as follows: 1. MgO at 100°C; 2. heated to 300°C then MgO at 100°C; 3. 25mins UV/O_3, heated to 300°C then MgO at 100°C; 4. 25mins UV/O_3.

(b) Sc_2O_3 Deposition

Figure 7-7 shows the data for HEMTs deposited with 100Å of Sc_2O_3 at 100°C, with no other surface treatment. There is no significant change in any of the dc performance parameters, but the reverse leakage was decreased. Note that all of the equivalent circuit parameters obtained from the rf data do not show any change as a result of the Sc_2O_3 deposition.

The use of UV-ozone treatment for 25mins at 25°C prior to loading the HEMT into the MBE system, heating to 300°C for 5mins and depositing 100Å of Sc_2O_3 at 100°C produced a slight increase in peak g_m but an increase in reverse leakage current (Fig 7-8). This result was very similar to HEMTs that went through the same procedure but without the UV/O_3 treatment and suggests that this latter treatment does not impact the surface properties as much as the dielectric film itself.

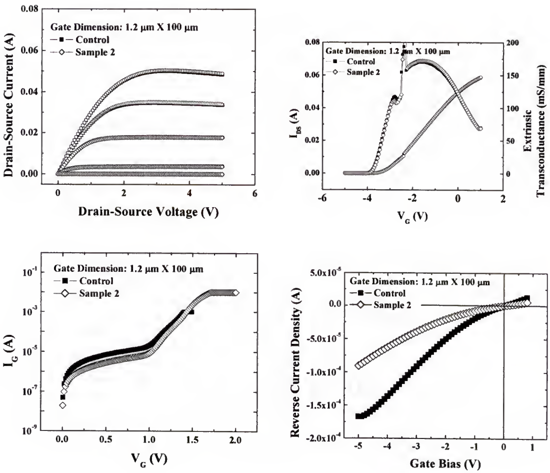

GM	CGS	RDS	CDS	CGD	RGS	RG	RS	RD	TAU
19.107	0.26057	682.40	0.00931	0.03369	4.7765	12.075	2.9945	5.2498	0.44459
18.946	0.24513	617.42	0.01023	0.03192	4.6793	11.763	4.2245	5.1650	0.39316

Figure 7-7. dc characteristics and tabulation of equivalent circuit parameters from HEMTs deposited with 100Å of Sc_2O_3 at 100°C without any other ex-situ or in-situ pretreatments.

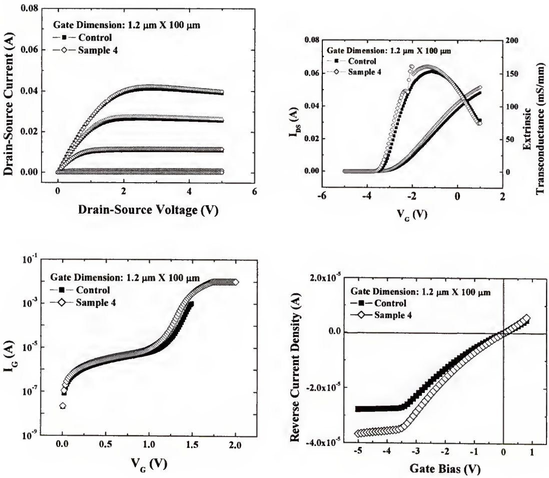

GM	CGS	RDS	CDS	CGD	RGS	RG	RS	RD	TAU
17.552	0.22728	720.23	0.00943	0.03656	13.505	12.179	3.3158	4.6427	0.41770
16.963	0.20026	755.48	0.01240	0.03496	13.355	11.840	2.3585	4.9487	0.38897

Figure 7-8. dc characteristics and tabulation of equivalent circuit parameters from HEMTs heated for 25mins with UV/O_3 at 25°C, heated to 300°C for 5mins and then deposited with 100Å of Sc_2O_3 at 100°C.

Figure 7-9 shows data from a HEMT heated for 25mins at 25°C in UV/O_3, dipped in BOE for 30secs then loaded in the MBE system, heated to 300°C and cooled to 100°C for the Sc_2O_3 deposition. Note the reduction in gate current, which may result from a reduction in effective channel doping caused by an increase in surface depletion. The reverse leakage was also decreased by the sequence of processes carried out on this set of devices.

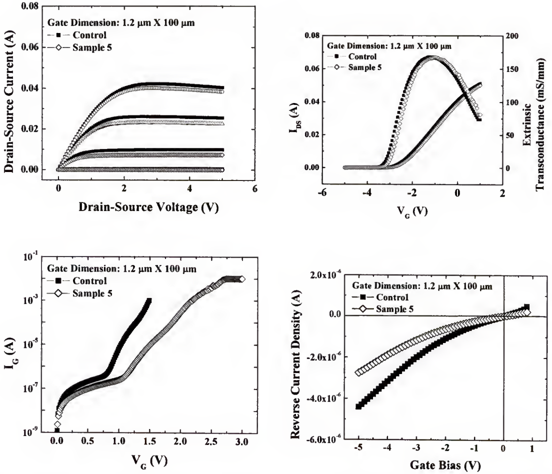

GM	CGS	RDS	CDS	CGD	RGS	RG	RS	RD	TAU
15.818	0.22432	516.42	0.00831	0.03806	12.086	12.048	1.0998	12.211	0.25461
11.291	0.17725	387.42	0.01096	0.02964	12.438	11.283	1.6594	7.4108	0.10557

Figure 7-9. dc characteristics and tabulation of equivalent circuit parameters from HEMTs heated for 25mins with UV/O_3 at 25°C, 30sec dip in BOE, heated to 300°C for 5mins and then deposited with 100Å of Sc_2O_3 at 100°C.

Figure 7-10 shows a summary of the rf and dc data from the HEMTs deposited with Sc_2O_3 with different pretreatments. There is no consistent improvement in dc characteristics, but some increases in both f_T and f_{MAX} for devices simply deposited with

Sc_2O_3 or treated with ozone, heated and then deposited with Sc_2O_3. A comparison of the data from MgO passivation shows that the latter was more effective in increasing I_{DS} which we suggest is due to an increase in positive charge at the MgO/GaN interface, resulting in an increase in effective sheet carrier concentration in the channel. This was accompanied by an increase in the small-signal transconductance and a change in threshold voltage, which are both consistent with an increase in effective channel doping. We have not yet performed large signal measurements, in which one would expect to observe large increases in saturated power and power-added efficiency if the passivation is truly effective.

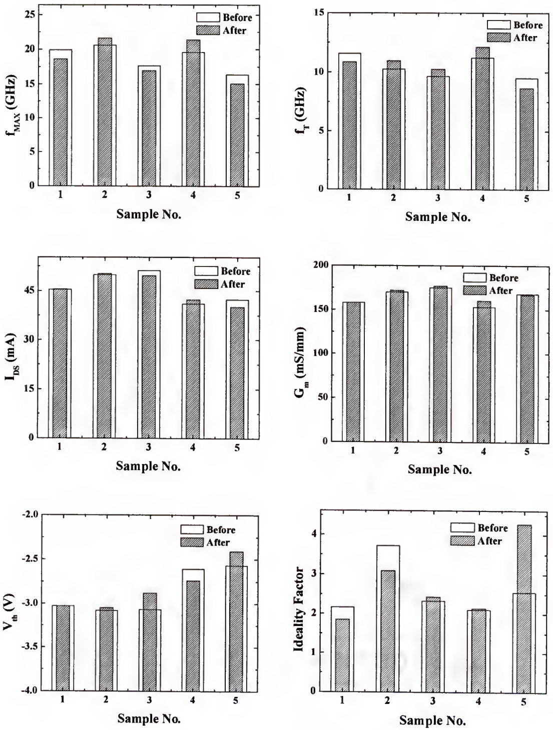

Figure 7-10. Tabulation of rf and dc results from HEMTs heated as follows: 1. heated to 300°C then held at 100°C; 2. Sc_2O_3 at 100°C; 3. heated to 300°C then Sc_2O_3 at 100°C; 4. 25mins UV/O_3, heated to 300°C then Sc_2O_3 at 100°C; 5. 25mins UV/O_3, 30sec dip in BOE, heated to 300°C then Sc_2O_3 at 100°C.

Two novel dielectrics, MgO and Sc_2O_3, were examined for passivation of AlGaN/GaN HEMTs. A variety of different pre-cleaning treatments were employed prior to the dielectric deposition. The MgO appeared more effective than Sc_2O_3 in increasing drain-source current through an increase in surface charge at the interface with the GaN. These dielectrics may have advantages over SiN_X in terms of long-term device stability.

7.3 Comparison of Surface Passivation Films for Reduction of Current Collapse in AlGaN/GaN HEMTs

Three different passivation layers (SiN_X, MgO and Sc_2O_3) were examined for their effectiveness in mitigating surface-state-induced current collapse in AlGaN/GaN high electron mobility transistors (HEMTs). The plasma-enhanced chemical vapor deposited SiN_X produced ~70-75% recovery of the drain-source current, independent of whether SIH_4/NH_3 or SiD_4/ND_3 plasma chemistries were employed. Both the Sc_2O_3 and MgO produced essentially complete recovery of the current in GaN-cap HEMT structures and ~80-90% recovery in AlGaN-cap structures. The Sc_2O_3 had superior long-term stability, with no change in HEMT behavior over 5 months aging.

7.2.3 Introduction

AlGaN/GaN high electron mobility transistors (HEMTs) show great promise for applications in which high speed and high temperature operation are required, such as high frequency wireless base stations and broad-band links, commercial and military radar and satellite communications(209-210, 253-256, 262-273). These devices appear capable of producing very high power densities (>12W•mm^{-1}), along with low noise figures (0.6dB at 10GHz) and high breakdown voltage. A number of recent reviews have appeared on this topic(274-277). The use of metal-oxide-semiconductor (MOS) or metal-insulator-semiconductor (MIS) gates for HEMTs produces a number of advantages over the more conventional Schottky metal gates, including lower leakage current and greater voltage swing(98, 260, 263, 272, 273). Amongst the materials employed for gate oxide/insulators are SiO_2(259, 260, 263, 284), $Gd(Ga_2O_3)$(259, 260, 273, 282), AlN(283), SiN_X(261, 278-281), MgO(261, 285) and Sc_2O_3(285). These materials can also be employed as surface passivation layers on HEMTs. One problem commonly observed in these devices is the so-called "current collapse" in which the application of a high drain-source voltage leads to a decrease of the drain current and increase in the knee voltage(76, 209, 254, 259-270). This phenomenon can also be observed by a current dispersion between dc and pulsed test conditions or a degraded rf output power. The cause is the presence of surface states on the cap layer or trapping centers in the resistive buffer underlying the active channel. The carriers in the 2-dimentional electron gas can be lost either to the surface or buffer traps(209, 254, 286-289). The former may be mitigated to a greater or lesser extent by use of appropriate surface passivation, most often SiN_X deposited by plasma-enhanced chemical vapor deposition (PECVD), while the latter is a function of the epitaxial growth conditions. In the situation in which surface states dominate the current collapse, the use of SiN_X passivation typically restores 70-80% of the "lost" current.

We have recently found promising results for two alternative candidates for HEMT passivation, namely Sc_2O_3 and MgO(132, 290). A comparison of the properties of these oxides with those of the other commonly used passivation materials on GaN is shown in Table 7-1. They have smaller lattice mismatch to GaN and larger bandgap than

Gd_2O_3. In addition, they do not contain hydrogen and may have advantages over SiN_X in that respect because atomic hydrogen diffuses rapidly and could enter the GaN or gate metal over extended periods of device operation.

Table 7-1: Material properties for GaN and various dielectrics. W = Wurtzite, A = amorphous, B = Bixbyite, N = NaCl.

	GaN	**SiO_2**	**SiN_x**	**AlN**	**GGG**	**Gd_2O_3**	**Sc_2O_3**	**MgO**
Structure	W	A	A	W or A	A	B	B	N
Lattice Constant	3.186	-	-	3.113		10.813	9.845	4.2112
Atomic Spacing in the (111) plane		-	-	-	-	3.828	3.4807	2.978
Mismatch to GaN (%)	-	-	-	2.3	-	20.1	9.2	-6.5
T_{MP} (K)	2800	1900	2173	3500	2023	2668	2678	3073
Bandgap (eV)	3.4	9	5	6.2	4.7	5.3	6.3	8
Electron Affinity (eV)	3.4	0.9		0 – 2.9		0.63		0.7
Work Function (eV)				0.9 – 1.2		2.1 – 3.3	4	3.1 – 4.4
Dielectric Constant	9.5	3.9	7.5	8.5	14.2	11.4	14	9.8

In this paper we report on a comparison of SiN_X, MgO and Sc_2O_3 passivation layers on AlGaN/GaN HEMTs with different layer structures (GaN vs AlGaN cap layer) and show the long-term (5 month) stability of the MgO and Sc_2O_3 passivation. We find essentially complete mitigation of the drain current collapse in GaN-capped HEMTs passivated with MgO or Sc_2O_3, compared to 70-75% recovery with SiN_X. For AlGaN-capped HEMTs, the MgO and Sc_2O_3 is effective in restoring ~80-90% of the drain current.

7.2.2 Experimental

Two different HEMT structures were used in these experiments. The first employed a GaN undoped cap layer on left of an undoped $Al_{0.2}Ga_{0.8}N$ layer. Both Al_2O_3

and SiC substrates were used. The doping in this structure is basically due to piezo-induced carriers. The second type of HEMT employed an undoped $Al_{0.3}Ga_{0.7}N$ cap layer on top of a doped $Al_{0.3}Ga_{0.7}N$ donor layer. The doping in this structure is due to the intentional Si-doping of the donor layer. The ohmic (Ti/Al/Pt/Au) and gate (Ni/Au) contacts were deposited by e-beam evaporation and patterned by lift-off. Schematics of the completed device structures are shown in Figure 7-11.

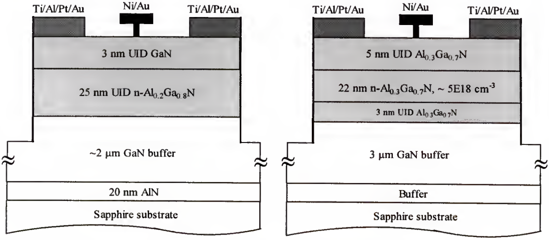

Figure 7-11. Schematic cross-sections of GaN-cap (left) and AlGaN-cap (right) HEMT structures.

The 100Å thick MgO, Sc_2O_3 or SiN_X layers were deposited on completed devices (0.25-1.2μm gate length, 100μm gate width) using either Molecular Beam Epitaxy (MBE) for the oxides or PECVD for the SiN_X, with deposition temperatures of 100°C in the oxide case and 250°C for the SiN_X case. Details of the oxide deposition have been given previously(132, 290). The SiN_X films were deposited with either $SiH_4 + NH_3$ or $SiD_4 + ND_3$ to examine the effect of deuterated precursors.

The HEMT dc parameters were measured in dc and pulsed mode at 25°C, using a parameter analyzer for the dc measurements and pulse generator, dc power supply and oscilloscope for the pulsed measurements. For the gate lag measurements, the gate voltage V_G was pulsed from –5V to 0V at different frequencies with a 10% duty cycle.

7.3.3 Results and Discussion

(a) Unpassivated Devices

Figure 2(left) shows typical gate lag data for $0.5\times100\mu m^2$ GaN-cap HEMT grown on sapphire substrates. The decrease in drain-source current becomes more pronounced at high measurement frequencies. The degradation in current was less significant when these same structures were grown on SiC substrates, as shown in Figure 7-12 (right). The defect density will be lower in the latter case due to the closer lattice match between GaN and SiC and this appears to affect the resultant surface state density. This suggests that at least some of the surface traps are related to dislocations threading to the surface.

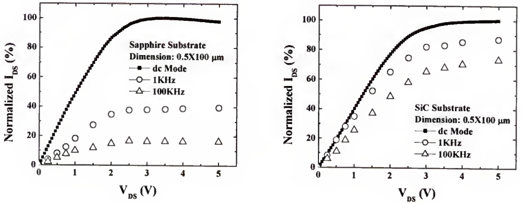

Figure 7-12. Gate lag measurements on unpassivated 0.5μm gate length, GaN-cap HEMTs grown on either sapphire (left) or SiC (right) substrates.

The effects of both substrate type and HEMT gate length on the change in drain-source current are shown in Figure 7-13. The shorter the gate length, the more pronounced the degradation in current because of larger surface area and higher electric field in the channel between source,S and drain,D (the S-D distance was fixed in all cases).

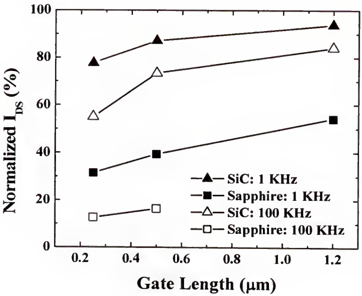

Figure 7-13. Normalized I_{DS} as a function of both gate length and substrate type for GaN-cap HEMTs at pulse frequency of 1KHz and 100KHz.

(b) SiN_X Passivation

Figure 7-14 (left) shows the I_{DS}-V_{DS} characteristics before and after SiN_X passivation using either hydrogenated or deuterated precursors. The inset shows the complete set of curves for the as-fabricated HEMT and the main figure shows only the uppermost curves for clarity. The I_{DS} increases after passivation with either type of SiN_X, which indicates that the surface state density is decreased(260). Similarly, the transconductance (g_m) increases after SiN_X deposition, which also suggests a decrease in surface trap density (Figure 7-14, right)(260).

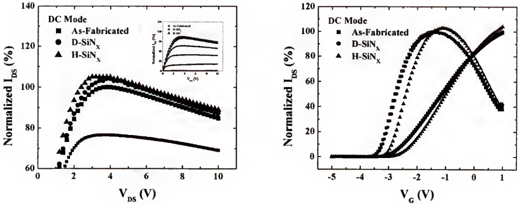

Figure 7-14. Normalized I_{DS} versus V_{DS} (left) or V_G (right) for 1.2×100μm^2, GaN-cap HEMTs before and after SiN_X passivation using either hydrogenated or deuterated precursors.

The gate lag data is shown in Figure 7-15(left) for the HEMTs before and after SiN_X passivation. Note that both the hydrogenated and deuterated precursor dielectric produces a recovery of 70-75% in the drain-source current. This range represents results obtained from five different devices with each type of dielectric. The unity current gain frequency (f_T) and maximum frequency of oscillation (f_{MAX}) data before and after passivation are shown at the right of Figure 7-15. Note that there is actually a slight increase in both parameters, in contrast to previous reports(260). There were no systematic differences between the results for hydrogenated and deuterated precursor SiN_X, even though the latter typically produce slightly denser films when deposited under the same PECVD conditions.

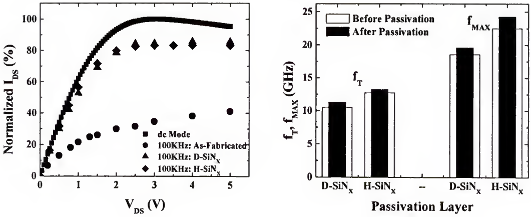

Figure 7-15. Gate lag measurements before and after SiN_X passivation of 1.2×100μm^2, GaN-cap HEMTs (left) and f_T and f_{MAX} before and after SiN_X passivation (right).

There was also an increase in forward and reverse gate currents after passivation with SiN_X, as shown in the I-V characteristics in Figure 7-16. These results are also consistent with a decrease in surface depletion and decrease in surface trap density and indicate that there is no major degradation to the dc performance of the HEMTs upon addition of the SiN_X layer. We believe the increase in gate leakage is not from the passivation itself, but may originate from degradation of the gate metallization during the oxide desorption step at 350°C.

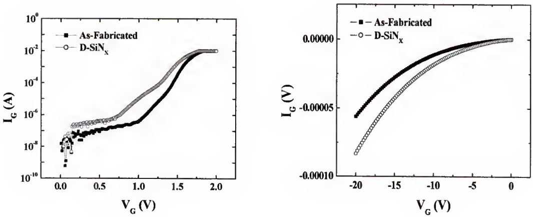

Figure 7-16. Forward (left) and reverse (right) I_G-V_G characteristics from 1.2×100μm^2, GaN-cap HEMTs before and after SiN_X passivation with deuterated precursors.

(c) MgO and Sc_2O_3 Passivation of GaN-cap HEMTs

Figure 7-17 shows the gate lag data for GaN-cap 0.5×100μm^2 HEMTs. In the case at left, V_G was pulsed from –5 to 0V at 0.1MHz with a 10% duty cycle and this pulsed data is compared to that from dc measurements. The right of Figure 7-17 shows the normalized I_{DS} for gate voltage switched from –5V with V_{DS} held constant at 3V to avoid any self-heating effects. This data establishes the base-line for measuring the effectiveness of the MgO and Sc_2O_3 passivation. As reported previously(286), these HEMTs showed an increase in drain-source current of ~20% after deposition of either type of oxide. In addition, the forward and reverse gate currents were slightly increased (Figure 7-18 shows an example for an MgO-passivated HEMT).These results are similar to those for SiN_X deposition.Once again,the increased reverse current may be due to gate metal degradation.

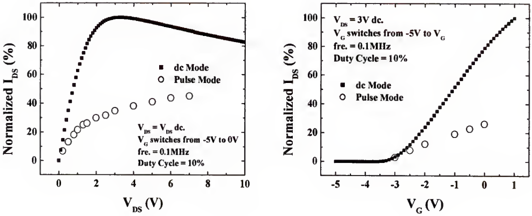

Figure 7-17. Gate lag measurements on unpassivated GaN-cap HEMTs (1.2×100µm^2 gate). At left V_G was switched from –5 to 0V, while at right it was switched from –5V to the value shown on the X-axis.

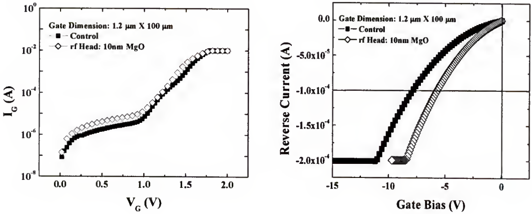

Figure 7-18. Forward (left) and reverse (right) I_G-V_G characteristics from 1.2×100µm^2, GaN-cap HEMTs before and after MgO passivation.

Figure 7-19 shows gate lag measurement for MgO-passivated HEMTs immediately after MgO deposition and after 5 months aging without bias on the devices under room conditions (temperature and humidity). The I_{DS} increases ~20% upon passivation, as mentioned earlier and there is almost complete mitigation of the degradation in I_{DS} immediately after MgO deposition. However after 5 months aging, there is a clear difference between the dc and pulsed data, indicating that the MgO passivation has lost some of its effectiveness. We are currently investigating possible mechanisms such as oxidation of the GaN surface through pinholes in the MgO, or reaction between the MgO and GaN.

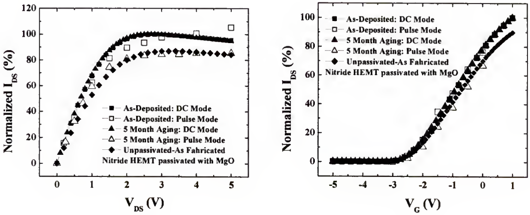

Figure 7-19. Gate lag measurements before and after MgO passivation and following 5 months aging of $1.2 \times 100\mu m^2$, GaN-cap HEMTs. At left V_G was switched from –5 to 0V, while at right it was switched from –5V to the value shown on the X-axis.

Similar data is shown in Figure 7-20 for Sc_2O_3-passivated HEMTs. In this data the I_{DS} also increases upon deposition of the oxide and there is also essentially complete mitigation of the degradation in drain-source current. However the major difference is that these is no significant change in these characteristics after 5 months aging. This indicates that Sc_2O_3 provides more stable passivation than MgO. We have noticed in separate experiments that the MgO/GaN interface deteriorates over time if left uncapped, i.e. we see increases in interface state trap density in MOS diodes on which the metal is deposited a long period after the MgO was deposited on the GaN. However, if the MgO is immediately covered by the gate metal, these changes are not observed. In a real manufacturing process, the MgO-passivated HEMTs would be covered with a dielectric such as SiN_X to provide mechanical protection and therefore MgO should not be disqualified as a candidate to provide effective passivation of GaN/AlGaN HEMTs. Obviously, further work is needed to establish the reliability of Sc_2O_3 and MgO passivation on these devices, but the preliminary data with Sc_2O_3 looks very promising.

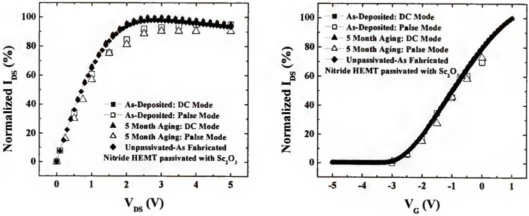

Figure 7-20. Gate lag measurements before and after Sc_2O_3 passivation and following 5 months aging of $1.2\times100\mu m^2$, GaN-cap HEMTs. At left V_G was switched from –5 to 0V, while at right it was switched from –5V to the value shown on the X-axis.

(d) MgO and Sc_2O_3 passivation of AlGaN-cap HEMTs

Figure 7-21 shows the gate lag data for the HEMT structures of Figure 1(right), i.e. the structures with $Al_{0.3}Ga_{0.7}N$ as the top layer. As with the GaN-cap devices, there is a very significant degradation of drain-source current under pulsed conditions where the surface traps cannot completely empty.

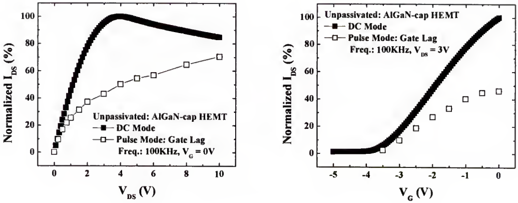

Figure 7-21. Gate lag measurements on unpassivated 0.5µm gate length, AlGaN-cap HEMTs. At left V_G was switched from –5 to 0V, while at right it was switched from –5V to the value shown on the X-axis.

The effectiveness of the MgO and Sc_2O_3 passivation was more variable on the AlGaN-cap devices than for the GaN-capped HEMTs described in the previous section. Figure 7-22 shows typical gate-lag data from a Sc_2O_3 passivated AlGaN-cap HEMT. We found that the Sc_2O_3 deposition was typically able to restore 80-90% of the drain current loss relative to dc measurement conditions. Some devices showed essentially complete restoration of the current, but the 80-90% range was more typical. Similar results were obtained for MgO passivation, as shown in Figure 7-23. Once again, some individual HEMTs showed essentially full restoration of I_{DS} upon MgO deposition, but a more typical result was that shown in Figure 7-23, with 80-90% effectiveness. We believe that our in-situ cleaning procedure prior to deposition of these oxides in the MBE chamber is not able to completely remove the native oxide from the AlGaN surface. This limits the effectiveness of the resulting passivation and accounts for the more variable results we observe for the AlGaN-cap devices.

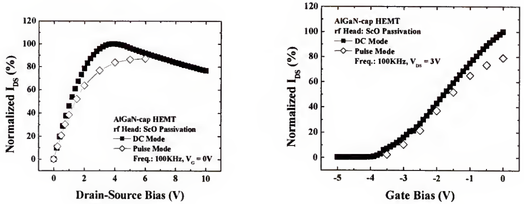

Figure 7-22. Gate lag measurements before and after Sc_2O_3 passivation of $0.5\times100\mu m^2$, AlGaN-cap HEMTs. At left V_G was switched from –5 to 0V, while at right it was switched from –5V to the value shown on the X-axis.

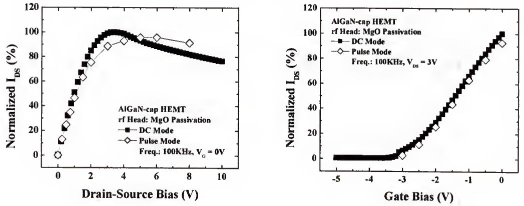

Figure 7-23. Gate lag measurements before and after MgO passivation of $0.5\times100\mu m^2$, AlGaN-cap HEMTs. At left V_G was switched from –5 to 0V, while at right it was switched from –5V to the value shown on the X-axis.

MgO and Sc_2O_3 thin films deposited by MBE appear very promising as surface passivation layers on AlGaN/GaN HEMTs. In our structures with a GaN-cap layer they provide more effective mitigation of drain current collapse than the conventional PECVD SiN_X films. The Sc_2O_3 provides stable passivation characteristics over a period of at least

5 months, while the MgO was found to lose some of its effectiveness under the same conditions. The passivation with both oxides is more variable on AlGaN-cap structures, which we believe is due to the greater difficulties in removing the native oxide from the AlGaN surface prior to deposition of the passivation films. With respect to SiN_X passivation, we found no obvious advantage to the use of deuterated precursors for the deposition. Finally, it showed be noted that both MgO and Sc_2O_3 can also be used as gate dielectrics on GaN to provide MOS diodes and transistors and thus an MBE system equipped for their deposition can provide both the gate oxide and the device passivation in a manufacturing environment.

7.4 Role of Cleaning Conditions and Epitaxial Layer Structure on Reliability of Sc_2O_3 and MgO Passivation on AlGaN/GaN HEMTs

The effect of layer structure (GaN versus AlGaN cap) and cleaning procedure prior to Sc_2O_3 or MgO deposition at 100^0 C were examined for their effects on the long-term bias-stress stability of AlGaN/GaN HEMTs. Surface cleaning by itself was not sufficient to prevent current collapse in the devices. The forward and reverse gate leakage currents were decreased under most conditions upon deposition of the oxide passivation layers. After approximately 13 hours of bias-stressing, the MgO-passivated HEMTs retain $\geq 90\%$ their initial drain-source current. The Sc_2O_3-passivated devices retained ~ 80% recovery of the current under the same conditions.

7.4.1 Introduction

Remarkable progress have been made in recent times in developing insulator-GaN heterostructures with a low density of interfacial states(291). This has led to the recent demonstration of inversion behavior in MgO/p-GaN gated devices(292), which is a critical first step towards development of enhancement-mode GaN MOSFETs. Both MgO and Sc_2O_3 have been found to have a low interfacial state density ($\leq 3\times10^{11}$ $cm^{-2}eV^{-1}$ at 25°C) on GaN when deposited under Molecular Beam Epitaxy (MBE) conditions(251, 293). These materials may also be employed as surface passivation layers on AlGaN/GaN high electron mobility transistors(HEMTs) in order to reduce the effects of current degradation and transconductance dispersion that result from surface traps between the gate and drain region of the device(132, 290). The oxides are found to provide more effective passivation than other reported films used for the same purpose, such as SiN_X(267, 294-296). The absence of hydrogen in the oxides also makes them attractive candidates for long-term stable passivation of the HEMTs. While some initial results have shown excellent long-term stability (>5 months for Sc_2O_3 in AlGaN/GaN HEMTs) under un-biased conditions, there is a need to investigate the reliability under bias-stress testing conditions.

In this paper, we report on some initial experiments on Sc_2O_3 and MgO passivation of HEMTs after biasing for periods up to ~ 13 hours. The critical issues for achieving acceptable stability of the passivation are reported.

7.4.2 Experimental

Several different effects were investigated in this work. The first was the epitaxial layer. Two different HEMT structures were used in these experiments. The first employed a GaN undoped cap layer on top of an undoped $Al_{0.2}Ga_{0.8}N$ layer. Both SiC and Al_2O_3 substrates were used, but these did not any effect on the passivation results, which suggests that the surface is the dominant factor and not buffer-layer traps. The doping in this structure is basically due to piezo-induced carriers. The second type of HEMT employed an undoped $Al_{0.3}Ga_{0.7}N$ cap layer on top of a doped $Al_{0.3}Ga_{0.7}N$ donor layer. The doping in this structure is due to the intentional Si-doping of the donor layer. The ohmic (Ti/Al/Pt/Au) and gate (Ni/Au) contacts were deposited by e-beam evaporation and patterned by lift-off.

The 100Å thick MgO, Sc_2O_3 or SiN_X layers were deposited on completed devices (0.25-1.2μm gate length, 100μm gate width) using Molecular Beam Epitaxy (MBE) for the oxides with a deposition temperature of 100°C. The devices were heated in vacuum at 300~350°C prior to oxide deposition. Details of the oxide deposition have been given previously(132, 290). In addition, we investigated the effects of surface cleaning only, without oxide deposition. In this case, the HEMTs were exposed to UV/Ozone, followed by heating to 200°C(290).

The HEMT dc parameters were measured in dc and pulsed mode at 25°C, using a parameter analyzer for the dc measurements and pulse generator, dc power supply and oscilloscope for the pulsed measurements. For the gate lag measurements, the gate voltage V_G was pulsed from –5V to 0V at a frequency of 100 KHz with a 10% duty cycle.

7.4.3 Results and Discussion

(a) Surface Cleaning

First we discuss devices which were cleaned with the ozone/heating process and did not have any oxide passivation. The AlGaN-cap HEMTs showed little change in their dc characteristics with the exception of a decrease in gate leakage (Fig 7-24) during almost 10 hours of bias-stress at $V_G = 1V$, $V_{DS} = 8V$. Figure 7-25 shows the gate lag measurements before and after stressing for 572 minutes. There is no further degradation of the drain-source current over this period.

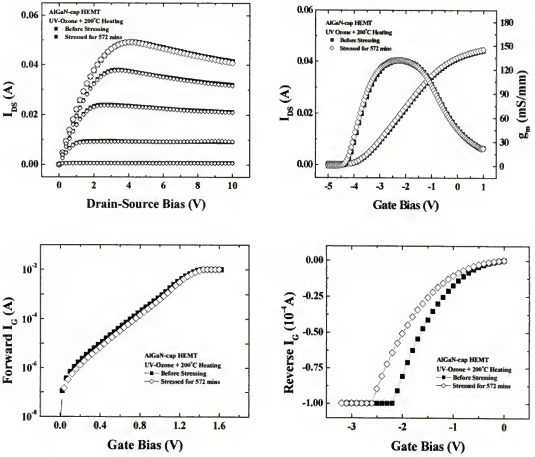

Figure 7-24. dc characteristics of AlGaN-cap HEMT cleaned with UV/Ozone and subsequent heating at 200°C. The characteristics are shown before and after bias-stressing for 572 mins.

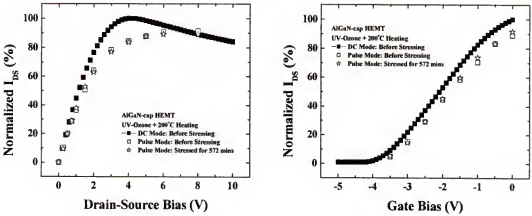

Figure 7-25. Gate lag measurements of AlGaN-cap HEMTs cleaned with UV/Ozone and subsequent heating at 200°C. The data is shown before and after bias-stressing for 572 mins.

Somewhat different results were obtained for the GaN-cap HEMTs. Figure 7-26 shows the dc characteristics before and after bias-stressing. In this case the gate currents were increased, which may be more of an issue related to degradation of the metal-semiconductor interface than surface-related. In these devices, the gate-lag measurements showed a continued deterioration of the current collapse with bias-stressing time (Figure 7-27). These results indicate that surface cleaning alone is not sufficient to prevent the current collapse phenomenon, or equivalently, that the nitride semiconductor surface is not adequately passivated.

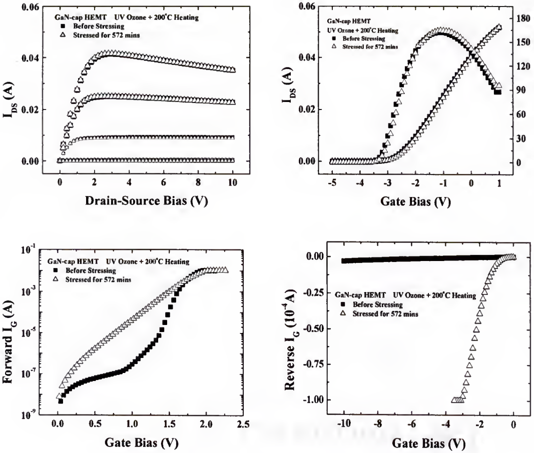

Figure 7-26. dc characteristics of GaN-cap HEMT cleaned with UV/Ozone and subsequent heating at 200°C. The characteristics are shown before and after bias-stressing for 572 mins.

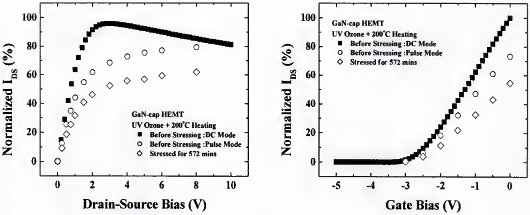

Figure 7-27. Gate lag measurements of GaN-cap HEMTs cleaned with UV/Ozone and subsequent heating at 200°C. The data is shown before and after bias-stressing for 572 mins.

(b) Effect of Vacuum Anneal Temperature Prior to Oxide Deposition

Figure 7-28 shows the dc characteristics from an AlGaN-cap HEMT cleaned in-situ by heating to 350°C prior to deposition of MgO at 100°C. The only significant change is once again a decrease in reverse gate leakage.

The major difference observed with these oxide-passivated devices is shown in Figure 7-29, where the gate lag data shows essentially complete mitigation of the current collapse, both before and after bias-stressing for approximately 758 minutes. It is clear that the MgO passivation is stable under bias for at least this period. We observed similar results for HEMTs passivated with a bi-layer of MgO/Sc_2O_3 .We have previously observed that unprotected MgO may degrade over a long period by reaction with water vapor. However, when it is encapsulated with another film, it is stable.

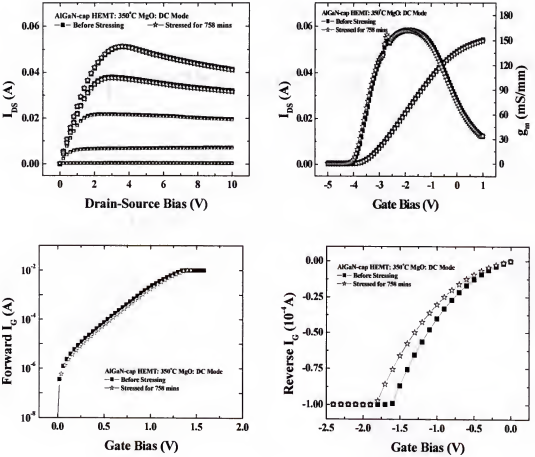

Figure 7-28. dc characteristics of AlGaN-cap HEMT heated to 350°C prior to MgO deposition. The characteristics are shown before and after bias-stressing for 758 mins.

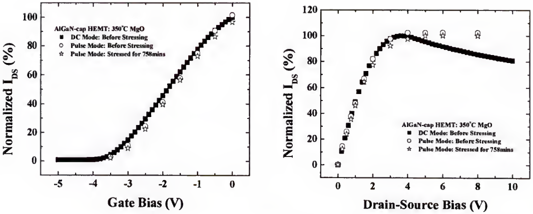

Figure 29. Gate lag measurements of AlGaN-cap HEMTs heated to 350°C prior to MgO deposition. The characteristics are shown before and after bias-stressing for 758 mins.

Similar results are shown in Figure 7-30 for GaN-cap HEMTs heated at 350°C prior to MgO deposition. In these devices there is a slight (a few percent) decrease in drain-source current over 758 minutes of bias-stressing and similar changes were observed for 300°C pre-cleaning. We believe that incomplete surface cleaning is responsible for these changes, since 700°C would be the ideal temperature for oxide deposition but this is not compatible with the existing metallization in use on the HEMTs.

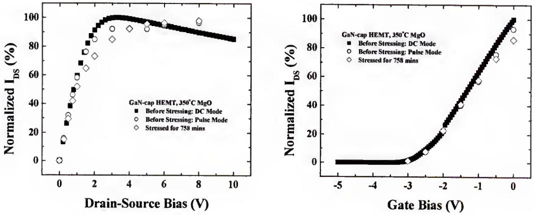

Figure 7-30. Gate lag measurements of GaN-cap HEMTs heated to 350°C prior to MgO deposition. The characteristics are shown before and after bias-stressing for 758 mins.

For Sc_2O_3 passivation, we also observed degradation of the drain-source current under pulsed conditions as a result of the bias-stressing cycle, as shown in Figure 7-31 for 350°C pre-cleaning and Figure 7-32 for 300°C pre-cleaning. Future work will focus on the differences between MgO and Sc_2O_3 in terms of both electrical and mechanical stability during long-term bias-stressing under ambient conditions.

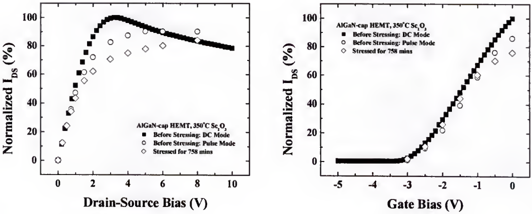

Figure 7-31. Gate lag measurements of AlGaN-cap HEMTs heated to 350°C prior to Sc_2O_3 deposition. The characteristics are shown before and after bias-stressing for 758 mins.

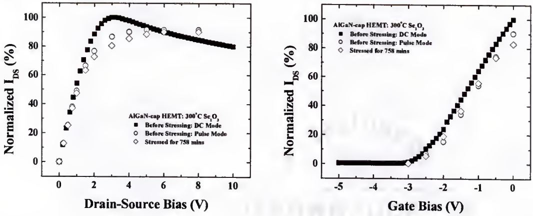

Figure 7-32. Gate lag measurements of AlGaN-cap HEMTs heated to 350°C prior to Sc_2O_3 deposition. The characteristics are shown before and after bias-stressing for 758 mins.

Excellent stability of HEMT passivation was obtained during bias-stressing (up to ~ 13 hours) of both AlGaN- and GaN-cap devices with MgO passivation. Small changes (a few percent) in drain-source current were observed for Sc_2O_3-passivated devices under the same conditions. A bi-layer of MgO/Sc_2O_3 prevented deterioration of the MgO through reaction with water vapor in the ambient.

7.5 Shielding Effects of Dielectric Films on Radiated Nitride HEMTs

AlGaN/GaN High Electron Mobility Transistors (HEMTs) with either MgO or Sc_2O_3 surface passivation were irradiated with 40 MeV protons at a dose of 5×10^9 cm^{-2}. While both forward and reverse bias current were decreased in the devices as a result of decreases in channel doping and introduction of generation-recombination centers, there was no significant change observed in gate lag measurements. By sharp contrast, unpassivated devices showed significant decreases in drain current under pulsed conditions for the same proton dose. These results show the effectiveness of the oxide passivation in mitigating the effects of surface states present in the as-grown structures and also of surface traps created by the proton irradiation

7.5.1 Introduction

MgO and Sc_2O_3 thin films deposited by Molecular Beam Epitaxy have shown great promise for surface passivation of AlGaN/GaN High Electron Mobility Transistors (HEMTs) and as gate dielectrics in metal-oxide semiconductor HEMTs (MOS-HEMTs)(71, 235, 237, 242-246). Two of the highest remaining obstacles to commercialization of AlGaN/GaN HEMTs are the current degradation and transconductance dispersion resulting from creation by surface states of a virtual gate in the gate-drain region(76, 209, 221, (265, 294, 295, 301-303) and of the high gate leakage alleviated temperatures of conventional metal-gate HEMTs(267, 278, 304-307). The recent advances in use of various oxides and dielectrics for surface passivation and as gate dielectrics have gone a long way forwards solving these problems, although issues of reliability and manufacturability remain to be proven.

Some of the applications for AlGaN/GaN HEMTs would be satellite communication systems for broad-band data transmission and weather forecasting. For these applications, it is necessary to measure the response of the devices to the type of high energy proton and gamma ray fluxes encountered in low-earth orbit(308-311). In this paper we report on the properties of AlGaN/GaN HEMTs with MgO or Sc_2O_3 passivation, after irradiation with 40MeV proton at a dose equivalent to approximately 10 years in low-earth orbit. Both GaN-cap and AlGaN-cap devices were investigated. The oxide passivation remains effective even after proton irradiation.

7.5.2 Experimental

Figure 7-33 shows the two types of HEMTs employed in this work. The processing and growth conditions for the structures has been described in detail previously(132, 133, 290). The 100Å thick MgO and Sc_2O_3 layers were deposited on completed $1.2\times100\mu m^2$ HEMT, using O_2 plasma-assisted MBE, as also described previously(132, 133, 285, 290). The HEMT dc characteristics were measured in both dc and pulsed mode using a HP 4145B parameter analyzer or pulse generator, dc power supply and oscilloscope, respectively. The devices were measured before and after irradiation with 40MeV protons at a fluence of 5×10^9 cm^{-2} in the Texas A&M cyclotron.

Measurements were taken ~50 hours after irradiation. The proton fluence corresponds to at least 10 years exposure in low-earth orbit.

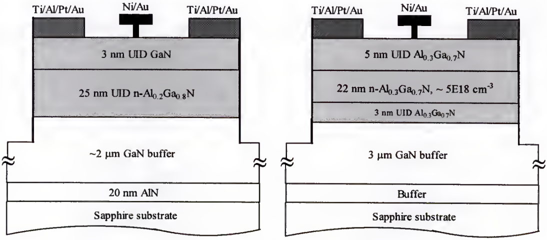

Figure 7-33. Schematics of GaN-cap(left) and AlGaN-cap(right) HEMT structures.

7.5.3 Results and Discussion

(a) GaN-cap HEMTs

Figure 7-34 shows the I_{DS}-V_{DS} characteristics(top left), transfer characteristics(top right), and forward (bottom left) and reverse (bottom right) I-V characteristics from an MgO passivated, GaN-cap HEMT before and after proton irradiation. As reported previously for unpassivated HEMTs(132), the changes in I_{DS} and gm are very small for these dose conditions. The diode ideality factor and barrier height were unchanged as a result of the irradiation, while the reverse breakdown voltage increased. This is consistent with removal of conduction electrons by the creation of deep trap states by the protons traversing the AlGaN/GaN layer. Each increasing proton is estimated to create ~50 stable traps(132). The presence of the MgO passivation did not have any measurable effect on the changes in HEMT dc characteristics observed after proton irradiation when we compared the results to unpassivated devices irradiated under the same conditions.

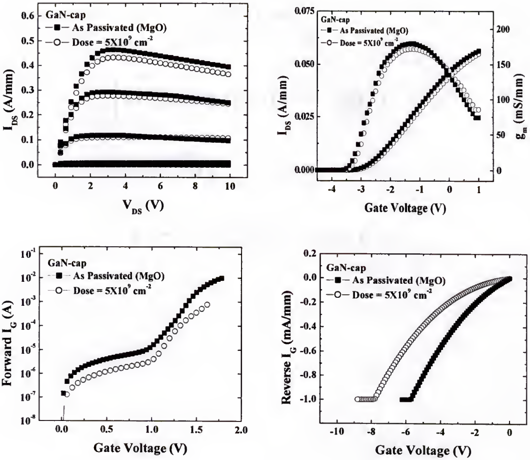

Figure 7-34. dc characteristics of MgO passivated, GaN-cap HEMTs before and after proton irradiation.

We have previously employed gate lag measurements as an indication for establishing the effectiveness of oxide passivation of HEMTs$^{(132)}$. Figure 7-35 shows the I_{DS} as a function of V_{DS} for pulsed measurements reported previously, there is essentially complete mitigation of the current collapse by employing MgO passivation and for clarity sake, we do not show the dc result since it is coincident with the pulsed result. In this data, V_G was pulsed from -5 to 0V at 0.1MHz with a 10% duty cycle. The right of Figure 7-35 shows the I_{DS} when the gate voltage is switched from -5 to 0V with V_{DS} held constant at 3V to avoid complication from device heating. These was essentially no change as a result of the proton irradiation, which indicates that the MgO is not degraded by the dose conditions employed and that it does not lose its effectiveness as a passivant of surface states on the HEMT structure.

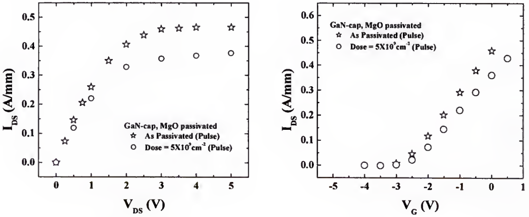

Figure 7-35. Gate lag measurements of MgO passivated GaN-cap HEMT. At left, V_G is switched from -5V to 0V, while at right it is switched from -5V to the value shown in the X-asix.

Similar results were achieved with Sc_2O_3 passivation layers. Figure 7-36 shows the dc characteristics from the GaN-cap HEMT before and after proton irradiation. The major change in the characteristics is once again in the reverse breakdown, which increases due to a reduction in the channel doping level.

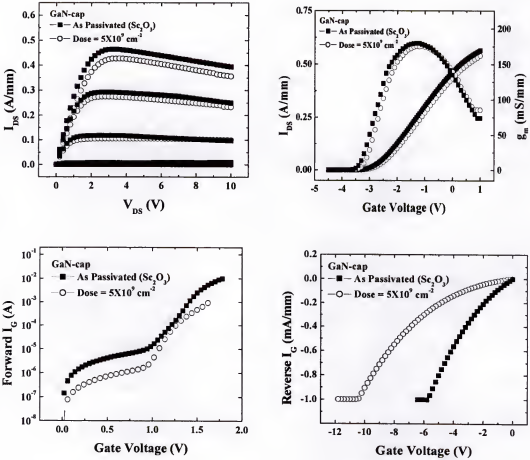

Figure 7-36. dc characteristics of Sc_2O_3 passivated, GaN-cap HEMTs before and after proton irradiation.

Figure 7-37 shows the results of the gate lag measurements. Once again there is no significant change in the behavior of the HEMT as a result of the proton irradiation, which indicates that Sc_2O_3 is also stable under the dose conditions employed. It will be also necessary to establish the long-term stability of the proton-irradiation deices, in order to ascertain any differences from unpassivated devices irradiation under the same conditions.

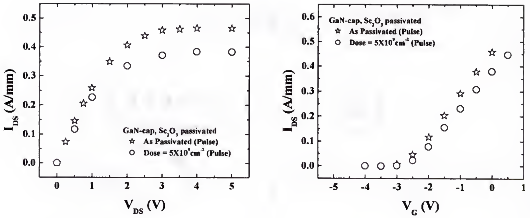

Figure 7-37. Gate lag measurements of Sc$_2$O$_3$ passivated GaN-cap HEMT. At left, V_G is switched from -5V to 0V, while at right it is switched from -5V to the value shown in the X-asix.

(b) AlGaN-cap HEMTs

The I_{DS}-V_{DS} characteristics, transfer characteristics and forward and reverse I-V characteristics are shown in Figure 7-38 both before and after proton irradiation. The changes are again very small at the 5×10^9 cm^{-2} dose, with perhaps even less damage than measured for the GaN cap devices. The may be due to the greater radiation hardness of AlGaN because of its higher average band strength relative to GaN.

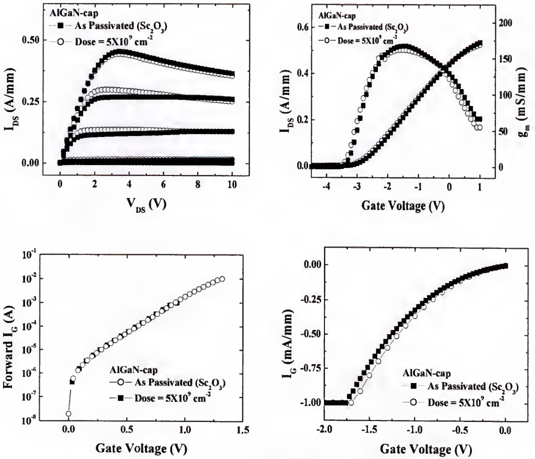

Figure 7-38. dc characteristics of Sc_2O_3 passivated, AlGaN-cap HEMTs before and after proton irradiation.

Figure 7-39 shows the gate lag data. Once again the Sc_2O_3 passivation effectively eliminates the effect of the surface states and the proton irradiation produces a small deterioration in drain-source current. However, an unpassivated device irradiated under the same conditions suffers a much greater degradation in I_{DS}, implying that three are significant number of surface traps created by the proton irradiation. These traps are also passivated by the Sc_2O_3 layer in addition to the existing traps present after growth of the HEMT. In this respect the presence of the Sc_2O_3 serves as a radiation-hardening mechanism, protecting the HEMT from the degradation it would otherwise suffer as a result of the proton-induced damage.

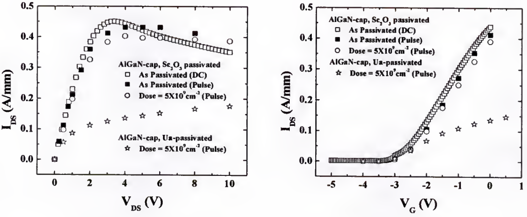

Figure 7-39. Gate lag measurements of unpassivated and Sc_2O_3 passivated AlGaN-cap HEMTs. At left, V_G is switched from -5V to 0V, while at right it is switched from -5V to the value shown in the X-asix.

MgO and Sc_2O_3 passivated HEMTs show minimal changes I surface-related trapping as a result of high energy proton irradiation and all changes in their dc performance result from traps created in a near the channel layer. The oxide passivation also serves to reduce the effect of near-surface traps created by the protons traversing the layer structure.

LIST OF REFERENCES

1. S. R. Wang, Z. L. Liu, G. R. Liang, X. Q. Liang and H. Z. Ma, *Chinese Journal of Semiconductors,* **22**, 755(2001).
2. S. Lombardo, *Microelectronic Engineering,* **59**, 33(2001).
3. J. W. Johnson, B. P. Gila, B. Luo, K. P. Lee, C. R. Abernathy, S. J. Pearton, J. I. Chyi,T. E. Nee, C. M. Lee, C. C. Chuo, and F. Ren, *Journal of the Electrochemical Society,* **148**, G303(2001).
4. Crupi, I. ; Lombardo, S.; Spinella, C.; Bongiorno, C.; Liao, Y.; Gerardi, C.; Fazio, B.; Vulpio, M.; Privitera, S. *Journal of Applied Physics,* **80**, 5552(2001).
5. Sharma, R.K. ; Kumar, A.; Anthony, J.M., *JOM,* **53**, 53(2001).
6. Chen, K.M. ; Sparks, A.W.; Hsin-Chiao Luan, Lim, D.R.; Wada, K.; Kimerling, L.C., *Applied Physics Letters,* **75**, 3805(1999).
7. Jong-Hyeob Back ; Won Seok Han, Hyung Koun Cho, Bun Lee; In Hoon Choi, *Electronics Letters, Volume,* **35**, 814(1999).
8. Shiuh Chao ; Wen-Hsiang Wang; Cheng-Chung Lee, *Applied Optics,* **40**, 2177(2001).
9. Bin Wang ; Suehle, J.S.; Vogel, E.M.; Bernstein, J.B., *IEEE Electron Device Letters, 22*, 224(2001).
10. Schmidt, J. ; Kerr, M.; Cuevas, A., *Semiconductor Science and Technology*, **16**, 164(2001).
11. A. Teramoto, H. Umeda, K. Azamawari, K. Kobayashi, K. Shiga, J. Komori, Y. Ohno and A. Shigetomi, *Microelectronics Reliability,* **41**, 47(2001).
12. K. Sakamoto, K. Asada and T. Sameshima, *Solar Energy Materials and Solar Cells,* **65**, 565(2001)
13. H. F. Sterling and R. C. G. Swann, *Solid-State Electronics*, **8**, 653(1965).

14. Smith, A. S. Alimonda and F. von Pressig, in " *Symposium Proceedings o Chemical Perspectives of Microelectronic Materials* ", **131**, Materials Research Society, Pittsburg, PA (1989).
15. K. Suzuki, T. Aoki, M. Ikeda, Y. Okada, Y. Zohta and K. Ide, *SID'83 Dig*, **00**, 146(1983).
16. H. Uchida, K. Takechi, S. Nishida and S. Kaneko, *Jpn. J. Appl. Phys.*, **30**, 3691(1991).
17. Lanford and M. J. Rand. *Journal of Applied Physics*, **49**, 2473(1978).
18. H. J. Stein, V. A. Wells, and R. E. Hampy, *Journal of Electrochemical Society*, **126**, 1750(1979).
19. R. Chow, W. A. Landoed, K. M. Wang, and R. Rosler, *Journal of Applied Physics*, **53**, 5630(1982).
20. D. G. Esaev, V. M. Efimov and A. A. Shklyaew, *Thin Solid Films*, **221**, 160(1992).
21. G. V. Gadiyak, *Journal of Applied Physics*, **82**, 5573(1997).
22. S. T. Sah, *Solid-State Electronics*, **33**, 147(1990).
23. R. C. Sun, J. T. Clemens and J. T. Nelson, in *Proc. IEEE Rel. Phys.*, 244(1980).
24. H. Uchida, K. Takechi, S. Nishida and S. Kaneko, *Jpn. J. Appl. Phys.*, **30**, 3691(1991).
25. Y. Kuo, *Vacuum*, **51**, 741(1998)
26. M. J. Loboda, and J. A. Seifferly, *J. Mater. Res.*, **11**, 391(1996).
27. P. Roca I Cabarrocas, *Mater. Res. Soc. Symp. Proc.*, **149**, 33(1989).
28. G. N. Parsons, J. H. Souk, and J. Batey, *J. Appl. Phys.*, **70**, 1553(1991).
29. B. F. Hanyaloglu and E. S. Aydi, *J. Vac. Sci. Technol. A*, **16**, 2794(1998).
30. S. Sitbon, M. C. Hugon, B. Agius, F. Abel, J. L. Courant and M. Puech, *J. Vac. Sci. Technol. A*, **13**, 2900(1995).
31. R. Chow, W. A. Lanford, W. Ke-Ming, and R. S. Rosler, *J. App. Phys.*, **53**, 5360(1982).
32. M. Maeda and H. Nakamura, *J. Appl. Phys.*, **58**, 484(1985).
33. D. L. Smith, A. S. Alimonda, C. C. Chen, and H. C. Tuan, *J. Electron. Mater.* **19**, 19(1990).

34. J. Campmay, J. L. Anjujar, A. Canillas, J. Cifre, and E. Bertran, *Sens. Actuators A*, **37-38**, 333(1993).

35. Q. W. Ren, L. K. Naver, C. R. de Boerand H. W. van Zeijl, *Microelectronic Engineering*, **36**, 179(1997).

36. Y. Kuo, *J. Electrochem. Soc.*, **142**, 186(1995).

37. S. Matsuo and M. Kiuchi, *Jpn. J. Appl. Phys.*, **22**, L210(1983).

38. J. Yota, J. Hander, and A. A. Saleh, *J. Vac. Sci. Technol. A*, **18**, 372(2000).

39. G. Martin, S. Strite, A. Botchkarev, A. Agarwal, A. Rockett, H. Morkoc, W.R.L. Lambrecht, B. Segall, *Applied Physics Letters*, **65**, 610(1994).

40. J. Baur, K. Maier, M. Kunzer, U. Kaufmann, J. Schneider, *Applied Physics Letters*, **65**, 1211(1994).

41. J.P. Waldrop, R.W. Grant, *Applied Physics Letters*, **68**, 2879(1996).

42. C.G. Van de Walle, J. Neugebauer, *Applied Physics Letters*, **70**, 2577(1997).

43. M.G. Nardelli, K. Rapcewicz, J. Bernholc, *Journal of the Vacuum Science and Technology B*, **15**, 1144(1997).

44. W.R.L. Lambrecht, K. Kim, S.N. Rashkeev, B. Segall, *Materials Research Society Symposium Proceedings*, **395**, 455(1996).

45. G. Martin, A. Botchkarev, A. Rockett, H. Morkoc, *Applied Physics Letters*, **68**, 2541(1996).

46. J.A. Majewski, M. StaK dele, P. Vogl, *Materials Research Society Symposium Proceedings*, **449**, 917(1997).

47. J.F. Nye, Physical Properties of Crystals, Oxford University Press, Oxford, 1985.

48. F. Bernadini, V. Fiorentini, D. Vanderbilt, *Physical Review B*, **56**, R10024(1997).

49. K. Tsubouchi, K. Sugai, N. Mikoshiba, *IEEE Ultrasonic Symposium*, **1**, 375(1981).

50. G.D. O'Clock, M.T. Du!y, *Applied Physics Letters*, **23**, 55(1973).

51. M.A. Littlejohn, J.R. Hauser, T.H. Glisson, *Applied Physics Letters*, **26,** 625(1975).

52. K. Shimada, T. Sota, K. Sizuki, *Journal of Applied Physics*, **84,** 4951(1998).

53. A.S. Barker Jr., M. Ilegems, *Physical Review B*, **7**, 743(1973).

54. F. Bernardini, V. Fiorentini, *Physical Review Letters*, **79,** 3958(1997).

55. V. Fiorentini, F. Bernadini, F. Della Sala, A. Di Carlo, P. Lugli, *Physical Review B*, **60**, 8849(1999).

56. M. Asif Khan, J.W. Yang, G. Simin, H. zur Loye, R. Bicknell-Tassius, R. Gaska, M.S. Shur, G. Tamulaitis, A. Zukauskas, *Physics Status Solidi (A)*, **176**, 227(1999).

57. H. Amano, T. Takeuchi, S. Sota, H. Sakai, I. Akasaki, *Materials Research Society Symposium Proceedings*, **449**, 1143(1997).

58. O. Ambacher, J. Smart, J.R. Shealy, N.G. Weimann, K. Chu, M. Murphy, W.J. Scha!, L.F. Eastman, R. Dimitrov, L. Wittmer, M. Stutzmann, W. Rieger, J. Hilsenbeck, *Journal of Applied Physics*, **85**, 3222(1999).

59. E.T. Yu, G.J. Sullivan, P.M. Asbeck, C.D. Wang, D. Qiao, S.S. Lau, *Applied Physics Letters*, **71**, 2794(1997).

60. M.S. Shur, *Materials Research Society Symposium Proceedings*, **483**, 15(1998).

61. L. Hsu, W. Walukiewicz, *Physical Review B*, **56**, 1520(1997).

62. B.K. Ridley, *Journal of Applied Physics*, **84**, 4020(1998).

63. S. Dhar, S. Ghosh, *Journal of Applied Physics*, **86**, 2668(1999).

64. R. Gaska, M.S. Shur, A.D. Byhhovski, A.O. Orlov, G.L. Snider, *Applied Physics Letters*, **74**, 287(1999).

65. I.P. Smorchkova, C.R. Elsass, J.P. Ibbetson, R. Vetury, B. Heying, P. Fini, E. Haus, S.P. DenBaars, J.S. Speck, U.K. Mishra, *Journal of Applied Physics*, 4520(1999).

66. K. Leung, A.F. Wright, E. B Stechel, *Applied Physics Letters*, **74**, 2495(1999).

67. D.C. Look, J.R. Sizelove, *Physical Review Letters*, **82**, 1237(1999).

68. H.M. Ng, D. Doppalapudi, T.D. Moustakas, N.G. Weimann, L.F. Eastman, *Applied Physics Letters*, **73**, 821(1998).

69. N.G. Weimann, L.F. Eastman, D. Doppalapudi, H.M. Ng, T.D. Moustakas, *Journal of Applied Physics*, **83**, 3656(1998).

70. J. J. Xu, S. Keller, G. Perish, S. Heikman, U. K. Mishra, R. A. York, *2000 IEEE MTT-S International Microwave Symposium Digest.*, **2** , 959(2000).

71. N. Q. Zhang, B. Moran, S. P. DenBaars, U. K. Mishra, X. W. Wang, T. P. Ma, *2001 IEDM Technical Digest. International Electron Devices Meeting*, 25.5.1 - 25.5.4(2001).

72. R. Vetury, N. Q. Zhang, S. Keller, U. K. Mishra, *IEEE Transactions on Electron Devices*, **48**, 560(2001).

73. W. Mickanin, P. Canfield, E. Finchem, and B. Odekirk, *GaAs IC Symp. Dig.*, 211(1989).

74. R. Yeats et al., in *IEDM Tech. Dig.*, 842(1988).

75. J. C. Huang et al., *IEEE Trans. Microwave Theory Techniques*, **41**, 752(1993).

76. S. C. Binari, K. Ikossi, J. A. Roussos, W. Kruppa, P. Doewon, H. B. Dietrich, D. D. Koleske, A. E. Wickenden, R. L. Henry, *IEEE Transactions on Electron Devices*, **48**, 465(2001).

77. V. Tilak, B. Green, H. Kim, R. Dimitrov, J. Smart, W. J. Schaff, J. R. Shealy, L. F. Eastman, *2000 IEEE International Symposium on Compound Semiconductors*, 357(2000).

78. S. Karmalkar, U. K. Mishra, *IEEE Transactions on Electron Devices*, **48,** 1515(2001).

79. K. L. Lear, A. Mai, K. D. Choquette, S. P. Kilcoyne, R. P. Schneider, Jr. and K.M. Geib, *Electron. Lett.* **32,** 457 (1996).

80. B. J. Thibeault, K. Bertilsson. E. R. Hegblom, E. Strzelecka, P. D. Floyd, A. Naone and L. A. Coldren *IEEE Photon. Tech. Lett.*, **9,** 11 (1997).

81. D. Weidermann, R. King. C. Fung, R. Jager, R. Michalzik, P. Schnitzer, M. Kicherer and K. J. Ebeling *IEEE J. Selected Topics in Quantum Electronics*, **5**, 503 (1999).

82. N. Hatori, A. Mizutani, N. Nishiyama, A. Matsutani, T. Sahaguchi, F. Motomura, F. Koyama and K. Iga *IEEE Photon. Tech. Lett.* **10**, 194 (1998).

83. B. Weige, M. Grabherr, C. Jung, R. Jager, G. R. Aeiner, R. Michalzek, D. Sowada and K. J. Ebeling, *IEEE J. Selected Topics in Quantum Electronics* **4**, 409 (1997).

84. L. M. F. Chirovsky, W. S. Hobson, R. E. Leibenguth, S. P. Hui, J. Lopata, G. J. Zydzik, G. Giaretta, K. W. Goossen, J. D. Wynn, A. V. Krishnamoorthy, B. J. Tseng, J. M. Vandenberg, and L. A. D'Asaro, *IEEE Photon. Technol. Lett.*, **11**, 500-502 (1999).

85. F. Ren, A. B. Emerson, S. J. Pearton, T. R. Fullowan and J.M. Brown, *Appl. Phys.*

Lett., **58**, 1030-1032 (1991).

86. R.A. Morgan, J.A. Lehman, and M.K. Hibbs-Brenner, "Vertical-cavity surface-emitting lasers come of age", in Proc. SPIE, M. Fallahi and S.C. Wang, Chairs/Eds., San Jose, CA, **2683**, 18-29 (1996).
87. G. Dang, W. S. Hobson, L. M. F. Chirovsky, J. Lopata, M. Tayahi, S. N. G. Chu, F. Ren, and S. J. Pearton, "High-Speed Modulation of 850 nm, Intra-Cavity Contacted, Shallow Implant-Apertured, Vertical-Cavity Surface-Emitting Lasers", *Solid Stage Electronics*, **45**,1639-1644(2001).
88. F. Ren, C. R. Abernathy, S. J. Pearton, and J. R. Lothian. *Journal of Vacuum Society Technology B*, **13**, 293-296 (1995)
89. J. W. Lee, S. J. Pearton, C. R. Abernathy, W. S. Hobson, F. Ren and C. S. Wu, *Solid-State Electronics*, **38**, 1871-1874 (1995).
90. I. Ishida, S. Wako, S. Ushio, *Thin Solid Films*, **39**, 227(1976).
91. Stareev. *Appl. Phys. Lett.*, **62**, 2801(1993).
92. C. C. Han, X.Z. Wang, S.S. Lau, R.M. Potemski, M.A. Tischler and T.F. Kuech. *Appl. Phys. Lett.*, **58**, 1617(1991).
93. C. C. Han, X. Z. Wang, S. S. Lau, R. M. Potemski, M. A. Tischler and T. F. Kuech. *J. Appl. Phys.*, **69**, 3124(1991).
94. B. M. Henry, A. E. Staton-Bevan, V. Sharma, M. A. Crouch, and S. S. Gill, *Mater. Res. Soc. Symp. Proc.*, **240**, 431(1992).
95. S. J. Pearton, J. C. Zolper, R. J. Shul and F. Ren, *J. Appl. Phys.* **86**, 1(1999).
96. E. R. Brown, *Solid-State Electron.* **43**, 1918(1998).
97. G. T. Heydt and B. J. Skromme, *Mat. Res. Soc. Symp. Proc.* **483**, 3(1998).
98. S. J. Pearton, F. Ren, A. P. Zhang and K. P. Lee, *Mat. Sci. Eng. Rep. R* **30**, 55(2000).
99. Z. Z. Bandic, P. M. Bridger, E. C. Piquette, T. C. McGill, R. P. Vaudo, V. M. Phanse, and J. M. Redwing, *Appl. Phys. Lett.* **74**, 1266(1999).
100. J. –I. Chyi, C. –M. Lee, C. C. Chuo, X. A. Cao, G. T. Dang, A. P. Zhang, F. Ren, S. J. Pearton, S. N. G. Chu, and R. G. Wilson, *Solid-State Electron.* **44**, 613(2000).
101. A. P. Zhang, G. Dang, X. A. Cao, H. Cho, F. Ren, J. -I. Chyi, C. M. Lee, T. E. Nee,

C. C. Chuo, G. C. Chi, S. N. G. Chu, R. G. Wilson, and S. J. Pearton, *MRS Internet J. Nitride Semicond. Res.* **5S1**, W11.67(2000).

102. A. P. Zhang, G. Dang, F. Ren, J. Han, A. Y. Polyakov, N. B. Smirnov, A. Govorkov, J. M. Redwing, X. Cao, and S. J. Pearton, *Appl. Phys. Lett.* **76**, 1767(2000).
103. A. P. Zhang, G. Dang, F. Ren, J. Han, A. Y. Polyakov, N. B. Smirnov, A. Govorkov, J. M. Redwing, H. Cho and S. J. Pearton, *Appl. Phys. Lett.* **76**, 3816(2000).
104. A. P. Zhang, J. W. Johnson, F. Ren, J. Han, A. Y. Polyakov, N. B. Smirnov, A. Govorkov, J. M. Redwing, K. P. Lee and S. J. Pearton, *Appl. Phys. Lett.* **78**, 823(2001).
105. T. G. Zhu, D. J. H. Lambert, B. S. Shelton, M. M. Wong, V. Choudhury, and R. D. Dupuis, *Appl. Phys. Lett.* **77**, 2918(2000).
106. A. P. Zhang, G. Dang, F. Ren, H. Cho, K. P. Lee, S. J. Pearton, J. I. Chyi, T. Nee, C. M. Lee, and C. Chuo, *IEEE Trans. Electron Devices* **48**, 407(2001).
107. J. W. Johnson, J. LaRoche, F. Ren, B. P. Bila, M. E. Overberg, C. R. Abernathy, J. I. Chyi, C. Chuo, T. Nee, C. M. Lee, K. P. Lee, S. S. Park, J. Park and S. J. Pearton, *Solid-State Electron.* **45**, 405(2001).
108. A. P. Zhang, J. W. Johnson, B. Luo, F. Ren, S. J. Pearton, S. S. Park, Y. J. Park and J. -I. Chyi, *Appl. Phys. Lett.* **79**, 1722(2001).
109. H. P. Maruska and J. J. Tietzer, *Appl. Phys. Lett.* **15**, 367(1969).
110. R. J. Molnar, in "GaN-II", ed. J. I. Peenkove and T. D. Movstakas, (Academic Press, NY 1999).
111. R. P. Vaudo and V. M. Phanse, *Electrochem. Sco. Proc.* **19-18**, 79(1998).
112. D. Doppalapudi and T. D. Movstakus, in Handbook of Thin Films ed. H. S. Nalwa, **Vol. 4** (Academic Press, NY 2002).
113. R. Molnar, W. Goetz, L. T. Rornano and N. M. Johnson, *J. Cryst. Growth.* **178**, 147(1996).
114. T. Detchprohm, K. Hiramatsv, H. Amono and I. Alcasaki, *Appl. Phys. Lett.* **61**, 2688(1992).

115. P. Gibart and B. Beaumant, in GaN-based Technologies, ed. M. Osinski (SPIE Optical Engineering Series, Washington, 2002).

116. H. Morhoc, *Mat. Sci. Eng.* **R33**, 135(2001).

117. M. K. Kelly, R. P. Vaudo, V. M. Phanse, L. Gorgens, O. Ambacher and M. Stutzmana, *Jpn. J. Appl. Phys.* **38**, L217(1999).

118. S. S. Park, I.-W. Park and S. H. Chok, *Jpn. J. Appl. Phys.* **39**, L1141(2000).

119. K. Lee and K. Auh, *Jpn. J. Appl. Phys.* **40**, L13(2001).

120. S. T. Kim, Y. J. Lee, D. C. Moon, C. Hong and T. K. Soo, *Semicond. Sci. Technol.* **14**, 278(1999).

121. Y. V. Melaik, K. V. Vassilevski, I. P. Nikitina, A. I. Babanin, Y. Davydov and A. V. Dmitriev, *MRS Technol J. Nitride Semicond. Res.* **2**, 39(1997).

122. A. Wakahara, T. Yamamoko, K. Ishio, A. Yoshida, Y. Seki, K. Kainosho and O. Oda, *Jpn. J. Appl. Phys*. **39**, 2399(2000).

123. O. Kryliovk, M. Reed, T. Dann and T. J. Anderson, *Mat. Sci. Eng.* **B66**, 26(1999).

124. K. Motoki, *Jpn. J. Appl. Phys.* **40**, L140(2001).

125. S. Nagahamn, N. Iwasa, M. Senoh, T. Matsushita, Y. Sugimoto, H. Kikoyv, T. Kozaki, M. Suno, H. Matsumura, H. Vinemoko, K. Kocho and T. Mukai, *Jpn. J. Appl. Phys*. **39**, L647(2000).

126. J. C. Zolper, *Tech Digest IEDM* **389**, 16.1.1 (1999).

127. see for example, the papers in the special issue on GaN Electronics, *IEEE Trans Electron. Dev.* **ED48**, (2001), ed J. C. Zolper and V. K. Mishra.

128. R. T. Kemeley, H. B. Wallace and M. N. Yoder, *Proc. IEEE* **90**, 1059(2002).

129. V. K. Mishra, P. Parikh and Y.-F. Wu, *Proc. IEEE* **90**, 1022(2002).

130. R. J. Trew, *Proc. IEEE* **90**, 1032(2002).

131. J. W. Johnson, F. Ren, S. J. Pearton, A. G. Baca, J. Han, A. M. Dabiran and P. P. how, *J. Nanosci. Nanotech.* **2**, 325(2002).

132. B. Luo, J. W. Johnson, J. Kim, R. M. Mehandru, F. Ren, B. P. Gila, A. H. Onstine, C. R. Abernathy, S. J. Pearton, A. G. Baca, R. D. Briggs, R. J. Shul, C. Monier and J. Han, *Appl. Phys. Lett.* **80**, 1661(2002).

133. J. Gillespie, R. C. Fitch, J. Sewell, R. Dettmer, G. Via, A. Crespo, T. Jenkins, B.

Luo, R. Mehandru, J. Kim, F. Ren, B. P. Gila, A. H. Onstine, C. R. Abernathy and S. J. Pearton, *IEEE Trans. Electron. Dev.* **23**, 505(2002).

134. B. Luo, R. Mehandru, J. Kim, F. Ren, B. P. Gila, A. H. Onstine, C. R. Abernathy S. J. Pearton, R. Fitch, J. Gillespie, T. Jenkins, J. Sewell, D. Via, A. Crespo and Y. Irokawa, *J. Electrochem. Soc.*, **149**, G613 (2002).
135. J. W. Lee and F. Ren, in Handbook of Advanced Plasma Processing Techniques, ed. R. J. Shul and S. J. Pearton (Springer, Berlin 2000).
136. R. J. Shul, A. J. Howard, C. B. Vartuli, P.A. Barnes, and S. Weng. *J. Vac. Sci. Technol. A*, **14**, 1102(1996).
137. R. J. Shul, M. L. Lovejoy, D. L. Hetherington, D. J. Rieger, F. F. Klem, and M. R. Melloch. *J. Vac. Sci. Technol. B*, **13**, 27(1995).
138. K. K. Ko and S. W. Pang. *J. Vac. Sci. Technol. B*, **13**, 2376(1995).
139. J. Etrillard, P. Osart, G. Patriarch, M. Juhel, J. F. Bresse, and C. Daguet. *J. Vac. Sci. Technol. A*, **15**, 626(1997).
140. E. Berg and S. W. Pang. *J. Vac. Sci. Technol. B*, **15**, 2643(1997).
141. D. G. Yu, C.-H. Chen, A. L. Holmes. Jr., S. D. DenBaars, and E. L. Hu. *J. Vac. Sci. Technol. B*, **15**, 2672(1997).
142. S. J. Pearton. *Int. J. Mod. Phys. B*, **8**, 1781(1994).
143. S. J. Pearton. *J. Vac. Sci. Technol. A*, **12**, 1966(1994).
144. C. S. Wu, F. Ren, S. J. Peaton, M. Hu, C. K. Pao, and R. F. Wang. *Electron. Lett.*, **30**, 1803(1994).
145. F. Ren, A. Y. Cho, J. M. Kuo, S. J. Peaton, J. R. Lothian, D. L. Sivco, R. G. Wilson, and Y. K. Chen, *Electron. Lett.*, **31**, 406(1995).
146. J. G. van Hassel, C. M. van Es, and R. A. M. Nouwens. *Electron. Lett.*, **31**, 834(1995).
147. S. J. Pearton, J. W. Lee, J. D. MacKenzie, C. R. Abernathy, and R. J. Shul. *Appl. Phys. Lett.*, **67**, 2329(1995).
148. J. W. Lee, S. J. Pearton, C. R. Abernathy, W. S. Hobson, and F. Ren. *Appl. Phys. Lett.*, **67**, 3129(1995).
149. R. J. Shul, C. T. Sullivan, M. B. Snipes, G. B. McClellan, M. Hafich, C. T. Fuller,

C. Constantine, J. W. Lee, and S. J. Pearton. *Solid-State Electron.*, **38**, 2047(1995).

150. R. R. Stradtmann, J. W. Lee, C. R. Abernathy, S. J. Peatron, and W. S. Hobson. *J. Electrochem. Soc.*, **143**, L219(1996).
151. S. J. Pearton. *Mat. Sci. Eng. B*, **40**, 101(1996).
152. F. Ren, J. R. Lothian. J. D. MacKenzie, C. R. Abernathy, C. B. Vartui, S. J. Pearton, and R. G. Wilson. *Solid-State Electron.*, **39**, 1747(1996).
153. K. N. Lee, J. W. Lee, C. R. Abernathy, S. J. Pearton, W. S. Hobson, and F. Ren, *Solid-State Electron.*, **40**, 401(1997).
154. S. J. Pearton. *Mater. Sci. Eng. B*, **44**, 1(1997).
155. J. W. Lee, D. Hays, C. R. Abernathy, S. J. Pearton, W. S. Hobson, and C. Constantine. *J. Electrochem. Soc.*, **144**, L245(1997).
156. S. J. Pearton. *Appl. Surf. Sci.*, *117/118*, 597(1997).
157. J. W. Lee, C. R. Abernathy, S. J. Pearton, F. Ren, W. S. Hobson, R. J. Shul, C. Constantine, and C. Barratt. *J. Electrrochem. Soc.*, **144**, 1417(1997).
158. F. Ren, J. W. Lee, C. R. Abernathy, S. J. Pearton, C. Constantine, C. Barratt, and R. J. Shul. *Appl. Phys. Lett.*, **70**, 2410(1997).
159. J. W. Lee, C. R. Abernathy, S. J. Pearton, F. Ren, R. J. Shul, C. Constantine, and C. Barratt, *Solid-State Electron.*, **41**, 829(1997).
160. F. Ren, J. W. Lee, C. R. Abernathy, S. J. Pearton, C. Constantine, C. Barratt, and R. J. Shul. *J. Vac. Sci. Technol. B*, **15**, 983(1997).
161. F. Ren, J. W. Lee, C. R. Abernathy, S. J. Pearton, R. J. Shul, C. Constantine, and C. Barratt. *Semicond. Sci. Technol.*, **12**, 1154(1997).
162. F. Ren, D. N. Buckley, K. N. Lee, S. J. Pearton, R. A. Bartynski, C. Constantine, W. S. Hobson, R. A. Hamm, and D. C. Chao. *Solid-State Electron.*, **38**, 2011(1996).
163. S. Thomas III, H. H. Chen, and S. W. Pang. *J. Vac. Sci. Technol. B*, **15**, 681(1997).
164. S. W. Pang, S. Thomas III, and H. H. Chen. *Appl. Surf. Sci.*, **117/118**, 758(1997).
165. S. J. Pearton, F. Ren, T. R. Fullowan, J. R. Lothian, A. Katz, R. F. Kopf, and C. R. Abernathy. *Plasma Sources Sci. Technol.*, **1**, 18(1992).
166. F. Ren, T. R. Fullowan, S. J. Pearton, J. R. Lothian, R. Esagui, C. R. Abernathy, and W. S. Hobson. *J. Vac. Sci. Technol. A*, **11**, 1768(1993).

167. S. Thomas III, H. H. Chen, C. K. Hamish, J. W. Grizzle, and S. W. Pang. *J. Vac. Sci. Technol. B*, **14**, 2531(1996).

168. S. J. Pearton, F. Ren, C. R. Abernathy, W. S. Hobson, T. R. Fullowan, R. Esagui, and J. R. Lothian. *Appl. Phys. Lett.*, **61**, 586(1992).

169. S. J. Pearton, F. Ren, C. R. Abernathy, T. R. Fullowan, and J. R. Lothian. *Semicond. Sci. Technol.*, **6**, 1116(1991).

170. F. Ren, J. R. Lothian, S. J. Pearton, C. R. Abernathy, P. W. Wisk, T. R. Fullowan, B. Tseng, S. N. G. Chu, Y. K. Chen, L. W. Yang, S. T. Fu, R. S. Brozovich, H. H. Lin, C. L. Henning, and T. Henry. *J. Vol. Sci. Technol. B*, **12**, 2916(1994).

171. S. J. Pearton, J. W. Corbett, and T. S. Shi. *Appl. Phys. A*, **43**, 153(1987).

172. F. Ren, C. R. Abernathy, S. N. G. Chu, J. R. Lothian, and S. J. Pearton. *Solid-State Electron.,* **38**, 1137(1995).

173. C. S. Wu, F. Ren, S. J. Pearton, M. Hu, C. K. Pao, and R. F. Wang. *IEEE Trans. Electron. Device*, **ED42**, 149(1995).

174. See, for example, P. M. Asbeck, M. –C. Chang, K. C. Wang, and D. L. Miller, in *Introduction to Semiconductor Technology: GaAs and Related Compounds*, edited by C. T. Wang (Wiley-Interscience, New York, 1990), Chap. 4.

175. K. Honjo, *Solid-State Electron.* **38**, 1569(1995).

176. P. M. Asbeck, *Solid-State Electron.* **38**, 1691 (1995).

177. S. Tanaka, H. Hayama, A. Furukawa, T. Baba, M. Mizuta, and H. Honjo, *Electron. Lett.* **26**, 1439(1990)

178. H. F. Chau, W. Liu, and E. A. Beam III, *Proceedings of the 7th International Conference on InP and Related Materials* (IEEE, New York, 1995) pp. 640-644.

179. E. A. Beam III, B. Brar, T. P. E. Broekaert, H. F. Chan, W. Liu, and A. C. Seabaugh, *Mater. Res. Soc. Symp. Proc.* **421**, 3(1996).

180. T. R. Fullowan, S. J. Pearton, R. F. Kopf, and R. P. Smith, *J. Vac. Sci. Technol. B* **9**, 1445(1991).

181. M. Hafizi and W. E. Stanchina, in *InP HBTs: Growth, Processing, and Applications*, edited by B. Jalali and S. J. Pearton (Artech Hourse, Boston, 1994), Chap. 5.

182. S. Thomas III, K. K. Ko, and S. W. Pang, *J. Vac. Sci. Techno. A* **13**, 894(1995).
183. C. R. Abernathy, *Mater. Sci. R. Rep.* **14,** 203(1995).
184. M. Papastamatiou, N. Arpatzanis, G. J. Papaioannou, G. Constantinides, C. Michelakis and Z. Hatzopoulos. *Physica Status Solidi (A) Applied Research*, **180,** 569-584(2000).
185. N. V. Demarina and S. V. Obolensky. *Microelectronics and Reliability*, **39**, 1247-1263(1999).
186. D. M. Hiemstra, A. A. Kizeevi, L. Z. Hou and C. A. T. Salama. *IEEE Transactions on Nuclear Science*, **45**, 2616-2623(1998)
187. G. Battistoni, D. V. Camin, N. Fedyakin, G. Pessina and P. Sala. *Nuclear Instruments and Methods in Physics Research Section A: Accelerators, Spectrometers, Detectors and Associated Equipment*, **388**, 399-407(1997)
188. G. L. Hash, J. R. Schwank, M. R. Shaneyfelt, C. E. Sandoval, M. P. Connors, T. J. Sheridan, F. W. Sexton, E. M. Slayton, J. A. Heise and C. C. Foster. *IEEE Transactions on Nuclear Science*, **41**, 2259-2266(1994)
189. M. Citterio, S. Rescia and V. Radeka. *IEEE Transactions on Nuclear Science*, **42**, 2266-2270(1995)
190. N. Arpatzanis, R. Vlastou, G. Konstantinidis, M. Papastamatiou, E. Gazis and G. J. Papaioannou. *Solid State Electronics*, **42**, 277(1998).
191. Cheng T. Wang, Introduction to Semiconductor Technology: GaAs and Related Compounds, John Wiley & Sons, 337(1990)
192. Frank H. Attix, Introduction to Radiological Physics & Radiation Dosimetry, John Wiley & Sons, Inc., 103(1986).
193. James E. Turner, Atoms, Radiation, and Radiation Protection, 2nd Edition, John Wiley & Sons, Inc., 195(1995)
194. Glenn F. Knoll, Radiation Detection and Measurement, John Wiley & Sons, 59(1989).
195. C. Nquyen and M. Micovic, IEEE Trans. Electron. Dev. 48, 472(2001).
196. M. A. Cistvan, P. J. Vold and D. K. Arch, *IEEE Trans. Nucl. Sci.* **NS-34,** 1667(1987).

197. J. F. Sulzman, P. J. Mindty ad A. R. Knudson, IEEE Trans. Nucl. Sci. NS-34 1667(1987)

198. J. Liou, Phys. Stat. Solids A 119, 337(1990).

199. J. R. Srour and J. M. McGarrity, Proc. IEEE 76, 1443(1998)

200. A. Schrantz, N. W. van Vonno, W. A. Krull, M. A. Rao, S. I . Cong and H. Kroemer, IEEE Trans. Nucl. Sci. NS-35, 1657(1988).

201. Y. Song, M. E. Kion, A. K. Oki, M. E. Hafizi. J. B. Camor and K. W. Kobayaski, 11th GaAs IC Symp. Tech. Dig. 1989, pp.155-158.

202. S. B. Witmer, S. D. Miltleman and S. J. Pearton, in InP HBTs: Growth, Processing and Application, ed. B. Jalali and S. J. Pearton (Artech Hourse, Boston, 1995).

203. Ren, A. Y. Cho, Y. M. Kuo, S. J. Pearton, J. R. Lothian, D. L. Sino, R. G. Wilson and Y. K. Chen, Electron. Lett. 31, 46(1995).

204. B. Luo, J. W. Johnson, D. Schoenfeld, S. J. Peartona and F. Ren, Solid-State Electron. 45, 1149(2001).

205. B. Luo, J. W. Johnson, F. Ren, K. K. Allums, C. R. Abernathy and S. J. Pearton, R. Dwivedi, T. N. Fogarty and R. Wilkins, A. M. Dabiran, A. M. Wowchack, C. J. Polley and P. P. Chow and A. G. Baca, Appl. Phys. Lett. (Oct. 8 issue, 2001).

206. G. Simin, X. Hu, N. Ilinskaya, J. Zhang, A. Tarakji, A. Kumar, J. Yang, M. A. Khan, R. Gaska, and M. S. Shur, *IEEE Electron Dev. Lett.*, **22**, 53(2001).

207. H. Morkoc, R. Cingolani and B. Gil. Solid-State Electron., 43, 1909(1999).

208. C. Nguyen, N. X. Nguyen and D. E. Grider, Electron. Lett., 35, 1380(1999).

209. L. F. Eastman, V. Tilak, J. Smart, B. M. Green, E. M. Chumbes, R. Dimitrov, H. Kim, O. S. Ambacher, N. Weimann, T. Prunty, M. Murphy, W. J. Schaff and J. R. Shealy, *IEEE Trans. Electron Dev.*, **ED48**, 479(2001).

210. W. Lu, J. Yang, M. A. Khan and I. Adesida, *IEEE Trans. Electron Dev.*, **ED48**, 581(2001).

211. R. J. Trew, *IEEE Microwave Mag.*, **1**, 46(2000).

212. S. Keller, Y.-F. Wu; G. Parish, N. Ziang; J. J. Xu, B. P. Keller, S. P. DenBaars, and U. K. Mishra, *IEEE Trans. Electron Dev.*, **ED48**, 552(2001).

213. D. C. Look, D. C. Reynolds, J. W. Hemsky, J. R. Sizelove, R. L. Jones and R. J.

Molnar, *Phys. Rev. Lett.*, **79**, 2273(1997).

214. S. J. Cai, Y. S. Tang, R. Li, Y. Y. Wei, L. Wong, Y. L. Chen, K. L. Wang, M. Chen, R. D. Schrimpf, J. C. Keay and K. F. Galloway, *IEEE Trans Electron Dev.*, **ED47**, 304(2000).
215. B. Luo, J. W. Johnson, F. Ren, K. K. Allums, C. R. Abernathy, S. J. Pearton, R. Dwivedi, T. N. Fogarty, R. Wilkins, A. M. Dabiran, A. M. Wowchack, C. J. Polley, P. P. Chow and A. G. Baca, *Appl. Phys. Lett.*, **79**, 2196(2001).
216. J. M. Van Hove, P. P. Chow, A. M. Wowchack, J. J. Klaassen, R. Hickman, and C. J. Polley, J. Vac. Sci. Technol., B16, 1286(1998).
217. L. Chernyak, A. Osinsky and A. Schulte, *Solid-State Electron.*, **45**, 1687(2001).
218. L. Chernyak, A. Osinsky, G. Nootz, A. Schulte, J. Jasinski, M. Benamara, Z. Lilienthal-Weber, D. C. Look and R. J. Molnar, *Appl. Phys. Lett.*, **77**, 875(2000)
219. L. Chernyak, A. Osinsky, V. Fuflyigin and E. F. Schubert. *Appl. Phys. Lett.*, **77**, 1271(2000).
220. L. Chernyak. A. Osinsky, H. Temkin, Y. W. Yang, Q. Chen and M. A. Khan. *Appl. Phys. Lett.*, **69**, 2531(1996).
221. M. N. Yoder, *IEEE Trans. Electron. Dev.*, **43**, 1633(1996).
222. R. J. Trew, M. W. Shin and V. Gatto, *Solid-State Electron.*, **41**, 1561(1997).
223. T. P. Chow, *Mat. Res. Soc. Symp. Proc.*, **622**, T1.1(2001).
224. see for example, the special issue on group III-N semiconductor electronics, *IEEE Trans. Electron. Dev.*, **48**, 405-408(2001), ed. U. K. Mishra and J. C. Zolper.
225. S. J. Pearton and F. Ren. *Adv. Mat.*, **12**, 1571(2000).
226. J. I. Chyi, C. M. Lee, C. C. Chuo, G. C. Chi, G. Dang, A. P. Zhang, F. Ren, X. A. Cao, S. J. Pearton, S. N. G. Chu, R. G. Wilson, *MRS Internet J. Nitride Semicond. Res.*, **4**, 8(1999).
227. A. P. Zhang, G. Dang, F. Ren, J. Han, H. Cho, S. J. Pearton, J. I. Chyi, T. E. Nee, C. M. Lee, C. C. Chuo, S. N. G. Chu, *Slid-State Electron.*, **44**, 1157(2000).
228. F. Ren, A. P. Zhang, G. T. Dang, X. A. Cao, H. Cho, S. J. Pearton, J. I. Chyi, C. M. Lee, C. C. Chuo, *Solid-State Electron.*, **44**, 619(2000).
229. G. T. Dang, A. P. Zhang, F. Ren, X. A. Cao, S. J. Pearton, H. Cho, J. Han, J. I.

Chyi, C. M. Lee, C. C. Chuo, S. N. G. Chu and R. G. Wilson. *IEEE Trans. Electron. Dev.*, **47**, 692(2000).

230. A. Y. Polyakov, N. B. Smirnov, A. V. Govorkov, G. Dang, A. P. Zhang, F. Ren, X. A. Cao, S. J. Pearton and R. G. Wilson. *J. Vac. Sci. Technol. B*. **18**, 1237(2000).
231. V. Khemkar, R. Patel, T. P. Chow, R. J. Guttmann, *Solid-State Electron.*, **43**, 1945(1999).
232. S. J. Pearton, H. Cho, J. R. LaRoche, F. Ren, R. G. Wilson and J. W. Lee. *Appl. Phys. Lett.*, **78**, 2939(1999).
233. J. C. Zolper, *Mat. Res. Soc. Symp. Proc.*, **622**, T2.4(2001)
234. F. Ren, Mater. Res. Soc. Symp. Proc. 300, 15(1993).
235. E. A. Beam III, B. Brar, T. P. E. Broekaert, H. F. Chau, W. Liu, A. C. Seabaugh, Maer. Res. Soc. Symp. Proc. 61, 556(1996).
236. S. J. Pearton, In: B. Jalali, S. J. Pearton, editors. InP HBTs: growth, processing and devices. Boston: Artech House, Chapter 2(1994).
237. T. R. Hayes, In: A. Katz editors. InP and related materials: processing, technology and devices, Boston: Artech House, Artech House, Chapter 8(1992).
238. J. W. Lee, S. J. Pearton, C. Santana, J. R. Mileham, E. S. Lambers, C. R. Abernathy, F. Ren, W. S. Hobson, J. Electrochem. Soc. 143, 1093(1996).
239. D. L. Melville, J. G. Simmons, D. A. Thompson, J. Sci. Technol. B. 11, 2038(1993).
240. D. C. Hayes, K. P. Lee, B. P. Gila, F. Ren, C. R. Abernathy, S. J. Pearton, J. Electronic Mater. 29, 285(2000)
241. W. Lee, S. J. Pearton, C. R. Abernathy, W. S. Hobson, F. Ren, Solid-State Electron. 41, 159(1997).
242. S. J. Pearton, R. J. Shul, G. F. McLane, C. Constantine, Solid-State Electron. 39, 1095(1996).
243. J. W. Lee, K. D. MacKenzie, D. Johnson, R. J. Shul, S. J. Pearton, C. R. Abernathy, F. Ren, Solid-State Electron. 42, 1021(1998).
244. J. W. Lee, S. J. Pearton, C. R. Abernathy, W. S. Hobson, F. Ren, Mater. Sci. Engng. B 38, 263(1996).

245. F. Ren, S. J. Pearton, D. M. Tennant, D. J. Resnick, C. R. Abernathy, R. F. Kopf, C. S. Wu, M. Hu, C. K. Puo, D. M. Paine, D. C. Wang, C. D. Wen, J. Vac. Sci. Technol. B 10, 2949(1992).

246. S. J. Pearton, F. Ren, J. R. Lothian, T. R. Fullowan, R. F. Kopf, U. K. Chakrabarti, S. P. Hui, A. B. Emerson, R. L. Kostelak, S. S. Pei, J. Vac. Sci. Technol. B 9, 2487(1991).

247. S. Salimian, C. B. Cooper III, J. Vac. Technol. B 6, 1641(1988).

248. S. J. Pearton, C. R. Abernathy, W. S. Hobson, F. Ren, T.R. Fullowan, J. Lopata, U. K. Chakrabarti, M. Stavola, D. M. Kozuch, Mater. Sci. Engng. B, 13, 171(1992).

249. S. J. Pearton, W. S. Hobson, U. K. Chakrabarti, G. E. Derkits, A. P. Kinsella, J. Electrochem. Soc. 137, 3892(1990).

250. F. Ren, P. F. Kopf, J. M. Kuo, J. W. Lee, S. J. Pearton, R. J. Shul, C. Constantine, D. Johnson, Solid-State Electron. 42, 749(1998).

251. F. Ren, S. J. Pearton, J. R. Lothian, C. R. Abernathy, J. Vac. Sci. Technol. B 11, 2603(1993).

252. S. J. Pearton, F. Ren, A. Katz, T. R. Fullowan, C. R. Abernathy, W. S. Hobson, R. F. Kopf, IEEE Electron. Dev. ED-39, 154(1992).

253. K. K. Chu, J. A. Smart, J. R. Shealy and L. F. Eastman, Proc. State-of-The-Art Program on Compound Semiconductors (SOTAPOCS XX/X, Electrochem. Soc., Pennington, NJ 1998), M.3-12.

254. B. M. Green, K. K. Chu, E. M. Chumbes, J. A. Smart, J. R. Shealy, and L. F. Eastman, *IEEE Electron. Dev. Lett.*, **21**, 268(2000).

255. S. C. Binari, W. Kruppa, H. B. Dietrich, G. Kelner, A. E. Wickenden and J. A. Freitas Jr, *Solid-State Electron.*, **41**, 1549(1997).

256. Y. -F. Wu, B. P. Keller, S. Keller, D. Kapolnek, P. Kozodoy, S. P. Denbaars and U. K. Mishra, *Solid-State Electron.*, **41**, 1569(1997).

257. J. W. Johnson, A.G. Baca, R. D. Briggs, R. J. Shul, J. R. Heart, C. Monier, F. Ren, S. J. Pearton, A. M. Dabiran, A. M. Wowchack, C. J. Polley and P. P. Chow, *Solid-State Electron.*, **45**, 1979(2001).

258. M. Asif Khan, Q. Chen, Michael S. Shur, B. T. Dermott, J. A. Higgins, J. Burm, W.

J. Schaff and L. F. Eastman, *Solid-State Electron.*, **41**, 1555(1997).

259. F. Ren, M. Hong, S. N. G. Chu, M. A. Marcus, M. J. Schurman, A. Baca, S. J. Pearton, and C. R. Abernathy, *Appl. Phys. Lett.*, **73**, 3893(1998).
260. J. W. Johnson, B. Luo, F. Ren, B. P. Gila, V. Krishnamoorthy, C. R. Abernathy, S. J. Pearton, J. I. Chyi, T. E. Nee, C. M. Lee, and C. C. Chuo, *Appl. Phys. Lett.*, **77**, 3230(2000).
261. B. P. Gila, J. W. Johnson, K. N. Lee, V. Krishnamoorthy, C. R. Abernathy, F. Ren, and S. J. Pearton, *ECS Proc. Vol.*, **2001-1**, 71(2001).
262. N. X. Nguyen, M. Micovic, W.-S. Wong, P. Hashimoto, L.-M. McCray, P. Janke, C. Nguyen, *Electron. Lett.* **36**, 468(2000).
263. M. A. Khan, X. Hu, G. Simin, A. Lunev, J. Yang, R. Gaska, and M.S. Shur, *IEEE Electron. Dev. Lett.* **21**, 63(2000).
264. E. Kohn, I. Daumiller, P. Schmid, N. X. Nguyen, C. N. Nguyen, *Electron. Lett.* **35**, 1022(1999).
265. J.-S. Lee; A. Vescan, A. Wieszt, R. Dietrich, H. Leier, Y.-S. Kwon, *Electron. Lett.* **37**, 130(2001).
266. X. Hu, A. Koudymov, G. Simin, J. Yang, M. Asif Khan, A. Tarakji, M. S. Shur, and R. Gaska, *Appl. Phys. Lett.* **79**, 2832(2001).
267. N. X. Nguyen, C. Nguyen and D. E. Grider, *Electron. Lett.* **35**, 1356(1999).
268. I. Daumiller, C. Kirchner, M. Kamp, K. J. Ebeling, and E. Kohn, *IEEE Electron. Dev. Lett.* **20**, 448(1999).
269. A. Tarakji, G. Simin, N. Ilinskaya, X. Hu, A. Kumar, A. Koudymov, J. Yang, M. Asif Khan, M. S. Shur, and R. Gaska, *Appl. Phys. Lett.* **78**, 2169(2001).
270. E. M. Chumbes, J. A. Smart, T. Prunty and J. M. Shealy, *IEEE Trans. Electron Dev.*, **48**, 416(2001).
271. G. Simin, A. Koudymov, A. Tarakji, X. Hu, J. Yang, M. Asif Khan, M. S. Shur, and R. Gaska, *Appl. Phys. Lett.* **79**, 2651(2001).
272. M. Asif Khan, X. Hu, A. Tarakji, G. Simin, J. Yang, R. Gaska, and M. S. Shur, *Appl. Phys. Lett.* **77**, 1339(2001).
273. J. W. Johnson, B. P. Gila, B. Luo, K. P. Lee, C. R. Abernathy, S. J. Pearton, J. I.

Chyi, T. E. Nee, C. M. Lee, C. Chou and F. Ren, *J. Electrochem. Soc.* G303(2001).

274. M. S. Shur, *Solid-State Electron.* **42**, 2131(1998).
275. Hadis Morkoç, Aldo Di Carlo and Roberto Cingolani, *Solid-State Electron.* **46**, 157(2002).
276. Y. Ohno, M. Kuzuhara, *IEEE Trans. Electron Dev.* **ED48**, 517(2001).
277. H. Morkoc, Nitride Semiconductors and Devices (Springer, Berlin, 1999).
278. B. Gaffey, L. J. Guido, X. W. Wang, and T. P. Ma, *IEEE Trans. Electron Dev.* **ED48**, 458(2001).
279. Steven C. Binari, K. Doverspike, G. Kelner, H. B. Dietrich and A. E. Wickenden, *Solid-State Electron.* **41**, 177(1997).
280. S. Arulkumaran, T. Egawa, H. Ishikawa, T. Jimbo, and M. Umeno, *Appl. Phys. Lett.* **73**, 809(1998).
281. I. Irokawa and Y. Nakano, *Solid-State Electron.*, **46**, 1467-1469(2002).
282. T. S. Lay, M. Hong, J. Kwo, J. P. Mannaerts, W. H. Hung and D. J. Huang, *Solid-State Electron.* **45**, 1679(2001).
283. T. Hashizume, E. Alekseev, D. Pavlidis, K. S. Boutros, and J. Redwing, *J. Appl. Phys.* **88**, 1983(2000).
284. R. Therrien, G. Lucovsky and R. F. Davis, *Phys. Stat. Solidi.* **A176**, 793(1999).
285. B. P. Gila, J. Johnson, R. Mehandra, B. Luo, A. H. Onstine, K. K. Allums, V. Krishamoorthy, S. Bates, C. R. Abernathy, F. Ren, and S. J. Pearton, *Phys. Stat. Solidi A*, **188**, 239(2001).
286. P. B. Klein, S. C. Binari, K. Ikossi, A. E. Wickenden, D. D. Koleske, and R. L. Henry, *Appl. Phys. Lett.* **79**, 3527(2001).
287. P. B. Klein, J. A. Freitas, Jr., S. C. Binari, and A. E. Wickenden, *Appl. Phys. Lett.* **75**, 4016(1999).
288. P. B. Klein, S. C. Binari, J. A. Freitas, Jr., and A. E. Wickenden, *J. Appl. Phys.* **88**, 2843(2000).
289. P. B. Klein, S. C. Binari, K. Ikossi-Anastasiou, A. E. Wickenden, D. D. Koleske, P. L. Henry, D. S. Katzer, *IEEE Electron. Lett.* **37**, 661(2001).
290. B. Luo, J. W. Johnson, B. P. Gila, A. Onstine, C. R. Abernathy, F. Ren, S. J.

Pearton, A. G. Baca, A. M. Dabiran, A. M. Wowchack and P. P. Chow, *Solid-State Electron.* **46**, 467(2002).

291. see for example, M. Hong, H. M. Ng, J. Kwo, A. R. Kortan, J. N. Baillargeon, K. A. Anselm, J. P. Mannaerts, A. Y. Cho, C. M. Lee, J. I. Chyi, T. S. Lay, F. Ren, C. R. Abernathy, and S. J. Pearton, *Mat. Res. Soc. Symp.* Vol. **622,** T 2.2.1 (2000).
292. J. Kim, R. Mehandru, B. Luo, F. Ren, B. P. Gila, A. H. Onstine, C. R. Abernathy and S. J. Pearton and Y. Irokawa, *Appl. Phys. Lett.*, **81,** 373 (2002).
293. B. P. Gila, J. W. Johnson, R. Mehandru, B. Luo, A. H. Onstine, K. K. Allums, V. Krishnamoorbly, S. Bates, C. R. Abernathy, F. Ren, and S. J. Pearton, *Phys. Stat. Solidi* **B228,** 171(2001).
294. W. Lu, V. Kumar, R. Schwindt, E. Pina and I. Adesida, *Solid-State Electron.,* **46,** 1441-1444 (2002).
295. B. J. Ansell, I. Harrison and C. T. Foxon, *Phys. Stat. Solids* A, **188,** 279(2001).
296. I. Harrison, N. W. Clayton and N. J. Jeffs, *Phys. Stat. Solids* A, **188,** 275(2001).
297. J. Kim, R. Mehandru, B. Luo, F. Ren, B. P. Gila, A. H. Onstine, C. R. Abernathy, S. J. Pearton, and Y. Irokawa, *Applied Phys. Lett.,* **80,** 4555 (2002).
298. R. Mehandru, B. P. Gila, J. Kim, J. W. Johnson, K. P. Lee, B. Luo, A. H. Onstine, C. R. Abernathy, S. J. Pearton and F. Ren, *Electrochem. Solid-State Lett.* **5,** G51(2002).
299. J. Kim, B. Gila, R. Mehandru, J. W. Johnson, J. H. Shin, K. P. Lee, B. Luo, A. Onstine, C. R. Abernathy, S. J. Pearton, and F. Ren, *J. Electrochem. Soc.*, **149,** G482(2002).
300. J. Kim, R. Mehandru, B. Luo, F. Ren, B. P. Gila, A. H. Onstine, C. R. Abernathy and S. J. Pearton, *Electron. Lett.* **38,** 920(2002).
301. J. Kim, B. P. Gila R. Mehandru, B. Luo, A. H. Onstine, C. R. Abernathy, F. Ren, K. K. Allums, R. Dwivedi, T. N. Fogarty, R. Wilkins, Y. Irokawa and S. J. Pearton, *Electrochem. Solid-State Lett.* **5,** G57(2002).
302. T. Kikkana, T. Nagahara, N. Okamoto, Y. Tateno, Y. Yamngidri, and N. Hara, *IEDM Tech. Dig. 2001*, pp. 25.4.1 -25.4.4.
303. W. S. Tan, P. A. Houston, P. J. Parbrook, G. Hill and R. J. Airey, *J. Phys. D: Appl.*

Phys., **35**, 595(2002).

304. A. Koudymov, X. Hu, K. Simin, G. Simin, M. Ali, J. Yang, M. A. Khan, *IEEE Electron Dev. Lett.*, **23**, 449(2002).
305. A. Vertiatchikh, L. F. Eastman, W. J. Schaff, I. Prunty, *Electron. Lett.*, **38**, 388(2002).
306. D. Mistele, T. Rotter, Z. Bougrioua, K.S. Röver, F. Fedler, H. Klausing, J. Stemmer, O. K Semchinova, J. Aderhold, J. Graul, *Phys. Stat. Solidi A*, **188**, 255(2001).
307. G. Simin, A. Tarakji, X. Hu, A. Koudymov, J. Yang, M. Asif Khan, M.S. Shur, R. Gaska, *Phys. Stat. Solidi A*, **188**, 219(2001).
308. B. Luo, J. W. Johnson, F. Ren, K. K. Allums, C. R. Abernathy, S. J. Pearton, R. Dwivedi, T. N. Fogarty, R. Wilkins, A. M. Dabiran, A. M. Wowchack, C. J. Polley and P. P. Chow and A. G. Baca, *J. Electron. Mater.*, **31**, 437(2002).
309. R. Neuberger, G. Müller, O. Ambacher, M. Stutzmann, *Phys. Stat. Solidi A*, **183**, R10(2001).
310. B. Luo, J. W. Johnson, F. Ren, K. K. Allums, C. A. Abernathy, S. J. Pearton, A. M. Dabiran, A. M. Wowchack, C. J. Polley, P. P. Chow, D. Schoenfeld and A.G. Baca, *Applied Physics Letters*, **80**, 604-606(2002).
311. S. A. Vituserich, N. Klein, A. E. Belyaev, S. V. Danylyvk, M. V. Petrycherch, R. V. Kmokova, A. M. Kurakin, A. E. Rengovich, V. Tilak, J. Smart, A. Vertiatchikh and L. F. Eastman, *Mat. Res. Soc. Symp.* **719**, F5.4.1(2002).

BIOGRAPHICAL SKETCH

Wen-Ben Luo was born in Kaohsiung, Taiwan on November 3, 1973. He moved to Taipei at age of seven and completed most of his education there. He received his Bachelor of Science degree in Chemical Engineering from National Taiwan University in 1996. After serving two years obligatory military service, he pursued his Ph.D. career in University of Florida with joining Dr. Fan Ren's compound semiconductor laboratory in department of Chemical Engineering. From there, he found his research interest in wide bandgap compound semiconductor device processing and characterization, device model simulation, and sensor applications.

After enjoying four years student life at UF, he is ready for future career in semiconductor industry.

I certify that I have read this study and that in my opinion it conforms to acceptable standards of scholarly presentation and is fully adequate, in scope and quality, as a dissertation for the degree of Doctor of Philosophy.

Fan Ren

Fan Ren, Chairman
Professor of Chemical Engineering

I certify that I have read this study and that in my opinion it conforms to acceptable standards of scholarly presentation and is fully adequate, in scope and quality, as a dissertation for the degree of Doctor of Philosophy.

Timothy J. Anderson

Timothy J. Anderson
Professor of Chemical Engineering

I certify that I have read this study and that in my opinion it conforms to acceptable standards of scholarly presentation and is fully adequate, in scope and quality, as a dissertation for the degree of Doctor of Philosophy.

Oscar Crisalle

Oscar D. Crisalle
Associate Professor of Chemical Engineering

I certify that I have read this study and that in my opinion it conforms to acceptable standards of scholarly presentation and is fully adequate, in scope and quality, as a dissertation for the degree of Doctor of Philosophy.

Stephen J. Pearton
Distinguished Professor of Materials Science and Engineering

This dissertation was submitted to the Graduate Faculty of the College of Engineering and to the Graduate School and was accepted as partial fulfillment of the requirements for the degree of Doctor of Philosophy.

May, 2003

Pramod Khargonekar

Pramod P. Khargonekar
Dean, College of Engineering

Winfred M. Phillips
Dean, Graduate School